POLITECNICO DI MILANO
School of Industrial Engineering
Master of Science in Mechanical Engineering

Mechanical Behavior of Stretchable Electronics with Specific Reference to Delamination and Buckling of the Metal Interconnects on Polymeric Substrate

Supervisor: Prof. Pasquale Vena

Co-Supervisor: Ing. Emanuele Cattarinuzzi

Master of Science Thesis by:

Siavash Maraghechi

Matr. 779819

Academic Year 2013–2014

Acknowledgments

I would like to express my most sincere gratitude to Prof. Pasquale Vena, without the help of whom this thesis wouldn't have been possible. I am thankful for all you taught me, all the opportunities you provided me with and the trust you had in me. It would be meaningless for me not to mention Dr. Riccardo Lucchini and Ing. Emanuele Cattarinuzzi, whose insightful guidance throughout the whole thesis was more than helpful. Riki, Ema; thank you also for the friendship, it was a pleasure working with you guys. I also want to thank Prof. Dario Gastaldi and everybody else at the Laboratory of Biological Structure Mechanics (laBS) specifically my dear friends who made the laboratory a lovely place to work at.

I have always said and will always say, I owe everything in my life, everything, even the things I earned on my own, to my parents, in whom I find the root of all that's good in me. My mother who taught me all about "Beauty"; how to know it, how to appreciate it and how to create it. My father who taught me how to live, simply by living his own life the best way imaginable. I admire you two more than anyone else in the whole universe. I wouldn't finish without appreciating the existence of the very first friend I had in my life, my lovely sister. I love you all from the deepest and brightest part of my hearth.

Siavash

Contents

Abstract

Electronic systems that in contrast to the traditional ones, offer mechanical properties such as flexibility and even stretchability, are of growing interest due the new application perspectives they are promising of. As one of the most appreciated approaches, the stretchability of electronic devices can be achieved through distributing rigid sub-circuit islands on a polymeric substrate and connecting them through flexible thin metal interconnects. In this way, major challenges rely on how to achieve reliable stretchability of thin metal film/polymeric substrate interconnects. Among diverse types of interconnects studied in literature, the *in-plane patterned* metal interconnects showed promising mechanical properties as well as stable electrical performance. Nevertheless, practical design indications for reliable mechanical behavior for this specific solution are still lacking. Indeed, local failure phenomena, such as buckling of the thin film and its delamination from the polymeric substrate, can dramatically restrict the safe stretchability range of the interconnects. The current thesis deals with the study of the buckling and delamination of the thin film in S shaped *in-plane patterned* stretchable interconnects, with emphasis on the Aluminum thin film and Polyimide substrate material system. Two specific case studies were investigated, namely the buckling of transversal parts and meanders of the S shaped interconnects. As concerns the methods, *in-situ* experimental, analytical and finite element techniques were explored. The experiments showed that the buckling in the transversal part happens only if the length of this part exceeds a specific value, suggesting the existence of a characteristic length scale for the aforementioned failure phenomenon. In order to interpret the observed phenomena, analytical and computational modeling was exploited, allowing to identify the critical conditions for the mechanical reliability of Al/PI interconnects. Good agreement with experiments in terms of buckling wavelength was found by introducing a finite interfacial stiffness to model the imperfect bond between the thin film and the substrate. As concerns the meanders, experimental evidences stated that buckling doesn't occur during unloading for Al/PI interconnects, while the analytical model allowed to interpret this observation to be due to the plasticity of the substrate.

Keywords: Stretchable Electronics, S Shaped Interconnects, Buckling, Delamination, SEM, *in-situ* Testing, Cohesive Element

Chapter 1

Introduction

1.1 Introduction and Literature Review

When referring to electronic devices, the term recalls rigid objects featuring densely packed circuits on brittle substrates, such as silicon or glassy polymers, However, during the last decade new fields named flexible and stretchable electronics were born. As the name suggests, this field is concerned with introducing new mechanical properties such as flexibility and even stretchability while maintaining electrical performance and reliability of the electronic circuits which is possible by replacing the conventional rigid substrates with compliant polymeric ones.

Flexible electronics addresses promising strides in the social media environment with rollable displays and paper electronics (Rogers, 2001), and more importantly in the photovoltaics, featuring solar cells to be safely applied onto curved surfaces (Matyba et al., 2010; Wu et al., 2010). But being flexibility naturally included in stretchability, it is straightforward to understand why the range of targeted application fields is way broader in the case of stretchable electronics. One of the key advantages of this discipline relies on the inherent conformability of stretchable electronics devices, which then become suitable candidates to interface complex, moving surfaces, like those of living tissues. Minimally invasive and reliable sensing in con-

tact with the human body is the most promising pathway opened by stretchable electronics in the field of healthcare technology. In biomedical applications some examples can be named, such as conformable sensors to be applied on skin (Lumelsky et al., 2001), smart surgical gloves (Someya et al., 2004), wearable electronic systems (Volynskii et al., 2000) and intervention balloon catheter for cardiac ablation (Kim et al., 2011). A shared feature of these examples is that they consist in collections of rigid electrodes or sensors connected to each other through metal interconnections to transmit electrical signals. In continue some examples will be discussed in more details.

To study the neural activity of the brain a high resolution mesh of sensors and electrodes is needed to enable a simple wire connection strategy Complying with the surface topology of the targeted tissue. To this aim, a flexible/stretchable solution based on silicon nanomembranes/ribbons has been proposed by Viventi et al. (2011). To achieve conformability with the most curved surfaces of the brain, open mesh geometries have been developed and deposited on a biodegradable sacrificial silk layer meant to ensure easy handling and positioning during the surgery and to dissolve afterwards (Kim et al., 2010). Figure 1.1 shows this specific application.

During specific surgical operations, mapping the electrical activity across the heart's surface is of importance. This electrical mapping to produce a representation of electrical activity needs to be done over a large region of interest. Integration of a multi-electrode array and multi-purpose sensors on a commercial balloon catheter was possible with the advancements of the stretchable electronics (Kim et al., 2011). The connections of the electrodes can be achieved through an array of serpentine interconnects. Temperature and contact sensors can also be included on the stretchable devices to provide an important feedback on how to adjust and maneuver the inflated balloons without X-ray imaging (Figure 1.2).

Diverse approaches have been exploited to provide stretchability to electronic systems. An interesting example is providing conductivity to polymers by addition of metal or CNT nanoparticles creating conductive nanocomposites (Cai et al.,

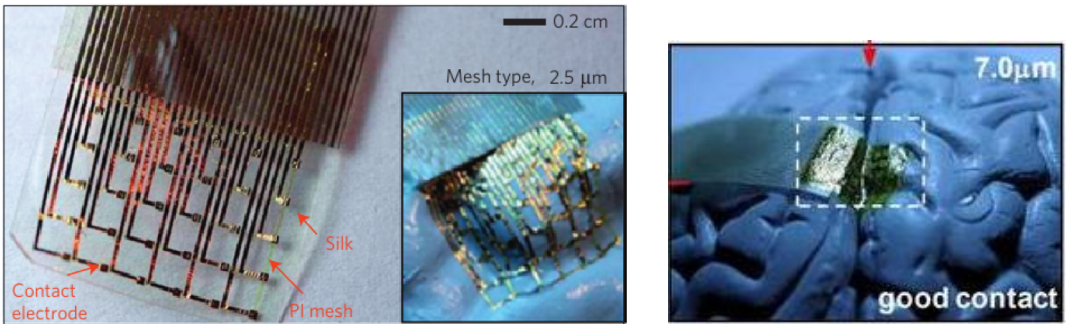

(a) (b)

Figure 1.1: Image of an electrode array with a mesh design on a biodegradable silk substrate. The arrows indicate struts in the mesh that help to stabilize the Au interconnects after dissolution of the silk. The inset and the picture on the left illustrates the high degree of conformal contact that can be achieved on the brain model once the silk substrate has been dissolved.

2012; Jung et al., 2006; Sekitani et al., 2008; Chen et al., 2011). However, the level of conductivity is always relatively poor as compared to the metal interconnects whose potential match with stretchability requirement has been extensively explored as well in the literature. Another solution is metal conductors which can go through stretches with the substrate. It is note worthy to mention that the problem of stretchability of the electronic devices can be focused on the stretchability of interconnects which guarantee the electrical connection between some rigid islands on the thin conformable substrate. Using metal interconnects, there are two main possibilities available to provide intrinsically stiff materials like metals with stretchability. The *out-of-plane* metal conductor design and the *in-plane* patterned design of metal lines. In continue explanation about each solution will be given briefly.

The *out-of-plane* metal or *non-coplanar buckling* conductors is a design based on utilizing the buckling of the thin film conductor on a polymer substrate. The out of plane buckling induced in the thin metal film by compressive strain in the substrate, can provide the system with stretchability. The geometrical properties of these sinusoidal buckling waves depend on the mismatch between the mechanical

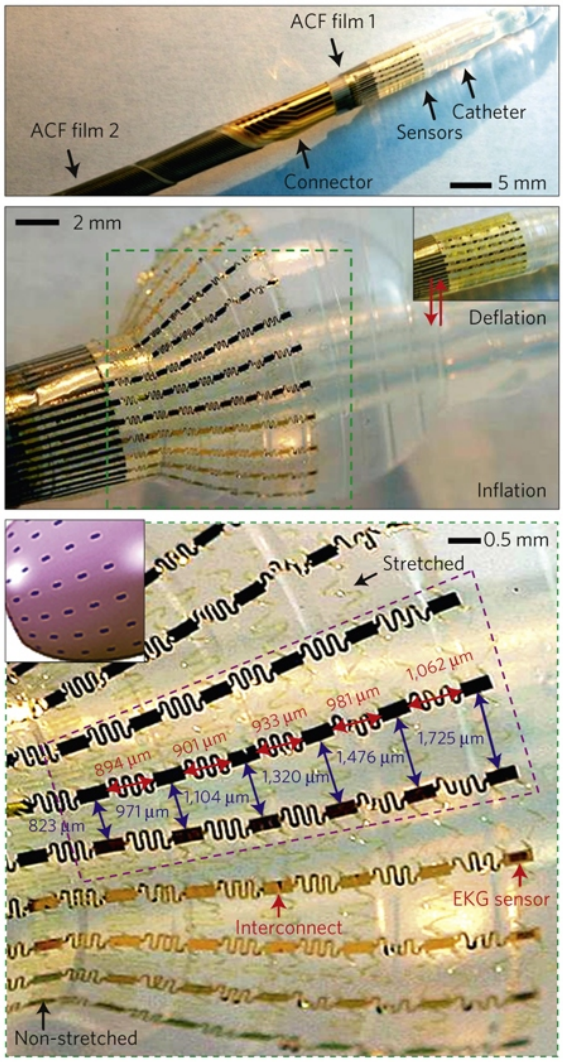

Figure 1.2: Multifunctional inflatable balloon catheters (Kim et al., 2011); (a) Optical image of a stretchable, interconnected passive network mesh integrated on a balloon catheter (deflated), (b) Optical image of the balloon inflated, (c) Magnified view of non-coplanar serpentine interconnects on the balloon in its inflated state.

properties of the thin film and those of the substrate, the thickness of the film, and the magnitude of the strain.

Bowden et al. (1998), more than ten years ago, observed ordered and complex structures of thin film buckling while the substrate on which it was placed were subjected to thermal contraction. Lumelsky et al. (2001) later on for the first time,

introduced the idea of a bendable, stretchable skin with intelligent capabilities such as sensing. In the following years, based on the same idea, several developments were pursued by using pre-stretched substrates to induce the buckling in the metal thin interconnects. Efimenko et al. (2005) reported the fabrication of tunable hierarchical wrinkling, fabricated by uniaxial stretching PDMS network sheets. In another work, wavy Si nanoribbons were created by transfer printing from a Si-on-insulator wafer onto a flat, prestrained PDMS substrate. The releasing of the prestrain generates 1D wavy stretchable layout (Khang et al., 2006). The schematic in Figure 1.3 shows the process.

The wrinkle formation in two directions has been investigated as well, to realize biaxially stretchable electronics (Choi et al., 2007). Several studies has been conducted to allow the control of the wavelength and amplitude of the wrinkles, which dictate the stretchability of the design (Huang et al., 2005; Jones et al., 2003, 2004; Mei et al., 2007; Song et al., 2008; Wagner et al., 2004; Yu and Jiang, 2010). The main issue related to this solution is the fact that the resistance of the interconnects exhibits significant dependence on the applied strain, which can be explained referring to the initiation and propagation of micro cracks in the thin metal film. This evidence makes this kind of solution not suitable for high performance or low power applications. A solution to solve the problem still exploiting the out of plane buckling of the thin film is to provide discontinuous adhesion between the thin metal film and the stretched substrate and then releasing the prestrain. In this way, a preferential buckling behavior is induced, with the possibility to predict the amplitude and the wavelength analytically: this approach has shown promising results in achieving buckled geometries with lower wavelengths (and corresponding higher amplitudes), thus enabling higher stretchability as compared to previous solutions (Sun and Rogers, 2007; Ko et al., 2009). Stretchable interconnects using the *Out-of-plane* designs, in the optimized cases, can bear strains of 100% or more, even approaching the fracture strain of the PDMS (Sun and Rogers, 2007). Another advantage of this kind is that the resistance remains constant with the applied strain however

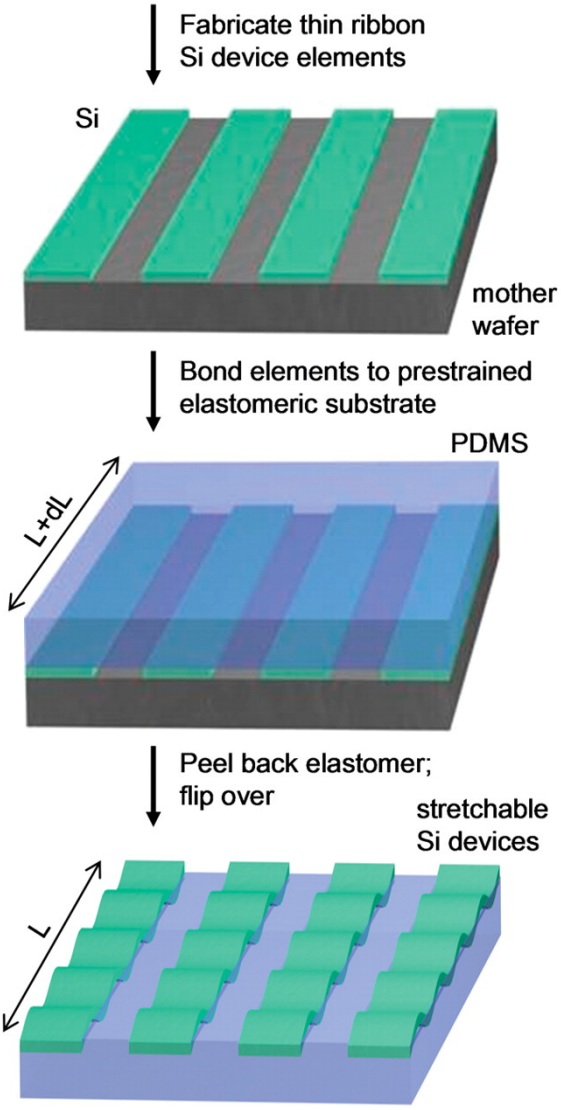

Figure 1.3: Example of fabrication of non-coplanar buckling structure, the picture represent the fabrication of single crystal Si ribbons on PDMS substrate proposed by Khang et al. (2006)

a side effect of this strategy is the incompatibility with biaxial stretchability. The functional sensors and devices can be deposited on the attachment points which function and rigid islands.

An alternative to the *out-of-plane* design of stretchable electronic interconnects is the *in-plane* or the *co-planar-patterned* one. Lacour et al. (2005) and Kim et al.

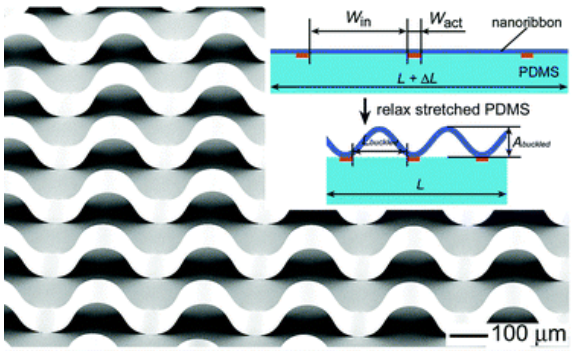

Figure 1.4: Example of out-of-plane buckling membrane with local de-attached areas to the PDMS substrate (Sun and Rogers, 2007)

(2008, 2009) exploited the stretchability by developing a coplanar mesh of wavelike interconnects which are bonded to the substrate. This design is based on the fact that many metals, however being unable to stretch significantly can go through considerable amount of bending if their cross sections are relatively small. for example, by shaping the metal conductor as serpentine, it will act like an in-plane deformable spring during the stretch. this condition results in induction of limited permanent deformation in the metal even when a large deformation is applied to the whole interconnect. As the advantages of this kind of stretchable interconnects, the stable and strain-independent electrical resistance and compatibility with the classical print circuit board (PCB) technology can be mentioned, since the whole design is a planar one. The applicability of PCB methods for the manufacturing the stretchable electronic devices makes possible the realization of industrial applications in terms of low cost and production time.

The shape in which the metal thin film interconnects are formed is of importance to minimize the permanent deformation induced in the thin metal film. The material system of metal/polymer of the thin film and substrate (like Cu/PDMS, Cu/PI, Al/PI, Au/PDMS) is of importance to control this issue as well. Different solutions addressing this issue can be found in the literature (Hsu et al., 2011a). Gonzalez et al. (2007) using a finite element method, studied different shapes and arrived at

the optimal shape of *horseshoe-like* interconnects. Figure 1.5(a) shows two cases of the *horseshoe-like* interconnects.

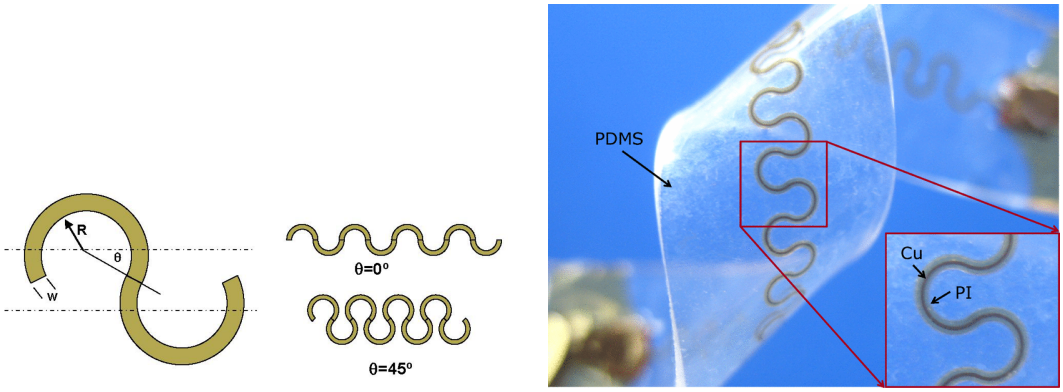

(a) (b)

Figure 1.5: In plane design of stretchable interconnects; (a) Configuration of horseshoe design (Gonzalez et al., 2007), (b) Cu/PDMS stretchable interconnect (Hsu et al., 2011b)

Work done by Axisa et al. (2008) confirmed this by achieving up to 100% elongations using the horseshoe type of interconnects. Lin et al. (2010) reported a comparison between multi-layer and single layer interconnects studying the maximum stretchability each guarantees which resulted in the fact that the constraint that the layers expose n each other reduces the maximum level of stretch applicable to the multi-layer design. Hsu et al. (2011b) proposed covering the Cu interconnect by a PI jacket and then encapsulating the structure inside a PDMS substrate to increase the cyclic stretch performance and also make possible one time stretches up to 250%. Lucchini (2014) has found an optimal design of the intersection of the S shaped interconnections and the rigid islands through numerical and experimental approaches.

1.2 Motivations and Objectives

Although the vast studies on the stretchable electronics during the past years resulted in both good understanding of their mechanics and notable improvements of their manufacturing technologies, still some fundamental limits remain. Insufficient maximum stretchability for the *in-plane patterned conductors*, poor understanding of deformation under complex loading and some local phenomena can be named as the present limitations in this field.

One of the local phenomenon which occurs in the thin film in the *in-plane* stretchable interconnects is its out of plane buckling and delamination. Delamination of the thin film from the substrate can be a critical factor in mechanical and electrical failure of the interconnect. Different studies (Gonzalez et al., 2008; Hsu et al., 2010a; Li et al., 2005) have shown that the interface failure can significantly accelerate the interconnect fracture. After delamination of the thin film from the substrate, the polymeric support cannot perform its strain isolation mechanism that limits the plastic strain in the interconnects tracks. Moreover, the out of plane deformations due to the buckling of the thin metal film, eventually causes stress/strain localizations leading to consequent crack initiation and growth. Experimental studies (Lacour et al., 2003; Kraft et al., 2000; Hommel and Kraft, 2001) confirmed that the free standing thin metal film usually fails in lower strains with respect to the thin metal film bonded to a polymeric substrate. The difference between the two cases is illustrated by Li and Suo (2006) and Lu et al. (2009). Escaping of the dislocations from the surfaces of a tin metal film and preventing proper hardening and resulting in relative low ductility. Lack of hardening causes instability in the the tensile deformation of a freestanding metal film and a perturbation in thickness can initiate necking phenomenon. Having low thickness the local elongation due to necking contributes very little to the final rupture strain. The whole procedure explained here wouldn't be valid if the delamination doesn't occur. One of the main instruments used to study such phenomena, is experimental tools. Due to the

nature of the issue, *in-situ* testing is necessary to be able to obtain a reasonable understanding of different phenomena initiating and progressing during the loading of the interconnects. As definition, *in-situ* experimental methods are referred to those which provide the possibility for physical or chemical characterization which is performed exactly when the targeted phenomenon takes place. More specifically, in-situ experimental mechanics relies on the combination of mechanical testing with other characterization techniques such as microscopy (Hsu et al., 2009, 2011b; Hoefnagels et al., 2010; Neggers et al., 2011), electrical characterization (Kim et al., 2013; Hsu et al., 2010b), typically to investigate the nature of small scale phenomena featured by characteristic length and time scales in the micro or nano range. Kolluri et al. (2009, 2011) have introduced test setups to accurately determine interface properties with simultaneous *in-situ* microscopic visualization of the delamination mechanism. Hsu et al. (2011b) provided proof to their optimal design parameters of PI-enhanced stretchable interconnects through *in-situ* experimental observations. Neggers et al. (2011) investigated the fibrillation process at the delamination front of metal rubber interface through *in-situ* SEM imaging of peel tests of rubber on copper samples. *In-situ* SEM observed experiments correlated with simulations provided understandings of the deformation and failure mechanisms (Hsu et al., 2009; Hoefnagels et al., 2010). With a combination of *in-situ* tensile testing of serpentine interconnects and finite element simulations, Lucchini (2014) has found the interface properties of Al/PI interconnects and studied the effect of geometrical parameters o the buckling and delamination.

Based on the aforementioned points, the objective of the current thesis was defined as follows.

- *To achieve an understanding of the global mechanical behavior of PI/Al stretchable interconnects used in devising stretchable electronics.*

- *To study the local phenomena of buckling and delamination in thin metal film in order to gain insight on the different cases of bucking and delamination.*

– *To study on the parameters affecting occurrence and properties of the buckling of the thin film by means of a combination of in-situ experimental, analytical and numerical approaches*

1.3 Outline of the Thesis

On the ground of the objectives explained above, the organization of the thesis is presented in continue. The present thesis is consisted of seven chapters. The first four chapters following the introductions, are concerned with the explanation of the different methods used in the study of the mechanical behavior of the stretchable interconnects while the last two ones present the results, discussions and finally the conclusions of the current work.

Chapter 2, is dedicated to introducing the in-house developed test setup used for the *in-situ* experimental study of the stretchable interconnects. In chapter 3 the experimental methods used are explained through different testing procedures implemented to study different cases of buckling and delamination of the thin film, as well as the in-scale material characterization performed. Chapter 4 is based on the discussion of analytical models used to study the buckling in different cases corresponding to the cases mentioned in chapter 3. The fifth chapter is concerned with the finite element simulation modeling the buckling and delamination by means of cohesive traction separation law. The results are reported and discussed in chapter 5. This chapter is devised in three parts, each dedicated to the results obtained from one of the methods explained in the preceding chapters. In the end, chapter 6, presents a general conclusion of the thesis by comparing the results from different methods.

Chapter 2

μTensile Test Equipment Development

2.1 Introduction

In order to investigate the local mechanics of S-shaped interconnects at the small scale, a specific characterization equipment is due. In this chapter the specifications of the test setup are introduced. In continue, the equipment selected, i.e. the motor and the load cell, to comply with the characterization aims is described. At last, the development of software interfaces for proper test control is discussed.

2.2 Specifications for the Test Setup

To study the mechanical properties of the stretchable electronics interconnects the very first step in the present study was conducting a series of experimental tests. One of the most noticeable specifications of the stretchable interconnects is the usage of thin films of the polymeric substrate and the metal interconnect, as the conducting material. The thicknesses can be from some tenths of a micron up to few micrometers. Consequently, the specimens suitable to study these kind of interconnects are of the same thickness range. The other two dimensions of the

specimens, however, can be of a higher order of magnitude, though in the scale of few millimeters. Having in mind these dimensions, it is obvious that even a simple tensile test cannot be done using ordinary equipment such as a universal testing machine.

First of all, gripping such a specimen (about 10 μm thick, 3 to 4 mm wide and 200 mm long) with a normal universal machine, without damaging it, is impossible. Moreover, the velocities of the grips should be of an order of few micrometers or even nanometers per second, not to induce high strain rates on the specimen, concerning its low initial length. Finally, a very sensitive load cell is needed to measure the small forces resulted from the stresses applied on the very small cross section.

2.3 Description of Equipments

An in-house developed μTensile testing machine was assembled and programmed to perform different tensile tests. A 1 1 M-112.1VG Linear Stage (Physik Instrumente, Karlsruhe, Germany) was used to apply the displacements needed. A Honeywell 31 low range precision miniature load cell (Burster, Dusseldorf, Germany) with a 5N full scale in tension and compression have been chosen. Both motor and load cell possessed vacuum compatibility. The motor (stage) and the load cell were assembled on frame as seen in the figure 2.1. This figure is showing the motor setup in two configurations. Figure 2.1(a) shows the configuration used for testing in normal conditions (outside the ESEM chamber) in order to perform *in-situ* testing based on optical microscopy while Figure 2.1(b) is showing the configuration used for putting the machine inside the Environmental Scanning Electron Microscopy (ESEM) chamber for ESEM based *in-situ* testing.

The out of chamber configuration was equipped by a digital optical microscope consisted of a 10 Mega-pixel CMOS camera and a 10x objective, mounted on an in-house triaxial linear stage to be able to study different regions of the specimens easily as can be seen in Figure 2.2(a). Due to the lack of enough space in the

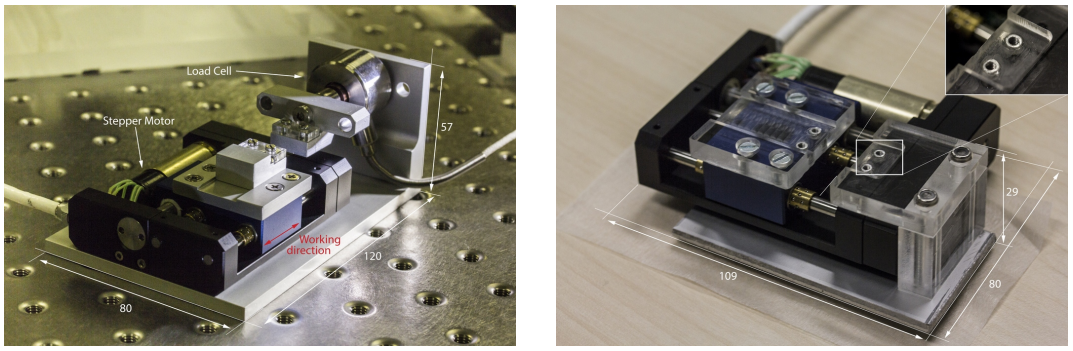

(a) (b)

Figure 2.1: Micor Tensile test setup (a) for air configuration (outside ESEM chamber); (b) for vacuum configuration (inside ESEM chamber)

chamber, the setup for ESEM case doesn't include the load cell. In Figure 2.2(b) the assembly of the motor inside the ESEM vacuum chamber is seen. A specific flange was prepare in the research group to make possible the connection of the motor inside the chamber and the controller outside.

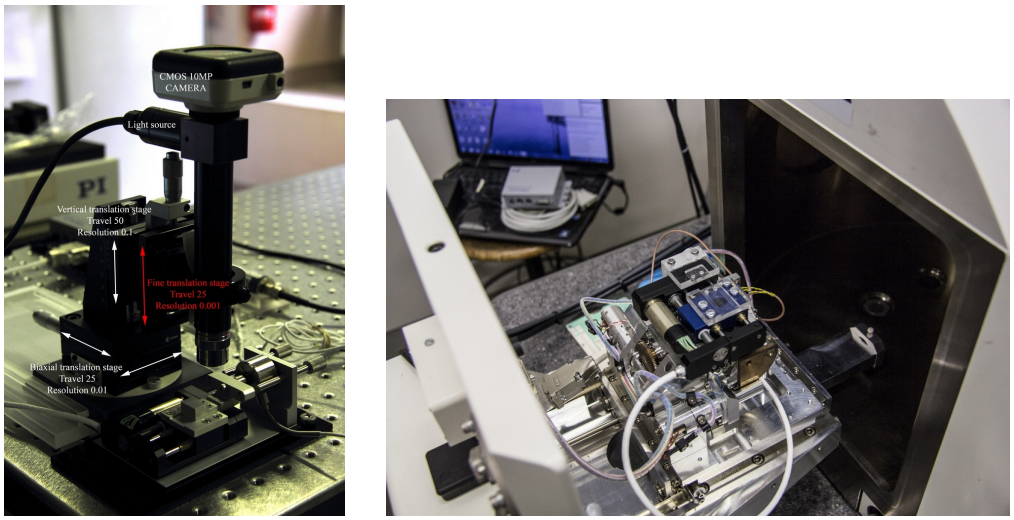

(a) (b)

Figure 2.2: μTensile test setup with two cases of *in-situ* microscopy methods; (a) optical microscopy, (b) environmental scanning electron microscopy (ESEM)

2.4 Load Cell Calibration

The calibration must have been performed while the load cell was assembled on the frame of the in-air configuration of the setup (Figure 2.1(a)), otherwise the procedure of assembling the load cell itself could have introduce shifts in the load value. To do so, the setup was rotated for 90 degrees, as seen in the Figure 2.3(a), to make it possible to perform the calibration utilizing the gravity. A set of different very precise weights ranging between 0.02N to 150.00N were used to impose known forces on the load cell, the voltage produced by the load cell was measured, and the relation between voltage and load was found. The ratio between load and the voltage was found to be 1.0416. The more detailed results can be found in the plot presented in Figure 2.3(b).

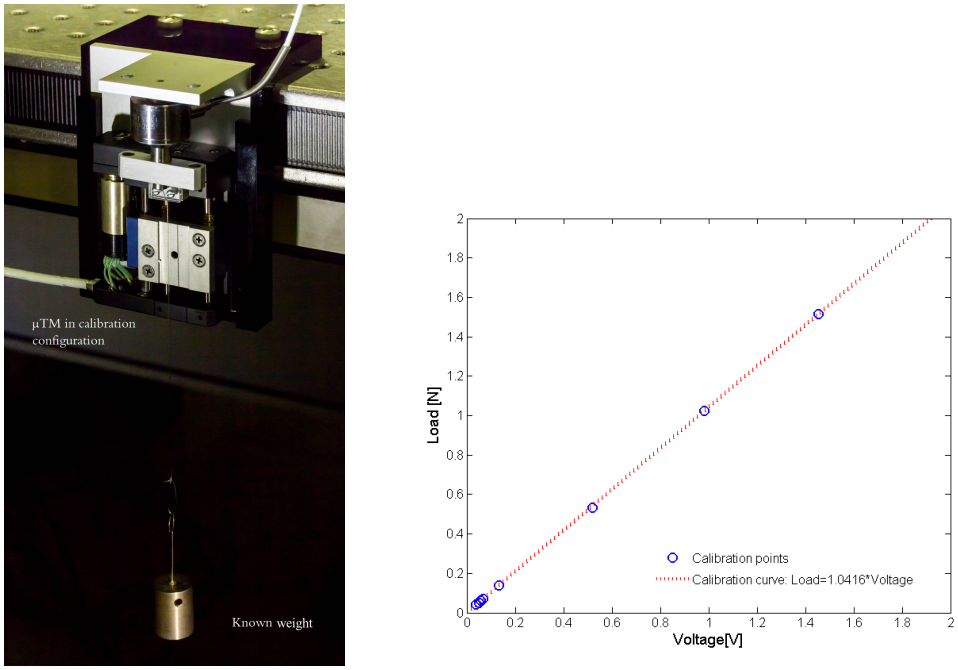

(a) (b)

Figure 2.3: The Load Cell Calibration (a) The setup; (b) the Load voltage relation resulted from the calibration process

2.5 Control Procedures

In order to control the motor's speed and position and all the while, measure the force from the load cell and the motor's position there was the need to prepare some VI's (Virtual Instrument) in LabVIEW. The connection of the motor to the computer was obtained through a C-863 Mercury DC Motor Controller. The Load cell was connected to the PC using a Burster A/D convertor and a Burster 9205 Amplifier. Securing the correct connection of the instruments to the computer, the needed VI's were programmed using the sub VI's provided by the motor and load cell manufacturers.

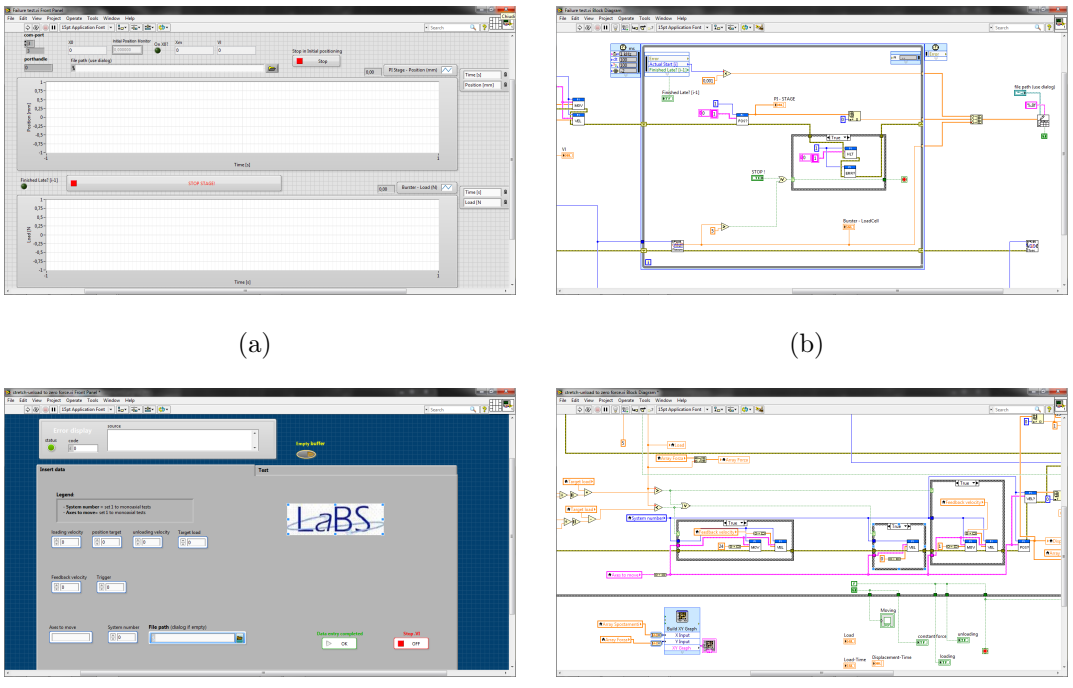

(a) (b)

(c) (d)

Figure 2.4: Examples of VIs' Front Panel and Block Diagram (a) Front Panel of Failure Test VI; (b) Block Diagram of Failure Test VI; (c) Front Panel of the Unloading test VI; (d) Block Diagram of the Unloading test VI

A series of different VI's were constructed, each serving for a certain experimental test such as Tension up to failure test, Cyclic loading-unloading test, Loading then

unloading up to zero force test (due to visco-elasticity of the substrate), etc. Each VI is consisted of a Front Panel and a Block Diagram. The Front Panel is where you can control the parameters and monitor the measured values before and during the test, while the Block Diagram is the program designed to connect the controls in the front panel and perform operations on the data flowing in and out during the test. In Figure 2.4 some examples of the VIs' Block Diagrams and Front panels are presented.

Chapter 3

μTensile Tests

3.1 Introduction

In order to investigate the mechanical behavior of the stretchable electronic interconnects, both globally and locally, a series of tensile tests was designed and performed. In this chapter, the different specimens and then the different testing procedures conducted on them are introduced. In the first set of tests, material characterization of Polyimide in the real scale were performed which consisted of diverse experimental procedures. In continue, a set of tests were performed on the stretchable interconnect specimens both for the understanding of the global mechanical characteristics and the local study of buckling and delamination. First set was to study the buckling and delamination of the transversal parts of the metal interconnects, a phenomenon which happens during loading. In continue, in order to study the possible buckling in the meanders of the interconnects, which could happen during unloading, another set of tests have been designed and performed. The details about each testing procedure will be discussed in continue.

3.2 Samples Description

In this section the specimens used as the samples of the interconnects are introduced and their geometrical and mechanical properties are discussed in detail.

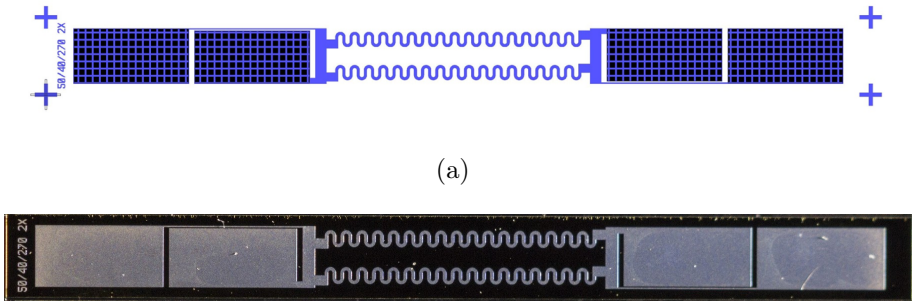

(a)

(b)

Figure 3.1: S Shaped interconnet specimen W50R40A270 (a) The Schematic; (b) Image taken by Optical Microscope

As mentioned in chapter 1, the focus of this study was on the In-plane design of the stretchable interconnects. The specimens used, were consisted of a polymeric substrate with metallic serpentine interconnections. A 10 μm thick film of Polyimide (PI) and a 1 μm thick, Aluminum film shaped in the form of the S shaped interconnects make up the substrate and the electrical interconnection, respectively. The width of the polymeric substrate is 1200 μm. The gauge length of the specimens (i.e. the whole length apart from the gripping sections at the two ends) was 4000 μm which in theory can define the gauge length. The samples were prepared at the BioMEMS Research Unit of Fondazione Bruno Kessler (FBK, Trento IT) and Commercial Polyimide (PI) Durimide115A (FUJIFILM, USA) was used for the polymeric substrate.

Figure 3.1 shows one of the specimens and a schematic of it. It can be observed from Figure 3.2(a) that each serpentine interconnect is basically constructed out of a series of meanders and transversal parts. These two parts can be considered as the main parts of a serpentine structure form a mechanical point of view in each of

which Buckling and delamination can take place, but with different conditions. The geometry of the S shaped interconnects can realize different forms. Figure 3.2(b) shows the three parameters controlling the geometry of the serpentine. The metal track width (W), the inner circles radius (R) and the amplitude (A) which is the transversal distance of the highest and lowest point of the serpentine shape. Four different kinds of specimens were used in the current study, changing the serpentine geometry by changing the three parameters mentioned above.

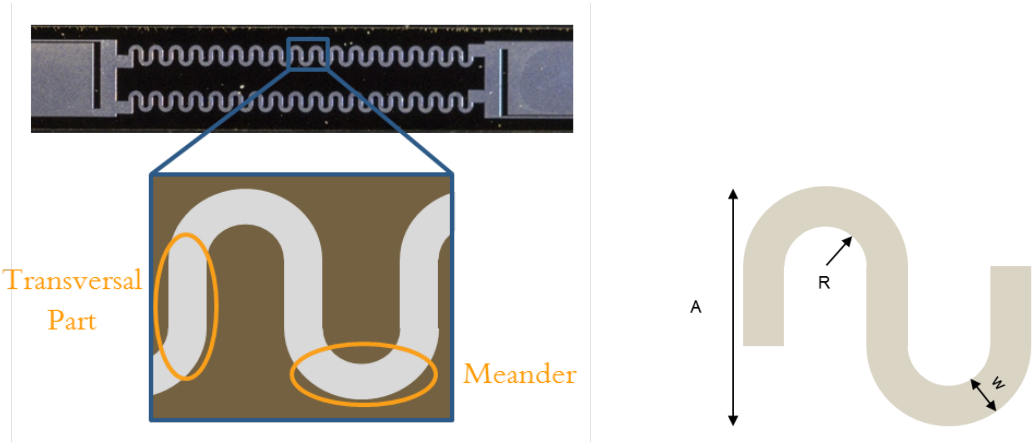

(a) (b)

Figure 3.2: Schematics showing the serpentine interconnect geometry; The two main structural parts of a serpentine stretchable interconnect, fig serp-geom The geometric parameters of the serpentine

The different parameters, defining the geometry of each specimen can be found in the table 3.1. With these specimens a good range of the ribbon width and the transversal part length was covered. In continue, when discussing the results of the experiments, the effect of the transversal part length on the buckling and delamination of the thin metal film will be mentioned.

Table 3.1: The geometric parameters of different specimens

Specimen Name	Width	Internal Radius	Amplitude	Transversal Part Length
W10R20A90	10	20	90	30
W20R20A120	20	20	120	40
W20R40A180	20	40	180	60
W50R40A270	50	40	270	90
W50R40A180	50	40	180	0

3.3 Material Characterization of Polyimide at the real scale

An understanding of the mechanical properties of Polyimide in the real scale was necessary as a preliminary step. Besides the importance of the mechanical properties this was due to make possible the comparison of the pure PI specimens with the composites Al/PI samples of the interconnects. PI Specimens the same size as the interconnect specimens but lacking the metal thin film were available. Three kinds of tests were performed: monotonic loading test, loading with repeated partial unloading and a a sort of creep test to study the viscoelasticity of PI.

First of all a simple stretch test was conducted to obtain the load displacement and in continue stress strain relation of the PI. This test was conducted on a number of similar specimens to check the repeatability of the tests results. Each tests was continued up to the specimen breakage. In order to eliminate errors due to misalignment of the sample and sliding in the grips, the real stretch induced on the sample was calculated by optical acquisition. As can be seen in Figure 3.3 six color markers have been placed on each specimen which in conjunction with a MATLAB code that was prepared in the research group, gave the accurate displacements and consequently the accurate strains.

In continue, to study the viscoelasticity in the Polyimide and the time dependent properties a creep tests was performed. It was not intended to study in detail the viscoelasticity of the specimens, but it was enough to obtain an idea of the time

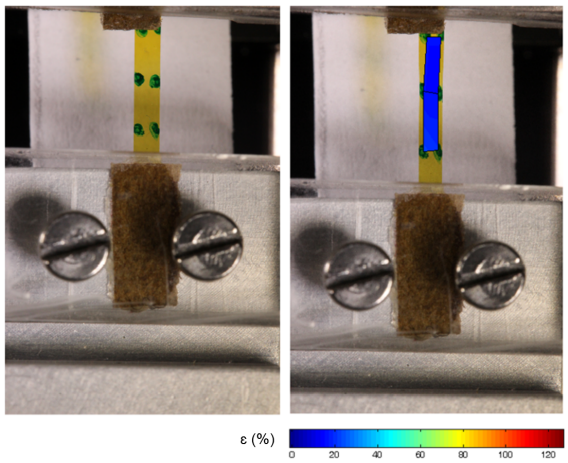

Figure 3.3: (left) Polyimide sample before the test, with six colored markers to make possible the accurate strain measurement, (right) Optical axial strain measurements at a representative time during the test

scale of the irreversibility observed previously in the specimens. To do so, the test was designed as loading the specimen immediately up to 1.1 N load, holding in the maximum force for 4500 sec and then unloading back to force equal to zero and holding there again for 4500 sec. The load time history is found in Figure 3.4.

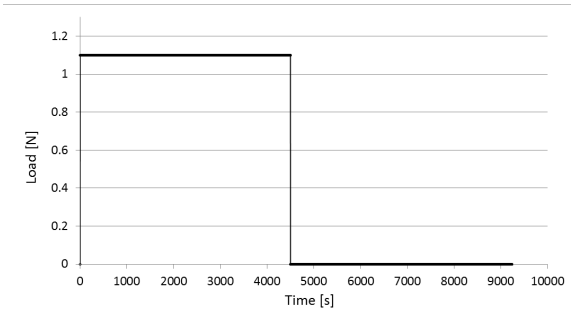

Figure 3.4: The time history of applied load for the creep test performed on the PI samples

In here the results of this test will be briefly discussed since the results were important for the continue of the characterization. In Figure 3.5 are presented the load and displacement data acquired during the creep test from the load cell and the motor, respectively. It is seen that after 4500 seconds of constant load after the

unloading, remains a considerable amount of non recovered displacement. Though it can not be simply interpreted as plasticity, the time scale of the application of the stretchable electronics is less than this, thus it can be treated as plasticity from a phenomenological point of view. It is note worthy to mention that Figure 3.5(a) shows the robust response of the system to the commands (the plot in Figure 3.4 is the command to the motor applied through the LabVIEW virtual instrument designed for the creep test) proving the reliability of the designed testing system.

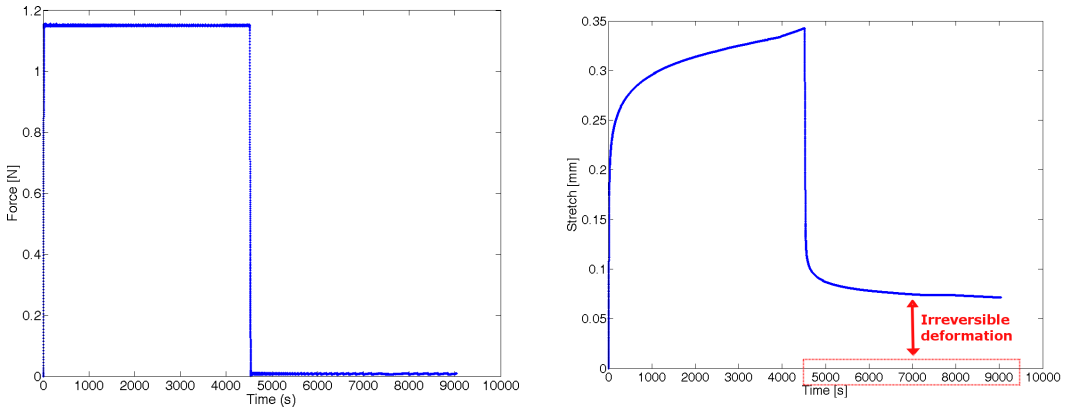

(a) (b)

Figure 3.5: The creep test on the PI specimens; (a) Load data acquired from the load cell, (b) the displacement acquired from the stage

Having arrived at the conclusion of the plasticity of PI (only phenomenologically) a final test on these specimens was conducted. A loading with repeated partial unloadings was operated in order to be able to study the plasticity precisely. The time history of the displacement can be found in the Figure 3.6. The isotropic hardening law with the procedure explained in continue was used to obtain from the results the true - true strain as well as true stress - plastic strain relations for the PI. The engineering strain is found initially as:

$$\varepsilon_{lin} = \frac{\Delta L}{L_0} \tag{3.1}$$

Then the logarithmic (true) strain is found as shown below:

$$\varepsilon_{log} = \ln \frac{L}{L_0} = \ln(1 + \varepsilon_{lin}) \tag{3.2}$$

The nominal stress defined as the ratio between the force and the initial cross sectional area is:

$$\sigma_{nom} = \frac{F}{A_0} \tag{3.3}$$

While the true stress is defined as the ratio of the force to the actual cross sectional area.

$$\sigma_{true} = \frac{F}{A} \tag{3.4}$$

And based on the assumption of isochoric deformation $A_0 L_0 = AL$, so the equation 3.4 can be converted to:

$$\sigma_{true} = \sigma_{nom}(1 + \varepsilon_{lin}) \tag{3.5}$$

And finally the plastic strain will be found as:

$$\varepsilon_p = \varepsilon_{log} - \frac{\sigma_{true}}{E} \tag{3.6}$$

The yield stress was found in continue as the 0.2% offset yield strength after the calculation of the mean elastic modulus. In detail results will be discussed in chapter 5.

3.4 Transversal Buckling and Delamination

In order to study the buckling and delamination of the transversal parts of the stretchable interconnects experimentally there was the need to design a specific testing procedure. Referring to the figure 3.1, the transversal part of the serpentine, perpendicular to the axial direction of the specimen, will go through compression due to Poisson's effect, while the specimen is under tension. The polymeric substrate

imposes compression to the thin metal film of the transversal from underneath. If this compression, which depends on the tension applied to the interconnect, is high enough the thin film buckles. With the thin film buckling, due to the new state of stress in the interface between the substrate and the film, delamination can occur too. This phenomenon can be conceived in the contrary order as well (i.e. the delamination might happen before the buckling starts). Due to the shear stress in the interface between substrate and the thin film, the delamination may occur, changing the boundary condition of the thin film from a beam on an elastic substrate to a free beam and lowering the buckling critical load. Consequently and in continue, the buckling can happen.

In order to induce the aforementioned failure mechanisms in the transversal parts, uniaxial traction of the specimens up to global failure was selected as a suitable and practical testing technique. The tests were performed in two configurations. firstly, *in-situ* optical imaging in the out-of-chamber configuration was used to correlate the onset of failure with the overall stress acting on the specimen in the stretch direction. Secondly, more accurate investigation of damage evolution was pursued by means of *in-situ* electron scanning microscopy imaging in the "inside-chamber configuration". The Environmental Scanning Electron Microscope (ESEM) was used for this purpose providing magnifications from 50X to 10000X. In continue, the detailed procedure of each of the configurations will be introduced.

It is note worthy that the specimens used for this kind of experiments were only the specimens that included the transversal parts of 30, 40, 60 and 90 μm long as can be found in Table 3.1.

3.4.1 Testing with Optical Microscopy

It was only in the out of chamber configuration of the μTensile testing machine that the load data could have been available, so a series of tests were needed in this configuration in order to obtain the global load-displacement and consequently the

stress-strain relations for each kind of specimens also to make possible the comparison with pure PI samples. On the other hand, these tests established the validity of the tests to be later performed again with the inside chamber configuration which lacked the load data.

Uniaxial traction tests in displacement control were performed according to the stretch with repeated partial unloading, ending with a last step of stretch up to global failure of the specimen as depicted in Figure 3.6 (the same as the procedure for PI characterization). The grip speed was chosen to be 1 μm/s to ensure the quasi-static conditions of the loading.

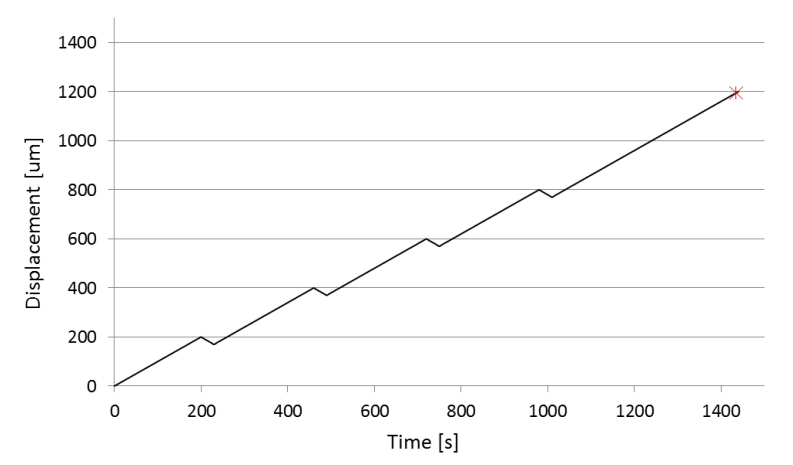

Figure 3.6: The time history of applied displacement for the transversal buckling test in the out of chamber configuration.

The same test was conducted for each of the four kinds of the specimens explained in the previous section. For each specimen, the load and displacement data was collected from the load cell and the motor, respectively. The same testing procedure was repeated three times on the W10R20A90 specimen, showing a very good repeatability in the results on the basis of load-displacement and stress-strain curves. The load-displacement curves obtained from the tests on different specimens, showed that the geometry of the serpentine interconnect doesn't affect the global behavior of the specimen. Based on this observation, the substrate cross sectional area was

used in order to calculate the engineering stress for all of the specimens. The results concerning the load displacement and stress strain relations will be discussed in detail in chapter 5 of the thesis.

During each tests some photos have been captured at certain intervals of $20s$, by the optical microscope, to reveal the initiation of buckling and delamination and their progress in different stages of the test. However, more detailed results were revealed by the pictures taken by the ESEM to be discussed in continue.

3.4.2 Testing in Environmental SEM Chamber

The second set of experiments to study the transversal buckling in the S shaped interconnects, was a set of *in-situ* tensile tests within the Environmental Scanning Electron Microscope (ESEM). The main purpose of this part of the experimental studies was to observe in detail, the buckling and delamination of the transversal parts of the interconnects. This was made possible by the high resolution and highly magnified images obtained from the ESEM (between 50 nm to 100 nm). The same testing procedure explained in the previous section was used here with a small modification. Based on the focus of this sets of tests, the local study of the buckling, partial unloading parts were replaced by rest phases. The duration of each rest phase was set to 100 seconds which was required by the ESEM for refined electron image acquisition. Although the whole duration of each test was observed by a lower resolution technique of ESEM to ensure fast screen refresh and update, and high resolution images were acquired during these rest phases. In addition, the loading up to a certain point is i.e. 800 μm of displacement, is executed without the constant intervals. This modification was since the buckling and delamination of the thin film in the transversal part doesn't initiate before a certain amount of stretch imposed on the specimen. The time history of the displacement applied can be found in the figure 3.7. The loading rate again to be exactly compatible with the out of chamber set pf tests was chosen to be equally 1 μm/s.

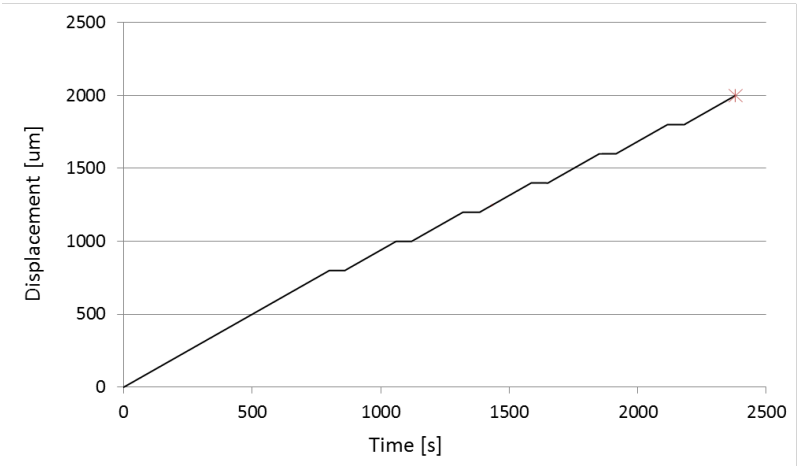

Figure 3.7: The time history of applied displacement for the transversal buckling test in the inside chamber configuration.

The traditional SEM method, requires the material to be conductive or if not to be metal coated. In the case of the current study, the specimens were in a major part consisted of polymers. On the other hand, metal coating the specimens would have affected the mechanical behavior of the specimens, specifically in the delamination and relative mechanical behavior of the thin metal film and the polymeric substrate. While, using an environmental scanning electron microscope (ESEM), the problem was solved. The ESEM allows for the option of collecting electron micrographs of specimens that are non-coated and even wet. This specification makes ESEM popular for biological studies, allowing the specimens to be in their natural state. For the present case, using ESEM was necessary to give the precision of the SEM and the option of not manipulating the specimens mechanically.

3.5 Meander Buckling and Delamination

The second part of the experimental studies conducted in the present work consisted of the experimental study of a possible buckling occurring in the meander of the interconnects. It is very often that the stretchable electronics experience unloading or even cyclic loading and unloading. On the other hand, during loading, plastic

strains can be induced inside the metal thin film structure of the whole interconnect. This plastic strain is more likely to develop and is concentrated in the meander of the serpentine (Hsu et al., 2011b). Consider a stretchable interconnect which is gone through enough loading to induce some plastic strain inside the meanders. If in continue it is completely unloaded, since the polymeric substrate being elastic is willing to go back to it's original length and there is some permanent deformation trapped inside the thin metal film in the meanders, the meanders will experience a compression induced from the substrate underneath. This compression causes the thin metal film to buckle and even delaminate from the substrate. A similar phenomenon, buckling of the meanders due to compression induced from the substrate underneath, is observed in the experimental images reported by Gray et al. (2004). So in order to study this kind of buckling and the possibility of its occurrence, there was the need to stretch the specimens up to a point ensuring the inductance of plastic strain in the meanders while not breaking the sample, and then unloading it back to the original length. In order to be sure about the plasticity of the meanders, the amount of initial stretch was decided by the results coming from the previous set of tests for studying the transversal parts buckling, expecting the meanders to already had gone through enough plasticity when the transversal parts buckled. For unloading the specimen, going back to the initial position could not create proper unloading conditions. The material characterization of PI resulted in detection of a phenomenological plasticity which will be discussed in details in chapter 5. Due to the permanent deformations that the stretch induced in the PI substrate, unloading in a position control manner resulted in global buckling of the specimens. To cope with this issue, the unloading was performed with a simple force control approach (i.e. unloading the specimen back to a point guaranteeing the force measured by the load cell to descend and remain zero). In this way the viscoelasticity effect of the substrate was avoided as well.

Again the tests should have been divided in two sections of inside and outside chamber. In continue each kind will be explained in details. The specimens used

were the two extreme cases of transversal length; one without the transversal part and the other with 90 μm long transversal parts as the longest case which can be found in the Table 3.1. The highest length of transversal part provided the highest amount of plastic strain in the meanders (Lucchini, 2014). The no transversal part specimen, on the other hand, was chosen due to the different serpentine distortion mechanisms it goes through which could contribute to the delamination of the meander due to the shear stress in the interface.

3.5.1 Testing with Optical Microscopy

The testing procedure was to stretch the specimens up to a certain point in displacement control, and then unloading back and controlling for the force to arrive back at zero in order to stop the unloading. In continue, the program (Virtual Instrument, VI) developed in LabVIEW continued to control for the force to remain zero (a very small positive value negligible with respect to the range of load experienced by the specimen which could be assumed as zero), moving the grip in case the measured load changed from zero with more than 5% error. The limit for stretching the specimens was chosen with reference to the tests performed to study the transversal part buckling. It was observed from those tests that the specimens do not break before 40% percent of global strain while showing a considerable amount of transversal buckling which suggests enough loading to have plasticity in the meanders. Again the displacement rate was chosen to be 1μm/s not to induce any kind of viscoelastic phenomenon. The time history of the displacement applied can be found in the figure 3.8.

Each test was observed by the optical microscope and a number of images was gathered during the loading and unloading but most importantly after arriving at the zero force. The tests were not terminated immediately after the first occurrence of zero force after unloading, though continued for a while to let the recovery of the viscoelasticity induced in the specimens during loading. The recovery time was

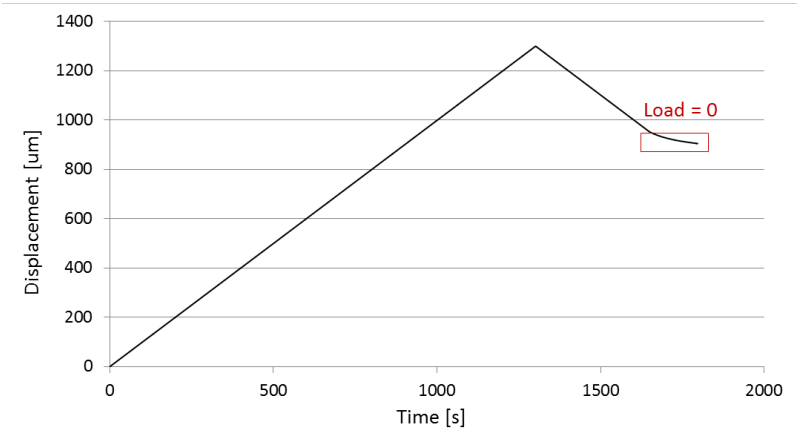

Figure 3.8: The time history of applied displacement for the meander buckling test in the out of chamber configuration.

about a few hundreds of seconds the same as the creep test on PI as mentioned in section 3.3 however, in a single tests a recovery time of about 20 hours was chosen. Time dependent behavior shows negligible contribution after 4500s: actually, after this time lapse, the creep was not completely arrested, but the creep rate was extremely low, such that no significant decrease in the displacement value could be recorded extending the test for further 20 hours.

3.5.2 Testing in Environmental SEM Chamber

Like the previous case, to study the local phenomena including bucking and delamination in the meanders there was the need to perform the same test inside the ESEM chamber. Since the inside chamber configuration lacked the load cell, an alternative method should have been devised to obtain the unloaded but not globally buckled specimens, enabling proper image acquisition by the ESEM. Based on the load cell measurements form the out-of-chamber experiments, an interpretation of the displacements resulting in zero force after a certain amount of loading was obtained. In order to ensure the same correspondence between overall loads and displacements, the inside chamber tests were conducted with the exact same initial lengths and were stretched up to the same point before unloading. The time history

of the displacement applied can be found in the figure 3.9.

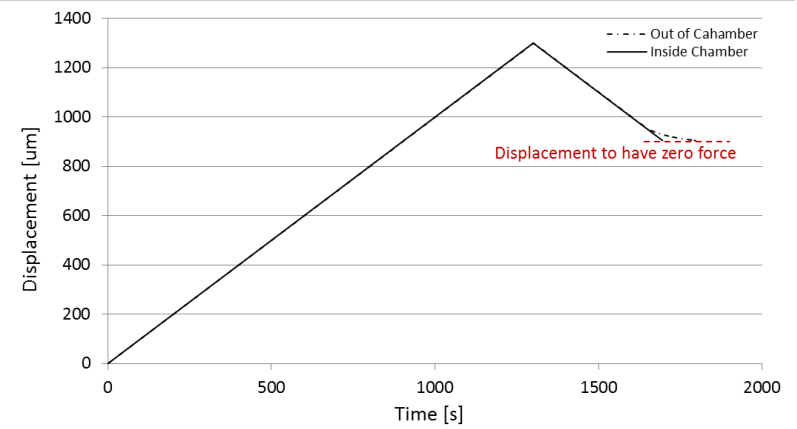

Figure 3.9: The time history of applied displacement for the meander buckling test in the inside chamber configuration

Again during the loading and unloading and also after the total unloading, some images were captured to investigate the buckling and delamination in the meanders.

Chapter 4

Analytical and Numerical Models for Buckling

4.1 Introduction

Analytical modeling was explored as a pathway to develop effective tools for the prediction of the buckling phenomenon occurring in the metal thin film of the stretchable interconnect. The transversal buckling problem was defined as two dimensional and plain strain simplified problem be solved analytically. In order to solve the problem an analogy was used. Another problem with a similar geometry but different loading and boundary condition with a known solution was found in the literature. The analogy was examined to establish the analogous parameters in the two problems. Based on the fact that in the experiments the buckling was always accompanied by delamination, another model was exploited for the transversal buckling, this time to account for the imperfectly bonded interface between the metal thin film and the polymeric substrate. Second part of this chapter is on the analytical model studying the possible buckling of the meanders in the S shaped stretchable interconnects. Again the problem was defined in a simplified 2D, plain strain case to be solved analytically. The analogous problem used for the transver-

sal buckling problem was used once again, taking the analogy to a further step considering the fact that in this case of buckling happens during the unloading of the interconnects and due to the plastic strain in the thin film. The model was in continue modified by introducing plasticity in the substrate as well.

The problem of transversal buckling was simulated using finite element method. In order to validate the analytical models a quantitative reference was needed, so the computational method was used to bridge the experimental and the analytical results. The model was done to predict both buckling and delamination in the thin metal film. To model the interface between the thin film and the substrate cohesive elements were used. The constitutive law governing the interface was obtained in a form of a traction-separation law resulted from another work conducted in the research group (Lucchini, 2014). The effect of different values of interfacial stiffness and the the different lengths on which the buckling and delamination could happen was studied through the buckling wavelength and critical strain. In this way the bridging between the analytical and experimental parts was made possible.

4.2 Analytical Model for Transversal Buckling During Loading

The buckling of the transversal part of the S shaped interconnects used in the stretchable electronics, was studied analytically using two different models. One model, considering a perfect bond between the thin metal film and the polymeric substrate for the sake of simplicity and another one, considering a non perfect bonded interface between the two parts, in order to model the actual case more accurately. The two models will be discussed in the following two sections of this chapter.

4.2.1 Perfectly Bonded Interface Model

The buckling problem in the transversal part of the interconnects was defined in a simplified two dimensional plain strain case. In order to be able to model the problem in a 2D form we needed to neglect the effect of the curved part of the S shaped interconnects and to focus only on the transversal part. the problem was defined looking at the cross section of the stretchable interconnects, and in the axial direction, since the buckling is happening out of plane with respect to the substrate and the thin film, as it can be seen in Figure 4.1.

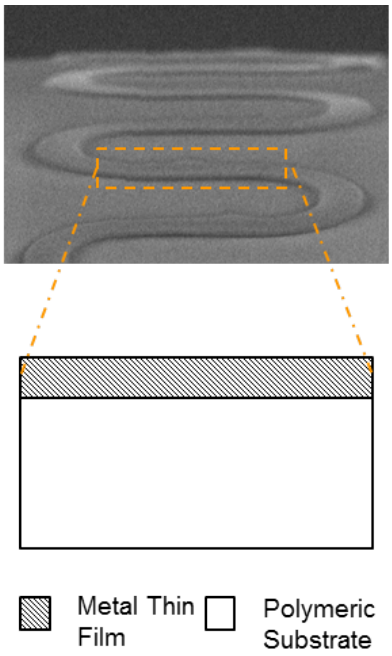

Figure 4.1: The cross sectional view of the transversal part of the S shaped interconnects to define the transversal part buckling problem

As mentioned before, the buckling in this case happens due to the Poisson's effect. The interconnect which is subjected to stretch in the axial direction, experiences compression in the transversal. So the loading on the configuration seen in Figure 4.1 in terms of applied strain can be considered as the multiplication of the axial strain and the Poisson's ration of the substrate in compression. The definition of the problem can be explained through Figure 4.2. The initial configuration in 4.2(a) is

showing the metal thin film lying on the polymeric substrate and perfectly attached to it, the Initial length is L_0. In the second part i.e. Figure 4.2(b), the loading on the system is shown. Due to the compression in the transversal part, the length of the system decreases to $L_0(1-\nu\varepsilon)$. In the end Figure 4.2(c) shows the buckled configuration still under compression.

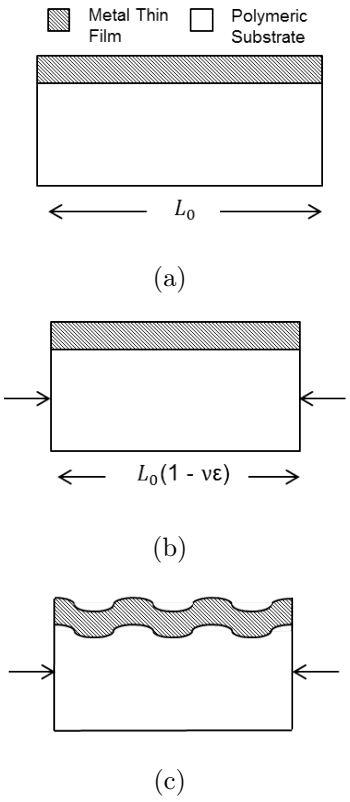

Figure 4.2: The definition of the problem of transversal buckling; (a) Before loading, (b) During loading and before buckling (Shortened in the transversal direction due to the axial stretch and the Poisson's effect), (c) the buckled configuration

To solve the problem an analogy was used. A problem with a similar geometry but different boundary condition and loading was found in the literature. In the work done by Song et al. (2008) problem of buckling of a thin metal film on polymeric substrate was solved. This problem was based on the out of plane design of stretchable electronics. The problem solved by Song et al. (2008) as depicted in Figure 4.3 can be explained as follows. In order to make a stretchable electronic

interconnect exploiting the out of plane design, firstly the substrate is pre-stretched to have a length matching with a previously longer thin metal film. The thin metal film is attached to the pre-stretched substrate in continue. Now on releasing of the whole system (the thin metal film in a strain free state and the pre-stretched substrate attached together) the substrate is willing to go back to it's initial length which puts the thin metal film in compression. If the amount of the pre-stretch, consequently the prestrain inside the substrate, is high enough to induce enough compressive stress in the thin film, the later will buckle. It is easily grasped that the prestrain in the analogous problem is in direct analogy with the strain in the transversal direction (the axial strain multiplied by the Poisson's ratio) in the original problem of transversal buckling.

The problem was solved by Song et al. (2008) with an energy approach. The energy terms for the thin metal film and the polymeric substrate were derived. The total energy was differentiated with respect to the two geometrical parameters defining the displacement field in the buckled configuration. Putting the differentiated terms equal to zero, gave the equilibrium state. Using the same approach and parting from the energy terms reported in the mentioned article, the results were derived and compared with the ones reported by Song et al. (2008).

The energy terms were derived considering infinite deformation and rotation. The thin film energy was described by two terms of bending and membrane energy. The interface shear was considered negligible. The thin film's membrane and bending energy terms are found in equations (4.1) and (4.3). The substrate was considered as a semi-infinite solid (due t the high thickness ratio of the substrate to the thin film) with a Neo-Hookean constitutive law describing it's stress strain relation accounting for large deformations. In order to expand the highly nonlinear deformation field inside the substrate the perturbation method was used resulting in the term found in equation (4.4).

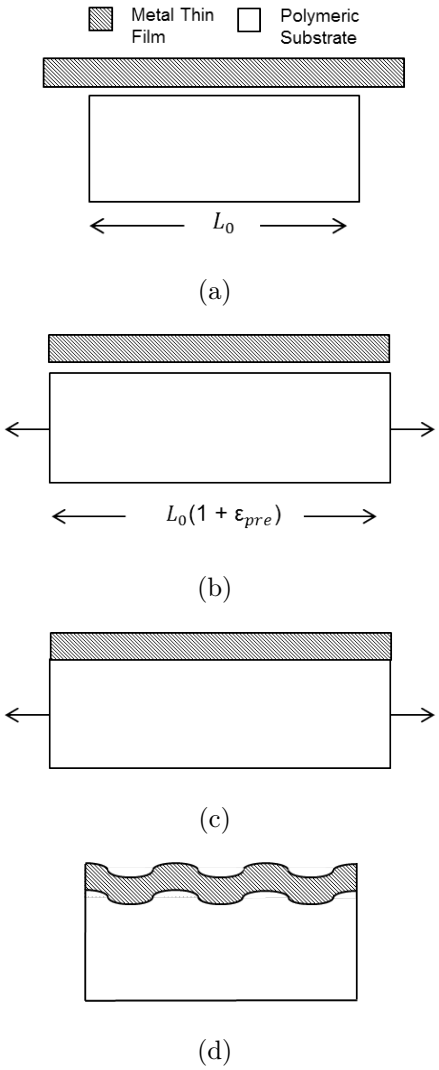

Figure 4.3: The analogous problem to be used for solving the transversal buckling problem; (a) The initial condition with substrate of length L_0 and the longer thin film unattached, (b) The substrate is subjected to pre-stretch to match with the metal thin film's length (still unattached), (c) The metal thin film is attached to the pre-stretched substrate, (d) the system of the attached metal thin film and the substrate are released which results in the buckled configuration

$$U_b = \frac{\pi^4}{3}\frac{\bar{E}_f h^3 A^2}{\big((1+\varepsilon_{pre})\lambda\big)^4}(1+\varepsilon_{pre}) = \frac{k^4 \bar{E}_f h^3}{48(1+\varepsilon_{pre})^3}A^2 \tag{4.1}$$

$$
\begin{aligned}
U_m &= \frac{1}{2}\bar{E}_f h\left[\frac{\pi^2 A^2}{(1+\varepsilon_{pre})^2\lambda^2} - \frac{\varepsilon_{pre}}{1+\varepsilon_{pre}}\right]^2 (1+\varepsilon_{pre}) = \\
&= \frac{1}{2}\bar{E}_f h\left(\frac{k^2 A^2}{4(1+\varepsilon_{pre})^2} - \frac{\varepsilon_{pre}}{1+\varepsilon_{pre}}\right)^2 (1+\varepsilon_{pre}) = \\
&= \frac{\bar{E}_f h}{2(1+\varepsilon_{pre})}\left(\frac{k^2 A^2}{4(1+\varepsilon_{pre})} - \varepsilon_{pre}\right)^2 = \\
&= \frac{\bar{E}_f h}{2(1+\varepsilon_{pre})}\left(\frac{k^4 A^4}{16(1+\varepsilon_{pre})^2} - \frac{k^2 A^2 \varepsilon_{pre}}{2(1+\varepsilon_{pre})} + \varepsilon_{pre}^2\right)
\end{aligned} \tag{4.2}
$$

$$
U_m = \frac{\bar{E}_f h k^4}{32(1+\varepsilon_{pre})^3} A^4 - \frac{\bar{E}_f h k^2 \varepsilon_{pre}}{4(1+\varepsilon_{pre})^2} A^2 + \frac{\bar{E}_f h \varepsilon_{pre}^2}{2(1+\varepsilon_{pre})} \tag{4.3}
$$

$$
U_s = \frac{\pi}{3}\frac{\bar{E}_s A^2}{\lambda}\left(1 + \frac{5\pi^2 A^2}{32\lambda^2}\right) = \frac{\bar{E}_s k}{6} A^2 + \frac{5\bar{E}_s k^3}{768} A^4 \tag{4.4}
$$

Where $\bar{E}_f = E_f/(1-\nu_f^2)$ is the plain strain modulus of the thin metal film, $\bar{E}_s = E_s/(1-\nu_s^2)$ is the plain strain modulus of the substrate, E_f and ν_f are the Young's modulus and Poisson's ration of the thin metal film respectively, E_s and ν_s are the Young's modulus and Poisson's ration of the substrate respectively, h is the thin film thickness, ε_{pre} is the prestrain applied to the substrate before attaching of the thin film which will be responsible for the buckling to happen, A and k are the wave amplitude and the wave number of the buckled configuration, respectively. The latter quantities are the two key parameters needed to define the displacement field in the buckled configuration.

The total strain energy is then the summation of the membrane (U_m) and bending energy (U_b) of the film plus the strain energy of the substrate (U_s). It is convenient to rewrite the total energy term in a polynomial form of the parameter A for ease of further differentiations.

$$
U(A,k) = U_b + U_m + U_s = \alpha + \beta(k)A^2 + \gamma(k)A^4 \tag{4.5}
$$

where α, β and γ are given in the equations (4.6), (4.8) and (4.10), respectively.

$$\alpha = \frac{\bar{E}_f h_f \varepsilon_{pre}^2}{2(1+\varepsilon_{pre})} \tag{4.6}$$

$$\begin{aligned}\beta &= \frac{\bar{E}_f h^3 k^4}{48(1+\varepsilon_{pre})^3} + \frac{\bar{E}_s k}{6} - \frac{\bar{E}_f h k^2 \varepsilon_{pre}}{4(1+\varepsilon_{pre})^2} = \\ &= \frac{1}{2}\bar{E}_f h \left(\frac{h^2 k^2}{24(1+\varepsilon_{pre})^3} + \frac{\bar{E}_s}{3\bar{E}_f h_f k} - \frac{\varepsilon_{pre}}{2(1+\varepsilon_{pre})^2} \right) k^2\end{aligned} \tag{4.7}$$

$$\beta = \frac{1}{2}\bar{E}_f h k^2 \left(f - \frac{\varepsilon_{pre}}{2(1+\varepsilon_{pre})^2} \right) \tag{4.8}$$

$$f = \frac{h^2 k^2}{24(1+\varepsilon_{pre})^3} + \frac{\bar{E}_s}{3\bar{E}_f h_f k} \tag{4.9}$$

$$\gamma = \frac{\bar{E}_f h k^4}{48(1+\varepsilon_{pre})^3} + \frac{5\bar{E}_s k^3}{768} \tag{4.10}$$

In order to find the equilibrium, the total energy was differentiated with respect to A and k in a row. Firstly, the first derivative of the total energy with respect to A was found and put equal to zero.

$$\frac{\partial U(A,k)}{\partial A} = 0 \Rightarrow 2\beta A + 4\gamma A^3 = 0 \tag{4.11}$$

$$A \neq 0 \Rightarrow 2\beta + 4\gamma A^2 = 0 \Rightarrow A_{eq}(k) = \pm\sqrt{\frac{-\beta}{2\gamma}} \tag{4.12}$$

In order to have a nontrivial (a non-zero solution for A) and non-imaginary solution to the equilibrium, as it is depicted also in the two parts of Figure 4.4, it was needed to have $\beta < 0$ which would imply:

$$f \leq \frac{\varepsilon_{pre}}{2(1+\varepsilon_{pre})^2} \tag{4.13}$$

The equation (4.13) dictates the fact that the buckling takes place depending on a condition which is a function of the material properties of the system, its the geometry and the prestrain (ε_{pre}).

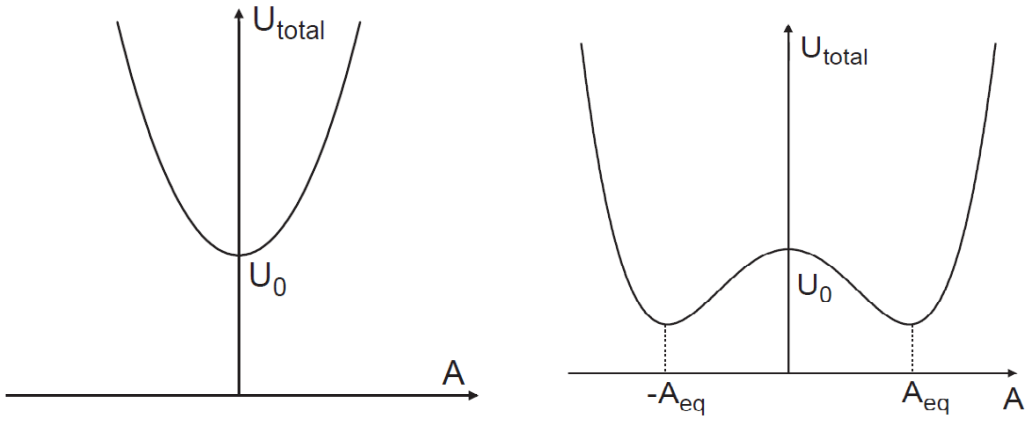

(a) (b)

Figure 4.4: The total energy versus the wave amplitude in two cases (Huang et al., 2005);(a) no buckling configuration i.e. equilibrium occurring with $A = 0$, (b) buckling configuration i.e. equilibrium occurring with $A \neq 0$

The equality case for equation (4.13) will give us the critical prestrain needed for the buckling to begin. Putting the equation (4.12) (A in equilibrium) in the equation (4.5) the total energy only as a function of k was found and then was differentiated with respect to k and put equal to zero. The result revealed the equilibrium wave number and the equilibrium wavelength consequently.

$$U(k) = U(A_{eq}, k) = \alpha + \beta A_{eq}^2 + \gamma A_{eq}^4 \tag{4.14}$$

$$\frac{dU(k)}{dk} = 0 \tag{4.15}$$

From the equation (4.15), k_{eq} was to be found and inserted in equation (4.9) (the definition of the term f) to find the critical strain as a function of the material properties and geometry (i.e. the film thickness).

The problem was solved using the commercial package Mathematica (Wolfram, Oxfordshire, United Kingdom). The solution was found to be too lengthy to be reported in explicit and closed form but the plotted results will be reported and

compared in chapter 5. The original approach to find the equilibrium for a function of two variables such as the case for $U = U(A, k)$, is to take derivatives of U with respect to A and k and then solving the system of equations simultaneously to find the k_{eq} and A_{eq}. In continue, the point found should be checked with the conditions of equations (4.17) and (4.18), based on the determinate of the hessian matrix, to make sure that the point is representing a minimum and not a maximum or even a saddle point. Equivalently the other method as explained previously was used, due to its convenience, but was double checked by the original approach as well. The equivalence of the two approaches is based on the fact that U is a polynomial function of both A and k and so the mixed partial derivatives are equal as seen in equation (4.19).

$$\begin{cases} \frac{\partial U}{\partial A} = 0 \\ \frac{\partial U}{\partial k} = 0 \end{cases} \tag{4.16}$$

$$\frac{\partial^2 U}{\partial A^2}\frac{\partial^2 U}{\partial k^2} - \left(\frac{\partial^2 U}{\partial A \partial k}\right)^2 > 0 \qquad for \qquad (A_{eq}, k_{eq}) \tag{4.17}$$

$$\frac{\partial^2 U}{\partial A^2} > 0 \quad , \quad \frac{\partial^2 U}{\partial k^2} > 0 \tag{4.18}$$

$$\frac{\partial^2 U}{\partial A \partial k} = \frac{\partial^2 U}{\partial k \partial A} \tag{4.19}$$

The results were found for two sets of material properties and geometry. The first case was the same properties used by Song et al. in order to be compared with the reported results in their paper which can be found in Table 4.1, and the second was the properties concerning the transversal buckling problem matching the specimens tested previously as reported in Table 4.2.

Table 4.1: The material properties used to compare the results with the published results of Song et al. (Si thin film and PDMS substrate)

Thin Film			Substrate	
$E_f[GPa]$	ν_f	$h_f[\mu m]$	$E_s[GPa]$	ν_s
130	0.27	0.1	1.8×10^{-3}	0.48

Table 4.2: The material properties used to to match the specimens of the experimental tests (Al thin film and PI substrate)

Thin Film			Substrate	
$E_f[GPa]$	ν_f	$h_f[\mu m]$	$E_s[GPa]$	ν_s
72	0.3	1	3.179	0.5

4.2.2 Imperfect Bond Interface Model

In the experimental tests performed to study the transversal buckling, the buckling of the thin film was always accompanied with the delamination of the thin film from the substrate. This means that considering the lower stiffness of the interface, the upper surface of the substrate wouldn't buckle with the thin film and instead, the film delaminates from the substrate while buckling. Based on this observation it was meaningful to consider a non-perfect interface between the thin film and the substrate so that the substrate is assumed not to deform in the buckling direction. Since again an energy method was chosen to solve the problem the energy term representing the strain energy in the substrate was replaced with a term defining the deformation energy of the interface. In order to do so the problem was again modeled with the general configuration found in Figure 4.1 but with the difference that the thin film was considered as a beam on a Winkler foundation, as presented in Lucchini (2014). Figure 4.5 shows a schematic of the problem considered with the Winkler foundation. The length L is a characteristic length representing the part of the thin film in which the buckling happens.

The total energy of the system is defined in equation (4.20). The three parts

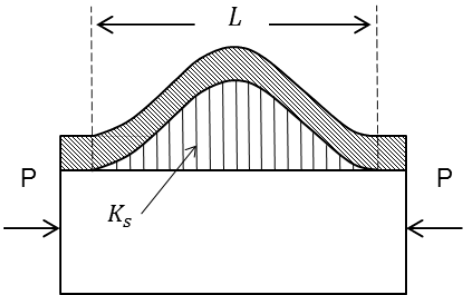

Figure 4.5: The schematic showing the thin metal film as a beam on a Winkler foundation to define the problem of buckling with non-perfect interface

of the total energy are recognizable inside the integral which in order are bending energy of the thin film, its membrane energy and the interface deformation energy. For the sake of simplicity, all the materials are considered linear elastic in this case. The tensile stress acting in the axial direction as well as the shear stress in the interface are neglected.

$$U(w) = \int_{-\frac{L}{2}}^{\frac{L}{2}} \left[EIw'' - Pw'^2 + k_s W_s w^2 \right] dx \tag{4.20}$$

Where L is the length representing the part of the thin film in which the buckling happens, E is the Young's modulus of the thin film, I is the second moment of area of the cross section of the thin film, P is the compressive force applied to the thin film due to the compressive strain thin the substrate, k_s is the stiffness of the Winkler foundation interface, W_s is the out of plane width of the thin film and w is the vertical displacement of the thin metal film defining the buckled configuration.

The relation between the compressive strain in the transversal direction and the compressive force induced on the thin film can be found in the equation (4.21).

$$\varepsilon_{transversal} = \frac{P}{EA_s} \tag{4.21}$$

where $A_s = W_s t$ is the cross sectional area of the thin metal film. The critical case resulting in buckling is consequently defined as:

$$\varepsilon_{cr} = \frac{P_{cr}}{EA_s} \tag{4.22}$$

Where ε_{cr} and P_{cr} are critical transversal strain and force respectively.

The displacement field, w can be defined in a general form as in equation (4.23) as a summation of a series of cosine waves with different wavelengths. For the sake of simplicity of the model a single term displacement field was chosen defined by a cosine wave as can be found in (4.24).

$$w = \sum_i A_i \left[\cos\left(2\pi i \frac{x}{L}\right) + 1\right] \tag{4.23}$$

$$w = A_1 \left[\cos\left(2\pi \frac{x}{L}\right) + 1\right] \tag{4.24}$$

$$w' = -\frac{2\pi A_1}{L} \sin\left(2\pi \frac{x}{L}\right) \tag{4.25}$$

$$w'' = -\frac{4\pi^2 A_1}{L^2} \cos\left(2\pi \frac{x}{L}\right) \tag{4.26}$$

Calculating the first and second derivatives of w and inserting the equations (4.24), (4.25) and (4.26) in the equation (4.20) the total energy was found to be:

$$\begin{aligned} U(A_1) = \int_{-\frac{L}{2}}^{\frac{L}{2}} EI \left\{ -A_1 \frac{4\pi^2}{L^2} \cos\left(\frac{2\pi x}{L}\right) \right\}^2 - P \left\{ -\frac{2\pi A_1}{L} \sin\left(\frac{2\pi x}{L}\right) \right\}^2 + \\ + k_s W_s \left\{ A_1 \left[\cos\left(\frac{2\pi x}{L}\right) + 1\right] \right\}^2 dx \end{aligned} \tag{4.27}$$

The integrals found in the equation (4.28) was used to simplify the total energy term resulting in the form found in equation (4.29).

$$\int_{-\frac{L}{2}}^{\frac{L}{2}} \left\{ \cos\left(\frac{2\pi x}{L}\right) \right\}^2 dx = \int_{-\frac{L}{2}}^{\frac{L}{2}} \left\{ \cos\left(\frac{2\pi x}{L}\right) \right\}^2 dx = \frac{L}{2} \tag{4.28}$$

$$U(A_1) = \frac{A_1^2}{2} \left(EI \frac{8\pi^4}{L^3} - P \frac{2\pi^2}{L} + \frac{3}{2} k_s W_s\right) \tag{4.29}$$

In continue, the instability condition was applied to the total energy which led to finding the critical value of P (equation (4.32)).

$$\frac{\partial^2 U}{\partial A_1^2} = 0 \tag{4.30}$$

$$EI\frac{16\pi^4}{L^4}\frac{L}{2} - P\frac{4\pi^2}{L^2}\frac{L}{2} + k_s W_s \frac{3}{2} = 0 \tag{4.31}$$

$$P_{cr} = \frac{4EI\pi^2}{L^2} + k_s W_s \frac{3}{4}\frac{L^2}{\pi^2} \tag{4.32}$$

Utilizing the equation (4.22) the critical strain in the transversal direction was found as:

$$\varepsilon_{cr} = \frac{4I\pi^2}{A_s L^2} + k_s W_s \frac{3}{4}\frac{L^2}{EA_s\pi^2} \tag{4.33}$$

And by inserting the second moment of area for the thin film cross section as $I = \frac{W_s t^3}{12}$ the critical strain is found explicitly as:

$$\varepsilon_{cr} = \frac{4t^2\pi^2}{12L^2} + k_s \frac{3}{4}\frac{L^2}{Et\pi^2} \tag{4.34}$$

Two non-dimensional parameters were defined and the critical strain was rewritten as a function of these two parameters, λ and β.

$$\begin{aligned} \lambda &= \frac{L}{t} \\ \beta &= \frac{k_s t}{E} \end{aligned} \tag{4.35}$$

$$\varepsilon_{cr} = \frac{\pi^2}{3\lambda^2} + \frac{3}{4}\frac{\beta\lambda^2}{\pi^2} \tag{4.36}$$

Considering the definition of the displacement field in the thin film (equation (4.24)), L and consequently the non-dimensional parameter λ represent the length on which the buckling happens which could be referred to as the wavelength of buckling. It should be noted that equation (4.36) represents the instability condition based on

two variables; the critical strain and the wavelength. Different combinations of these two parameters can define the critical condition, though the one representing the lowest energy can be found as the minimum of the curve ε_{cr} against λ. Considering the application of the strain which leads to the buckling, the minimum of the curve is actually the first critical condition to be satisfied defining the actual critical condition of the problem.

The value for the interface stiffness, k_s, was obtained form another work conducted in the research group (Lucchini, 2014) where was estimated by simulating the experimental tests performed on the specimens modeled in ABAQUS. In the above mentioned work, the interface was modeled by cohesive elements and a user defined traction-separation law introduced by means of a FORTRAN based subroutine. Figure 4.6 shows the traction-separation law governing the interface between the thin Al film and the PI substrate with regulated parameters matching the experiments. For the case matching the experiments, two values of k_s were found as the higher and lower bound as a tangential stiffness at $\delta_n = 0$ and a secant stiffness based on the peak of the curve, respectively. The values found by Lucchini (2014) were $2500 MPa/mm$ and $1000 MPa/mm$ for the higher and lower bound, respectively. The results were studied not only for the experimental k_s but also for three other cases of ten times higher, ten times lower and one hundred times lower values, to check the effect of the interface stiffness on the critical strain leading to buckling and the resulting wavelength. The detailed results will be discussed in chapter 5. The material system concerning the rest of the model was chosen as reported in Table 4.2 to match the specimens tested.

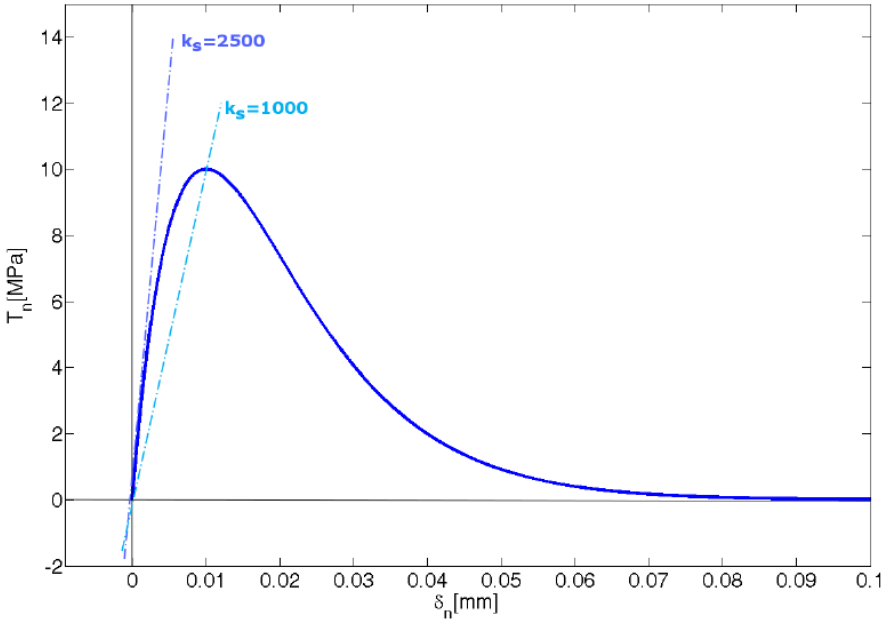

Figure 4.6: The curve showing the traction separation law governing the interface between the thin Al film and the PI substrate with regulated parameters matching the experiments (Lucchini, 2014)

4.3 Analytical Model for Meander Buckling During Unloading

To study the possible buckling of the thin metal film in the meanders of a S shaped interconnect used for stretchable electronics, another analytical model was developed. The meander buckling problem was defined in a plain strain, two dimensional case looking at the meander and substrate cross section as depicted in Figure 4.7.

The procedure happening in the meanders that can result in buckling of the thin film is depicted in three steps in Figure 4.8. The meander is modeled as a straight thin metal film lying on and attached to the thick polymeric substrate. The system is stretched in the axial direction. As can be seen in Figure 4.7 the stretch direction in Figure 4.8 is the axial direction of the whole stretchable interconnect, so it will be referred to as axial direction. The stretching goes on up to inducing a considerable

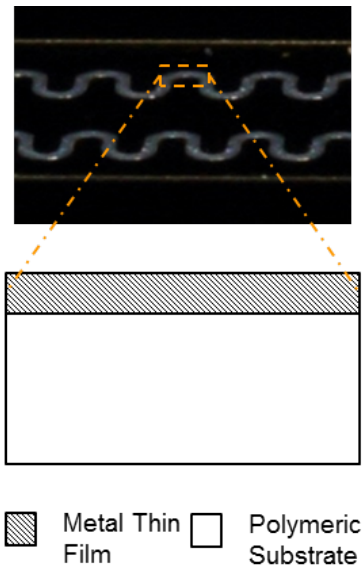

Figure 4.7: The cross sectional view of the meander of the S shaped interconnects to define the meander buckling problem

amount of plastic deformation inside the thin metal film. In continue the system is unloaded, as if it would happen in a case of a stretchable electronic designed to be subjected to at least a couple of loading-unloading cycles. During unloading, the polymeric substrate, which is initially considered elastic, tends to go back to its original configuration but the thin metal film having trapped some plastic strain inside does not. The result is the buckling of the thin film.

To solve the meander buckling problem as stated above, an analogy was castes between the actual case study and the Song model already exploited for the buckling of transversal parts. Figure 4.8 gives a definition of the analogous problem. However, this time the analogy is found in different parameters. As explained through five different stages of loading and unloading in Figure 4.9, the analogy between the two problems was found through the analogy between the prestrain in the problem solved by Song et al. and the plastic strain in the meander buckling problem. In Figure 4.9(a) the analogous problem is summarized. The thin metal film goes through compression induced by the prestrain of the substrate and if the stress inside

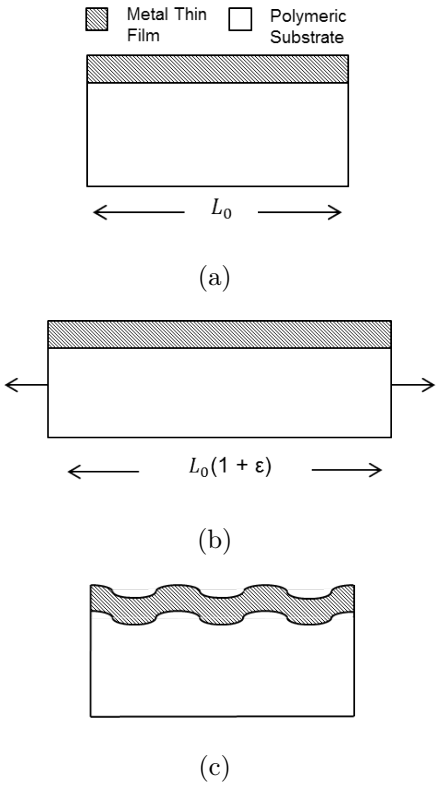

Figure 4.8: The definition of the problem of meander buckling and the procedure leading to buckling; (a) The thin metal film attached to the polymeric substrate representing the meander part of a S shaped interconnect, (b) The system is stretched (axial direction of the whole interconnect) up to a point to induce a considerable amount of plastic deformation inside the thin metal film ($\varepsilon = \varepsilon_{elastic} + \varepsilon_{plastic}$), (c) The stretched system is then released and buckling can occur during unloading

the thin metal film passes a critical value, the buckling happens. In Figure 4.9(b) through 4.9(f) the meander buckling problem is illustrated. Firstly, in Figure 4.9(b) the loading of the meander is shown up to inducing some plastic strain in the metal film. An amount of plastic strain which will -in the next steps- be found not to be sufficient to induce buckling. Secondly, in Figure 4.9(c) unloading of the previously stretched system, back to elastic recovery of the thin metal film is shown. In Figure 4.9(d) the same unloading in the previous step is continued back to the initial length ($\varepsilon_{total} = 0$). It is observed that the thin metal film after complete unloading, will not

arrive at the critical stress needed to initiate the buckling. However, it is observed in Figure 4.9(e) that if the same procedure is performed but with loading the system more than before and to induce more plastic strain in the thin metal film, the complete unloading can put the thin film into enough compressive stress for the buckling to initiate. In other words, there are two possible cases: (I) if the plastic strain is less than a critical value, when going back to $\varepsilon_{total} = 0$ the film is compressed but below its critical value for buckling (II) if the plastic strain is more than a critical value, when reaching $\varepsilon_{total} = 0$ the compressive stress within the film overcomes the critical value to induce buckling of the film. The smallest amount of plastic strain resulting in the buckling of the meander after complete unloading is the critical plastic strain. The state of the thin film depicted in Figure 4.9(c) is an updated stress free configuration of the thin film which is the initiation point of the analogy. If compared with Figure 4.9(a) it is observed that the plastic strain is exactly matching with the prestrain of the analogous problem to confirm the analogy between the two cases. As sketched in Figure 4.9(f) if the loading is taken even further as to aggregate more plastic strain in the thin metal film, even before the complete unloading the buckling is initiated.

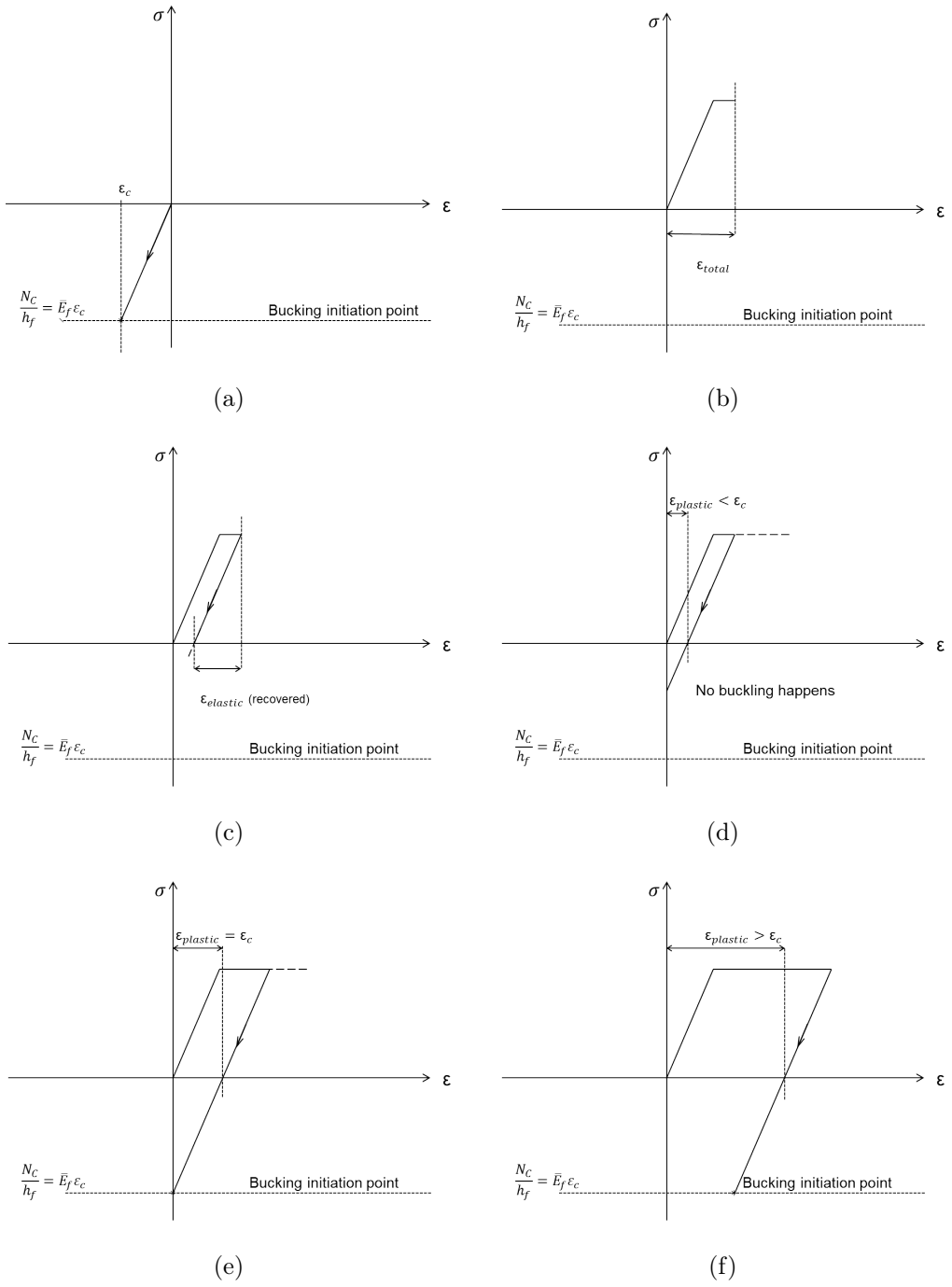

Figure 4.9: The study of the analogy between prestrain and plastic strain; (a) the analogous problem, (b) the original problem: just loading (elastic-perfectly plastic model), (c) The original problem: unloading up to elastic recovery, (d) the original problem: complete unloading - no buckling occurs, (e) the original problem: complete unloading - The first instance of buckling, (f) the original problem: complete unloading - buckling

Having established the analogy, the solution of the analogous problem was used to solve the problem to be dealt with, in this section. The solution to the analogous problem was exactly the same at explained before in section 4.2. Replacing the prestrain in the solution by the plastic strain the results concerning the meander buckling problem were found. Two cases of material properties were examined. First the case with material properties as found in Table 4.2 to match the specimens tested in the current study. And another, the case with material properties which is reported in Table 4.3 as a system with a perfectly elastic substrate which related results could have been found in the literature as well. The results will be discussed in chapter 5.

Table 4.3: The material properties with a perfectly elastic substrate (Au thin film and PDMS substrate)

Thin Film			Substrate	
$E_f[GPa]$	ν_f	$h_f[\mu m]$	$E_s[GPa]$	ν_s
77.2	0.42	1	1.8×10^{-3}	0.48

The present model was extended to a further step. Since the PI substrate showed itself to be phenomenologically plastic (refer to section 3.3), there was the need to introduce the plasticity of the substrate inside the model. The plasticity in the substrate can affect the meander buckling extensively, since irreversibility inside the substrate would mean that the completely unloaded system is not of the original length. So the plastic strain of the substrate was to be accounted for as well. In this case the amount of plastic strain trapped inside the substrate should be compared to the plastic strain of the thin film and then check with the buckling criterion. In Figure 4.10 four different cases of the problem can be found. For the sake of simplicity of presentation in this Figure the materials are depicted as elastic and perfect plastic. In each of the four cases, the system is loaded up to inducing plasticity inside both the thin metal film and the substrate. The end point of loading is shown by a vertical dashed line in each image. Each case is then unloaded

back to the equilibrium which is dictated by the substrate due to its much higher thickness. This unloaded equilibrium state is shown by another vertical dashed line in each image, representing the point of complete elastic recovery of the substrate. Different plastic properties of the substrate, specifically the yield strain, result in different final equilibrium states which will be discussed in here. Figure 4.10(a) shows the case in which the plastic strain of the thin metal film is smaller than the plastic strain in the substrate. With this condition, the thin film remains in tension even when the unloaded equilibrium is achieved so the buckling cannot happen. In the case illustrated in Figure 4.10(b) the plastic strain in the thin metal film is equal to that of the substrate so the unloaded equilibrium is a stress free state for both the substrate and the thin metal film. Being stress free, no buckling can happen again. The two last cases i.e. Figure 4.10(c) and 4.10(d) show the case that the thin film is experiencing more plastic strain than the substrate at the end of the loading so after unloading and when arrived at the unloaded equilibrium, the thin film goes in compression. The amount of compressive stress trapped inside the thin film depends on the difference between the plastic strain of the thin metal film and that of the substrate, a difference which can be called the plastic strain offset. Figure 4.10(c) shows a case in which the plastic strain offset is positive but not enough to induce buckling, while Figure 4.10(d) shows a case where the bucking happens considering the big difference between the plastic strain in thin film and substrate, thus the big enough plastic strain offset. So it is comprehended that the meander buckling problem should be revised taking into account the plasticity of the substrate since this phenomenon cannot be neglected considering it capacity to prevent buckling in cases which the buckling would have occurred with a elastic substrate.

In all the cases of Figure 4.10 the materials are shown as elastic - perfect plastic however in the model solved in the present study, the real work hardening laws derived from the experiments have been used. The procedure for obtaining the plastic properties of PI was discussed in section 3.3 and the aluminum properties were found in another work done in the research group (Lucchini, 2014). Figure

4.11 shows the case of bucking with plasticity in the substrate, considering a simple linear hardening law to show that the same discussion is valid also in the case of work hardening. It can be easily grasped from the discussion above, that in this case the analogy should have been defined again. In this case the analogy is valid between the prestrain of the analogous problem and the plastic strain offset of the present problem. The plastic strain offset was obtained as discussed in continue. The total strain is equal for both the thin film and the substrate and equal to the sum of the plastic and elastic strain for each.

$$\varepsilon_{total} = \varepsilon_{elastic-film} + \varepsilon_{plastic-film} = \varepsilon_{elastic-substrate} + \varepsilon_{plastic-substrate} \tag{4.37}$$

The plastic strain offset is defined as the difference between the plastic strains of the thin film and the substrate.

$$\varepsilon_{plastic-offset} = \varepsilon_{plastic-film} - \varepsilon_{plastic-substrate} \tag{4.38}$$

From the two equations above, the plastic strain offset is found as a function of the elastic strain of the thin film and the substrate. In this way, considering the relation between the elastic strain and the true stress and the fact that the true stress as a function of the total applied true strain was available from the test results the plastic strain offset was found as seen below:

$$\varepsilon_{plastic-offset} = \varepsilon_{plastic-film} - \varepsilon_{plastic-substrate} = \varepsilon_{elastic-substrate} - \varepsilon_{elastic-film} \tag{4.39}$$

$$\varepsilon_{elastic-substrate} = \frac{\sigma_{true-substrate}(\varepsilon)}{\bar{E}_{substrate}} \tag{4.40}$$

$$\varepsilon_{elastic-film} = \frac{\sigma_{true-film}(\varepsilon)}{\bar{E}_{film}} \tag{4.41}$$

$$\varepsilon_{plastic-offset} = \frac{\sigma_{true-substrate}(\varepsilon)}{\bar{E}_{substrate}} - \frac{\sigma_{true-film}(\varepsilon)}{\bar{E}_{film}} \tag{4.42}$$

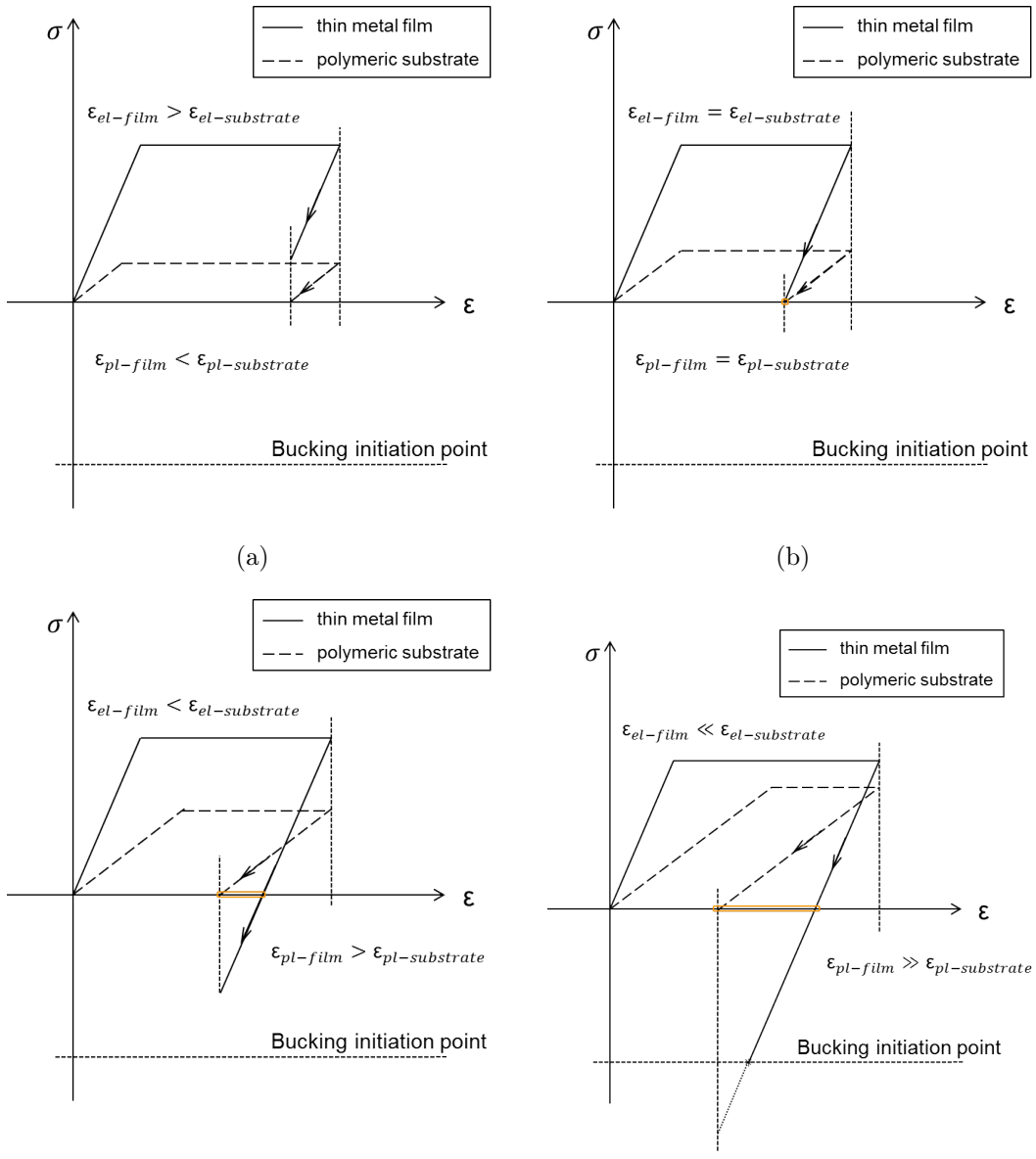

Figure 4.10: The effect of plasticity in the substrate on the meander buckling problem; (a) the plastic strain offset is negative - the thin metal film remains in tension, (b) the plastic strain offset is zero - the thin metal film remains stress free, (c) the plastic strain offset is positive (thin metal film in compression) but not big enough to induce buckling, (d) the plastic strain offset is positive (thin metal film in compression) and big enough to induce buckling

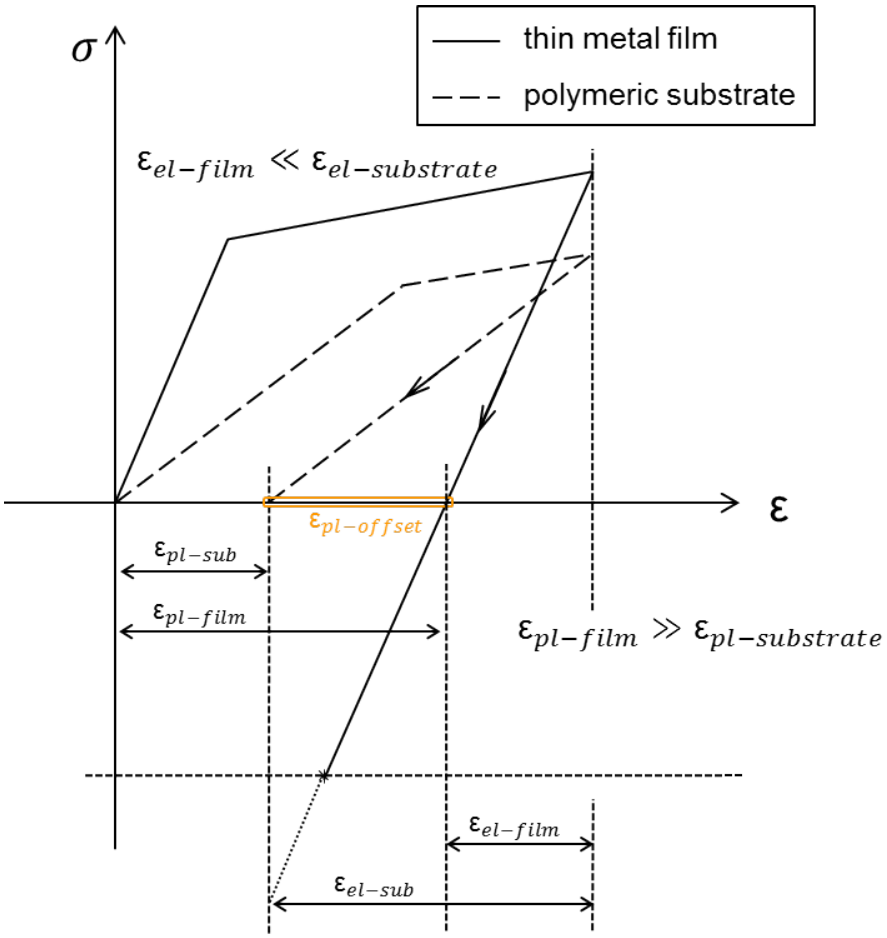

Figure 4.11: The case of the meander buckling with plasticity in the substrate considering work hardening in both the thin film and the substrate

4.4 Finite Element Model

A plain strain model of the transversal part of the S shaped interconnects used in stretchable electronics was created in ABAQUS 6.12 (Dassault Systemes, France), to study the buckling and delamination of the thin metal film on the polymeric substrate. As seen in Figure 4.12 the model represents a cross section of the transversal part in the direction perpendicular to the axis of a stretchable interconnect. The model was consisted of a PI substrate of $10\mu m$ thickness, an Aluminum film of $1\mu m$ thickness and $0.01\mu m$ thick (one hundredth of thin film thickness) interface all with a $100\mu m$ length. The PI and Al were modeled elastic and the interface was modeled using a traction separation law to be discussed in continue.

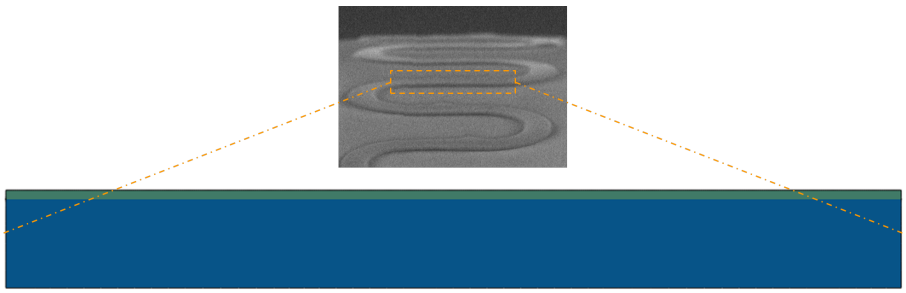

Figure 4.12: The cross sectional view of the transversal part of the S shaped interconnects to define the finite element model

As can be seen in Figure 4.13 the model is consisted of four different materials. The Thin metal film is depicted with color green in this figure while the polymeric substrate is shown in blue. Between these two main parts, there is the interface, illustrated in two colors itself. The light gray part of the interface (seen on the right) is representative of the compliant interface used to model the delamination and the red part (on the left) is modeling a stiff interface. This division of the interface into two parts was done to make possible studying the effect of the transversal part length on the buckling to make possible the comparison with the quantitative experimental result and the analytical ones. which will be discussed with more detail in continue.

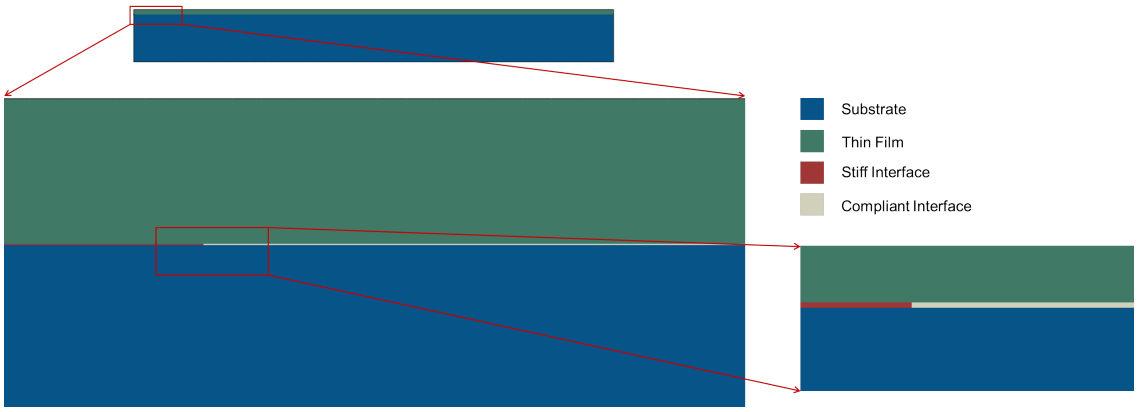

Figure 4.13: Different sections of the finite element model

The boundary condition and loading applied to the model can be seen in Figure 4.14. The two sides of the model were subjected to compression in form of displacement applied. The model was constrained in vertical direction by fixing the vertical displacement of the lower edge. A single point in the center of the lower edge was constrained in axial direction as well to eliminate rigid body motion. As confirmed by preliminary analysis, in order to induce the buckling there was the need to introduce a disturbance to the system. The disturbance was applied as two displacements at the two edges with a negligible amount not to effect the stress and strain distribution in the model. To check whether the unsymmetrical nature of the disturbance could have affected the results, simulation outcomes in cases of both unsymmetrical and symmetrical disturbances configurations were compared. A good match was obtained, specifically as referred to the quantities to be used for validating the analytical models, i.e., the critical strain and the wavelength.

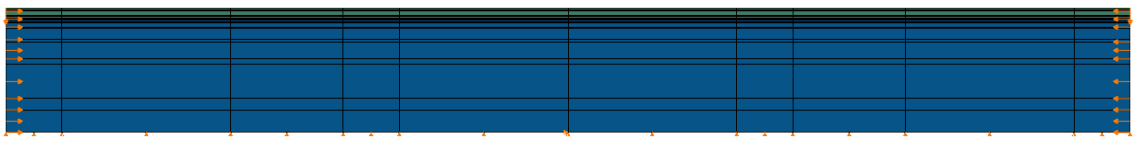

Figure 4.14: The finite element plain strain model of the transversal part showing the boundary conditions as well

The model was finely partitioned for a proper meshing. The element size needed

to be very fine in the interface considering both its small thickness and the importance of its discretization due to its important structural role. On the other hand the mesh needed to be coarse enough far from the interface to lower the computational cost. In order to make this kind of mesh possible in structured form, the model was divided into several partitions in the vertical direction. Starting from the interface going up in the thin metal film section, every other partition was designed to double the mesh size by using triangular elements. The same approach changed the element size in the substrate section of the model starting from the interface going down. In Figure 4.15(a) is seen that the interface is showed by a red color presenting a cohesive element type (COH3D8) while the thin film and the substrate are depicted with two colors of light gray and green for two kinds of plain strain element types. The light gray partitions are showing the quadrilateral plain strain elements (C3D8) and the green ones show the triangular plain strain elements (C3D6). In Figure 4.15(b) the mesh in a zoomed part of the model is visible showing the way this kind of meshing changes the element size in the model. The biggest element was of $0.2\mu m$ and $2\mu m$ long edge in the thin film and the substrate, respectively. The smallest elements found in the interface were of the size $0.01\mu m$ in the vertical and $0.025\mu m$ in the horizontal directions. This element size was chosen as a result of a mesh sensitivity analysis, which was performed to make sure about the reliability of the discretization of the model. As it can be seen in Figure 4.16 the element size was changed in 3 cases in the interface only. In order to maintain the structure mesh the mesh size was changed in the partitions close to the interface as well. The mesh size was changed in the horizontal direction only due to two reasons. Firstly, since the cohesive element should be defined as a single element through its thickness so the element size should have been kept constant in the direction of interface thickness. Secondly, the element size should be significantly lower than the process zone characteristic dimension. Breaking this rule would affect the performance of the interface when entering the softening branch of the traction-separation behavior, introducing numerical oscillations. And it is obvious that the crack growth in this

model was in the horizontal direction only. The different mesh properties are found in 4.4. The relative mesh size is the mesh size of the interface in horizontal direction divided by the thickness of the thin metal film in the model which is $1\mu m$.

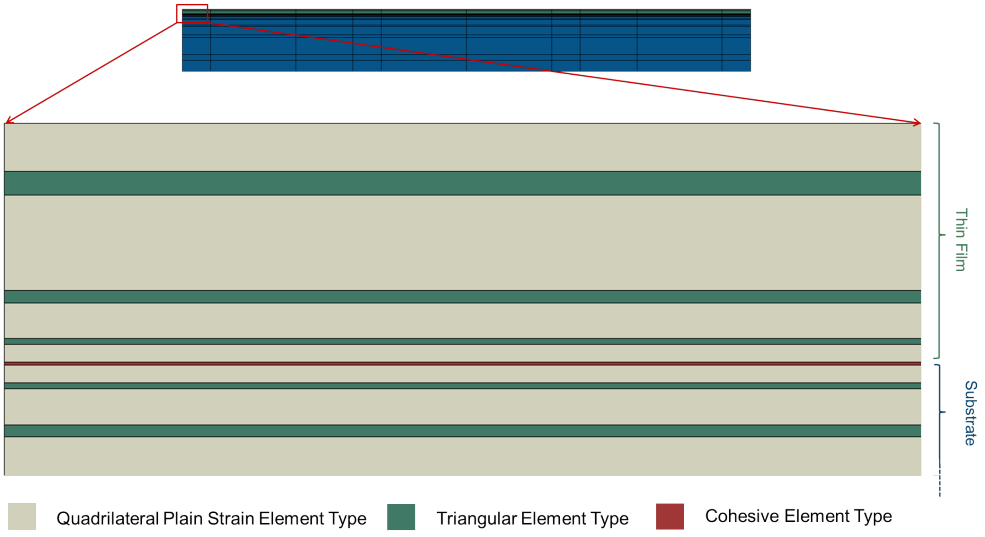

(a)

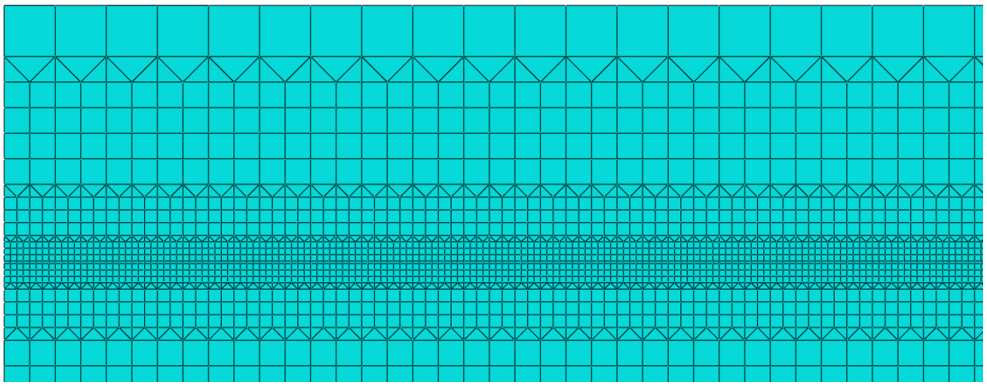

(b)

Figure 4.15: (a) Sectioning of the model with different element types to make possible a well structured mesh, (b) The mesh showing the method to change the element sizes systematically

Two parameters were utilized to perform the mesh sensitivity analysis, the wavelength of buckling (the length on which the film has buckled) and the total reaction force on one side of the model. The plots in Figure 4.17(a) and (c) show the results of

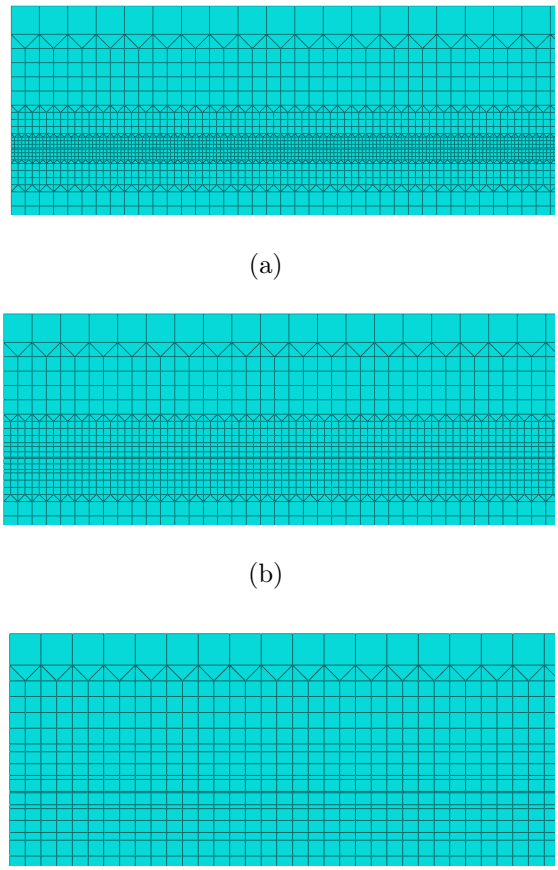

Figure 4.16: Different meshing cases; (a) fine mesh, (b) medium sized mesh, (c) coarse mesh

these two parameters plotted against different meshing cases. In addition to studying these parameters on their own, the Grid Convergence Index (GIC) was used (Roache, 1994). GIC method is based on the Richardson theory of extrapolation. Using three different values of a certain parameter for three different meshing cases, the exact value of the desired parameter is extrapolated. Using this extrapolated value for each meshing case an error can be found and compared. The percentage error found for the wavelength and the reaction force are plotted in Figures 4.17(b) and (d), respectively. It is seen that the absolute values and the errors are converging and moreover the amount of error in all the meshing cases is small.

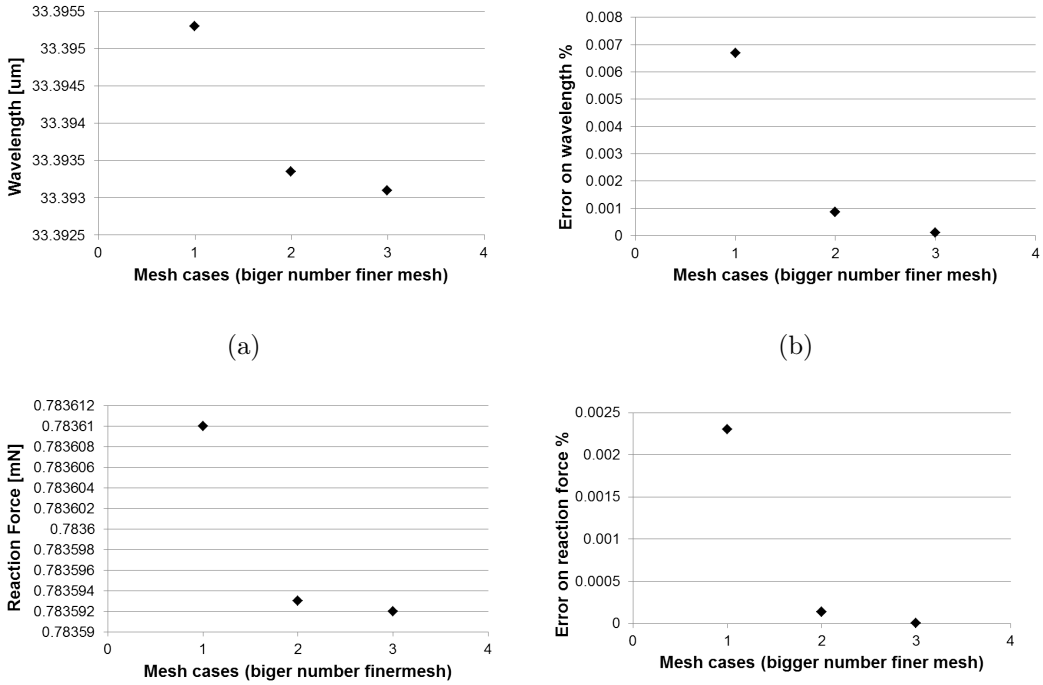

Figure 4.17: Mesh sensitivity analysis results (refer to table 4.4 for the information on each case); (a) the buckling wavelength for different meshing cases, (b) error on the buckling wavelength for different meshing cases, (c) the reaction force for different meshing cases, (d) error on the reaction force for different meshing cases

Table 4.4: The geometric characteristics of different cases for mesh sensitivity analysis

Meshing Case	Relative Mesh Size	Corresponding Image	Corresponding Case in the Curves
Fine	0.025	Figure 4.16(a)	3
Medium	0.050	Figure 4.16(b)	2
Coarse	0.100	Figure 4.16(c)	1

To define the cohesive material properties for the interface, a user defined UMAT subroutine prepared in the research group was used (Lucchini, 2014). The constitutive law was introduced as a traction separation law. The cohesive zone law is constituted as seen in Figure 4.18(a) in the way that the traction in the interface increases with increasing of the interfacial separation up to the point (C). From point (C) on the traction decreases up to the complete delamination at the point

(E). In this way the delamination of the thin film from the substrate was included in the finite element model.

The parameters defining the cohesive zone law i.e. the interface properties were found in the same work in the research group mentioned above (Lucchini, 2014) by confronting simulations and experimental results. The values as can be seen in Figure 4.18(b) were $2500 MPa/mm$ and $1000 MPa/mm$ for the higher and lower bound, respectively. The experimental values for the $k_s$were used to validate the FEM simulation with experimental qualitative results. However, the effect of the interface stiffness was studied in the present numerical study in order to validate the analytical model quantitatively. In addition to the experimental values three other cases of interface stiffness of ten times higher, ten times lower and one hundred times lower values were simulated. These values were corresponding to the same values for the interface stiffness used in the analytical model (check page 48).

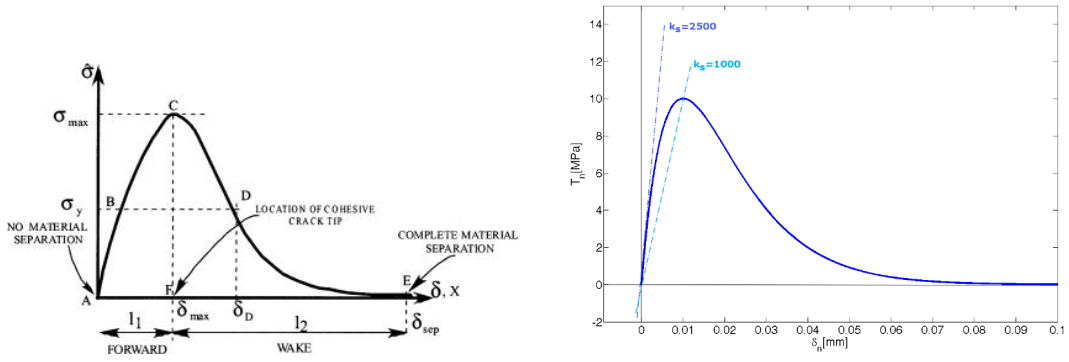

(a) (b)

Figure 4.18: The traction separation law used to define the interface properties; (a) definition of the cohesive zone model (Shet and Chandra, 2002), (b) cohesive zone model parameters based on experiments (Lucchini, 2014)

In the end, the model based on the mesh size established by the sensitivity analysis and the experimental value of the interfacial stiffness was used to study the effect of the transversal part length on the buckling wavelength and critical strain. The different transversal lengths were modeled by exploiting the method explained

on page 59. Introducing a stiff interface as a fourth set of material properties (again using the same UMAT subroutine but with different constants as input) it was possible to constrain the length on which the buckling and delamination could have happened. The material properties for two side parts of the interface was defined as the stiff interface. By changing the length of the these two side parts it was possible to model different lengths simply within the same ABAQUS model. The partitioning done in the horizontal direction seen in Figure 4.14 has been done for this purpose. Four length of $30, 40, 60$ and $90\mu m$ were modeled to be matching the cases of transversal part lengths of the specimens tested. (see table 3.1). A fifth case was modeled as well representing a $100\mu m$ of transversal length that was basically by increasing the length of the whole model to $110\mu m$ and defining the central $100\mu m$ as the compliant interface to have the same boundary condition of buckling as the other cases specifically in terms of the disturbance applied. Figure 4.19 shows all the five cases of the length study. The different interface lengths visible are artificially highlighted, which thus is in reality much thinner than what suggested by the pictorial lines in the images.

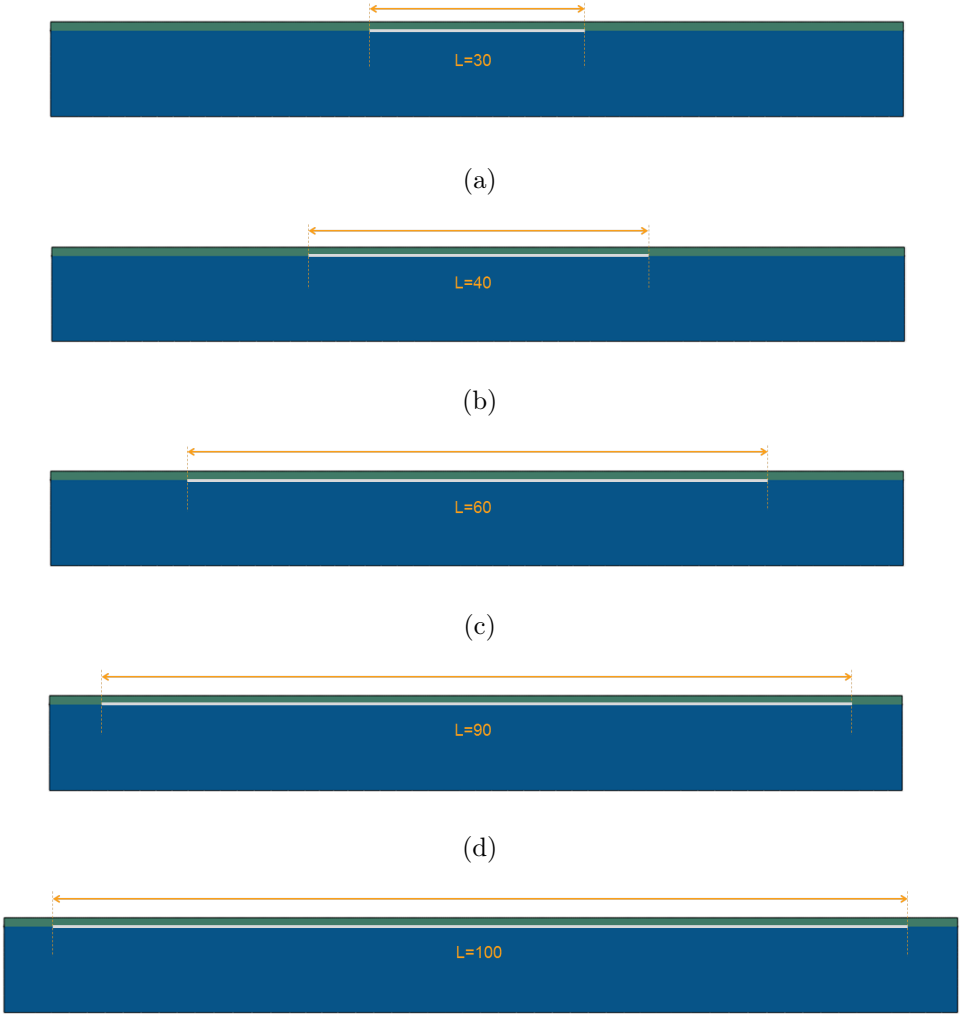

Figure 4.19: The transversal length study in the finite element model; (a) transversal part equal to $30\mu m$, (b) transversal part equal to $40\mu m$, (c) transversal part equal to $60\mu m$, (d) transversal part equal to $90\mu m$,(e) transversal part equal to $100\mu m$

Chapter 5

Results and Discussion

5.1 introduction

In this chapter, the results of the experiments, models and simulations will be discussed. The same as it was structured in the whole thesis, the results will presented and discussed firstly, for the experimental tests performed and basically on the observations of the buckling and delamination. Secondly, the results of the different analytical and numerical models will be reviewed. A more comprehensive discussion on the reliability of analytical and numerical models here developed as compared with experimental results, will be given in chapter 6.

5.2 Experimental Results

The experimental results are introduced divided in three different sections themselves. The experimental results on transversal buckling, the meander buckling and the Polyimide characterization at the real scale will be explained in the mentioned order in the pages to be followed.

5.2.1 Polyimide Characterization in the real scale

Polyimide specimens have been tested in three different manners in order to be mechanically characterized as discussed in section 3.3. The stress strain curve obtained by uniaxial tests on 8 identical PI samples are reported in Figure 5.1. The results concerning the loading with repeated partial unloading tests can be found in Figure 5.2 reported as a load versus displacement curve.

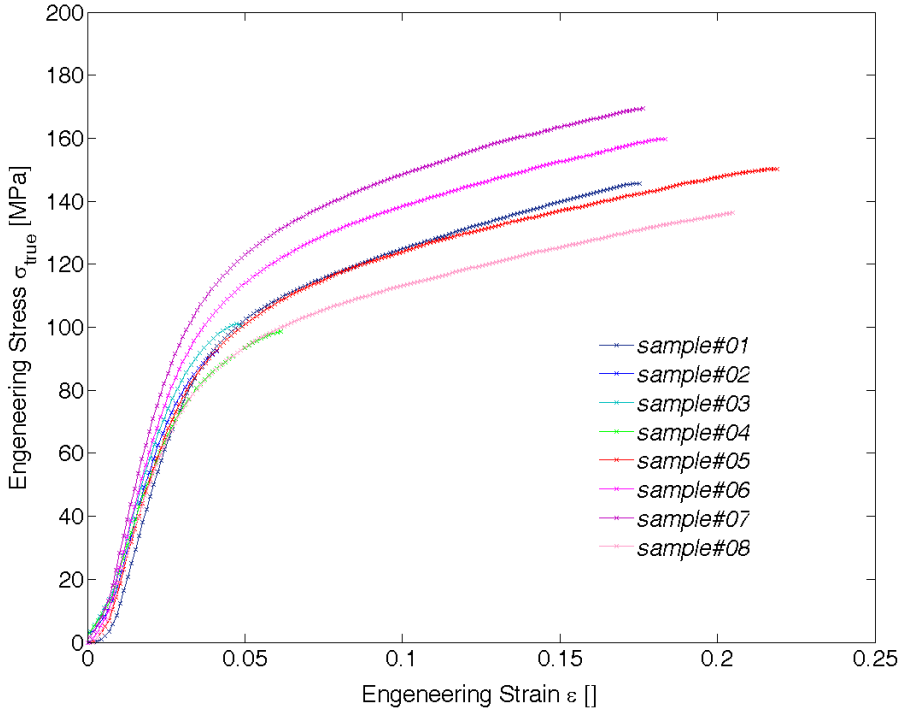

Figure 5.1: Stress strain curves resulted from uniaxial tests performed on a series of PI specimens at $1\mu m/s$

The curve presented in Figure 5.3(a) shows the load displacement curve obtained by the creep test as was explained in section 3.3. Though the irreversibility of the PI specimen is clearly visible in this plot, the plot seen in Figure 5.3(b) gives a better understanding of the phenomenon. The viscoplastic behavior of PI is noticeable and it is expected that the residual deformation would be recovered to a more extent if given more time, however, having in mind the time scale of application

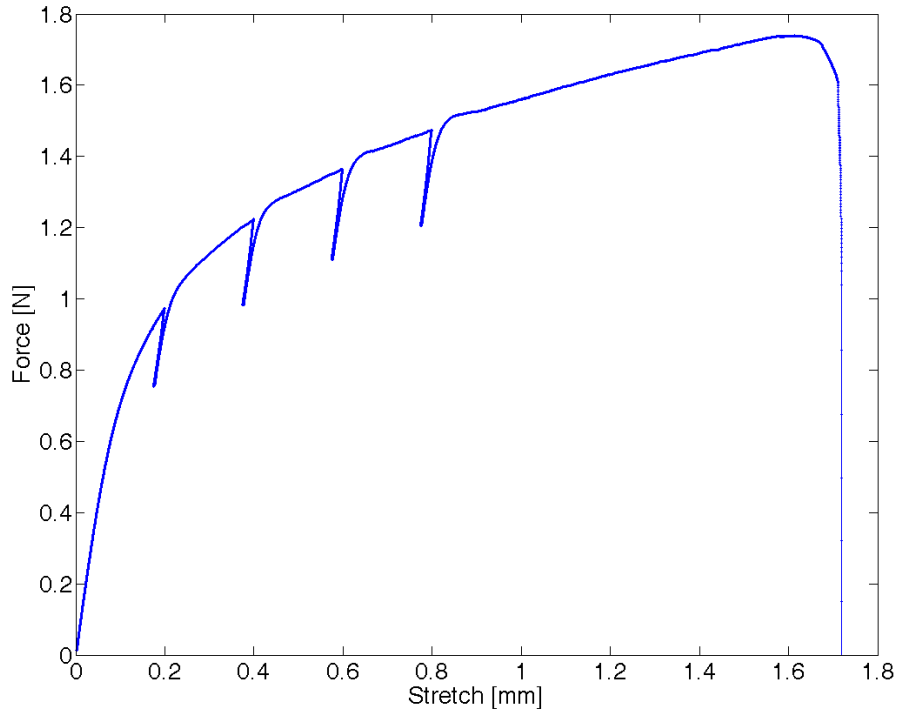

Figure 5.2: Uniaxial tensile test with four partial unloading paths on PI sample at $1\mu m/s$ stretch

of stretchable electronics, the time-dependent behavior was neglected. As a consequence, Polyimide was treated as an elasto-plastic material with isotropic work hardening to match the tensile tests reported previously. The elastic modulus of $3.179MPa$ and a Poisson's ratio of 0.34 were found for the tested specimens which are in agreement with reference literature data (Chang et al., 2008; Jansons et al., 2012; Kuo et al., 2004).

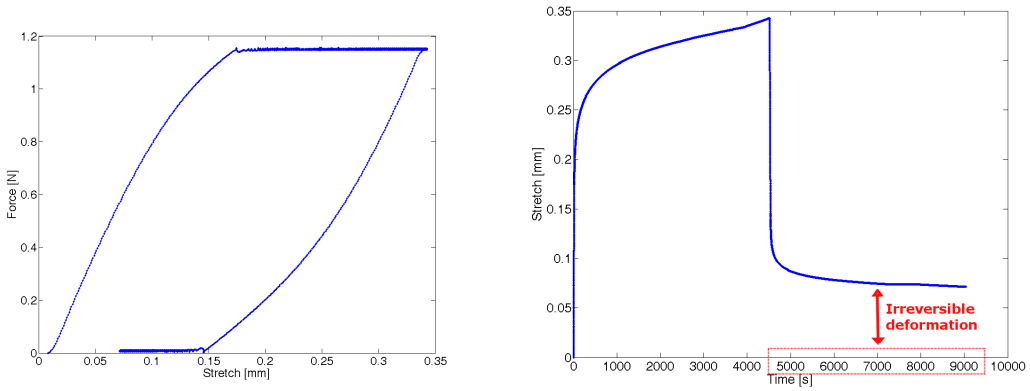

(a) (b)

Figure 5.3: The results of the creep test on the PI specimens; (a) Load-displacement resulted from the creep test, (b) the displacement acquired from the stage during the creep tests showing the irreversibility of Polyimide

5.2.2 Transversal Buckling

Obtained from the tests performed out of the ESEM chamber the global behavior of the specimens were studied. The results concerning the Load-Displacement relation for each specimen are plotted in Figure 5.4. The results are plotted on the same graph to make possible comparing the effect of the interconnect geometry.

What can be observed in the Figure 5.4 is that the geometry of the thin metal film interconnect is almost not affecting the overall load displacement behavior of the whole interconnect. This confirms the assumption of negligible contribution of metal films to the cross section of the samples to compute engineering stresses dividing the total force by the substrate cross-section only (refer to section 3.4.1). The results can be found in Figure 5.5 showing the engineering stress-engineering strain relation for each of the four kinds of specimens. The engineering definition was adopted because measurements of the deformed cross section were not provided for. Furthermore, the engineering definition complies with ASTMD882 for the determination of tensile properties of plastic thin sheeting, which then applies to the PI samples considered

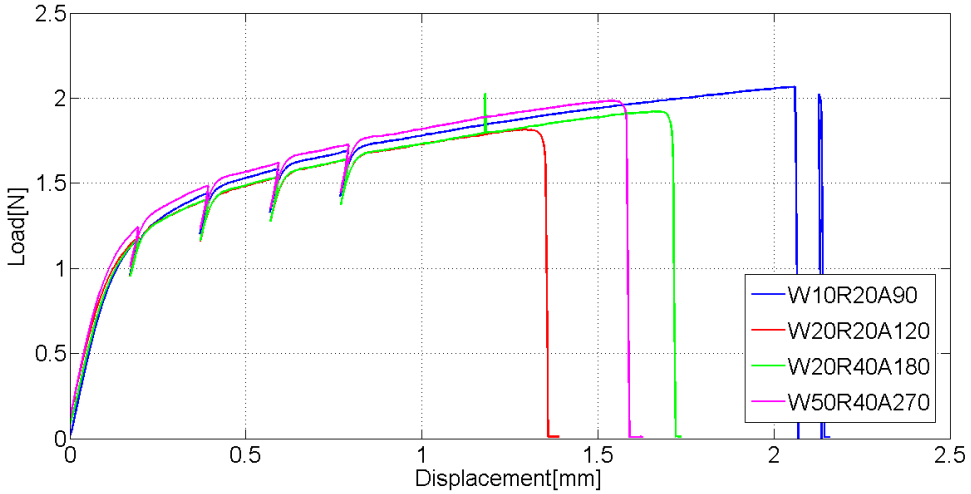

Figure 5.4: The load displacement relation for different specimens of the serpentine interconnects

in this study, provided the observation of their typical elasto-plastic behavior.

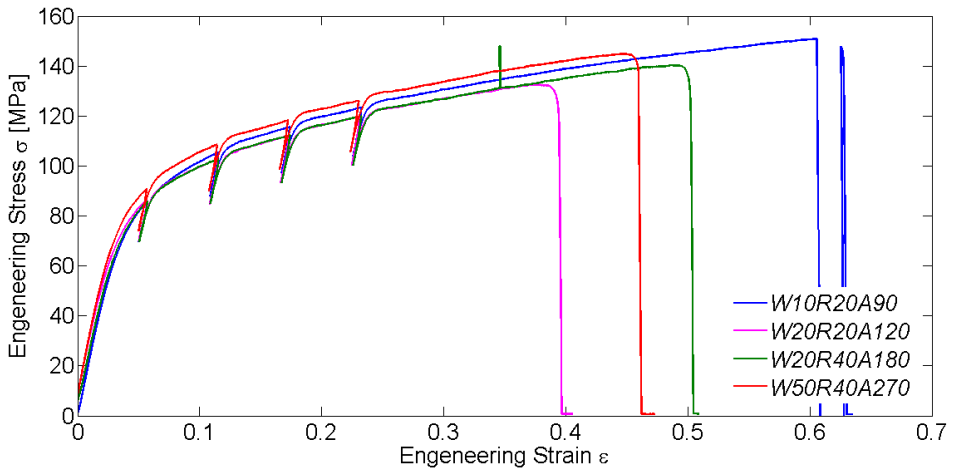

Figure 5.5: The engineering stress-engineering strain relation for different specimens of the serpentine interconnects

As it can be seen in the Figure 5.5, also the stress strain behavior of the different specimens are very close, making it possible to neglect the effect of the metallic interconnect with respect to the polymeric substrate in the global behavior of the whole

stretchable interconnect. On the other hand, it is noticeable that the stretchability of each specimen is between 40 and 60 percent. Such a stretchability is limited with respect to that of elastomeric substrates but still applies to applications requiring limited stretchability (Hattori et al., 2014). As was mentioned in section 3.4.1 the tests were observed by optical microscope and images have been captured during each tests with an interval of $20s$. Some examples of these images can be found in Figure 5.6. The *in-situ* optical imaging resulting in these images, provided an appreciable view of the very difference in the local mechanics of the interconnects with varying geometry, which conversely couldn't have been pursued by the overall stress/strain response only. The upper and lower case of transversal length among the specimens are presented in this figure. Figure 5.6(a) and (c) show the initial image taken before starting the test while images of in Figure 5.6(b) and (d) show the final image taken before the global breakage of the specimens. The buckling is easily observable in specimen W50R40A270 which has the $90\mu m$ long transversal part while in these images no buckling can be detected on the other specimen i.e. W10R20A90, which is the lowest case of transversal part of $30\mu m$ length. However, it was needed to study the phenomenon with more clear and precise images obtained from the ESEM.

In Figure 5.7 ESEM images of all the four types of specimens tested before the test and at the end of the loading are illustrated. The images are all with 400X magnification. Though more details can be found in the images found in Figures 5.8 to 5.11. From the images found in Figures 5.8 to 5.11 interesting results can be concluded. In the three later cases i.e. the specimens with the transversal part lengths of $40\mu m$, $60\mu m$ and $90\mu m$ the buckling and delamination of the thin film on the both sides of the transversal part are visible while in the first one representing the $30\mu m$ long transversal part specimen no buckling can be observed. In this case a uniform shear dominated delamination is seen but no buckling is observed: this results is extremely important, since it suggests the existence of a characteristic length in the buckling phenomenon.

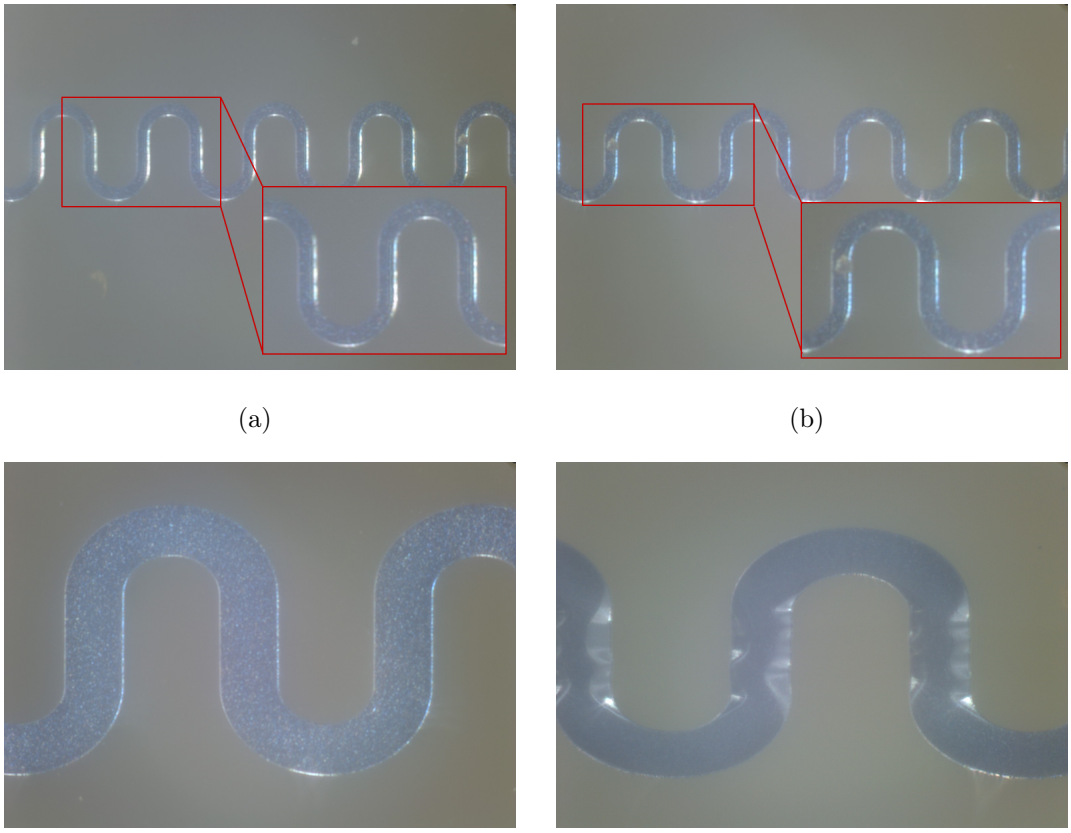

(a) (b)

(c) (d)

Figure 5.6: Optical microscope images of serpentine specimens; (a) W10R20A90 serpentine specimen before loading, (b) W10R20A90 serpentine specimen at the end of loading, (c) W50R40A270 serpentine specimen before loading, (d) W50R40A270 serpentine specimen at the end of loading

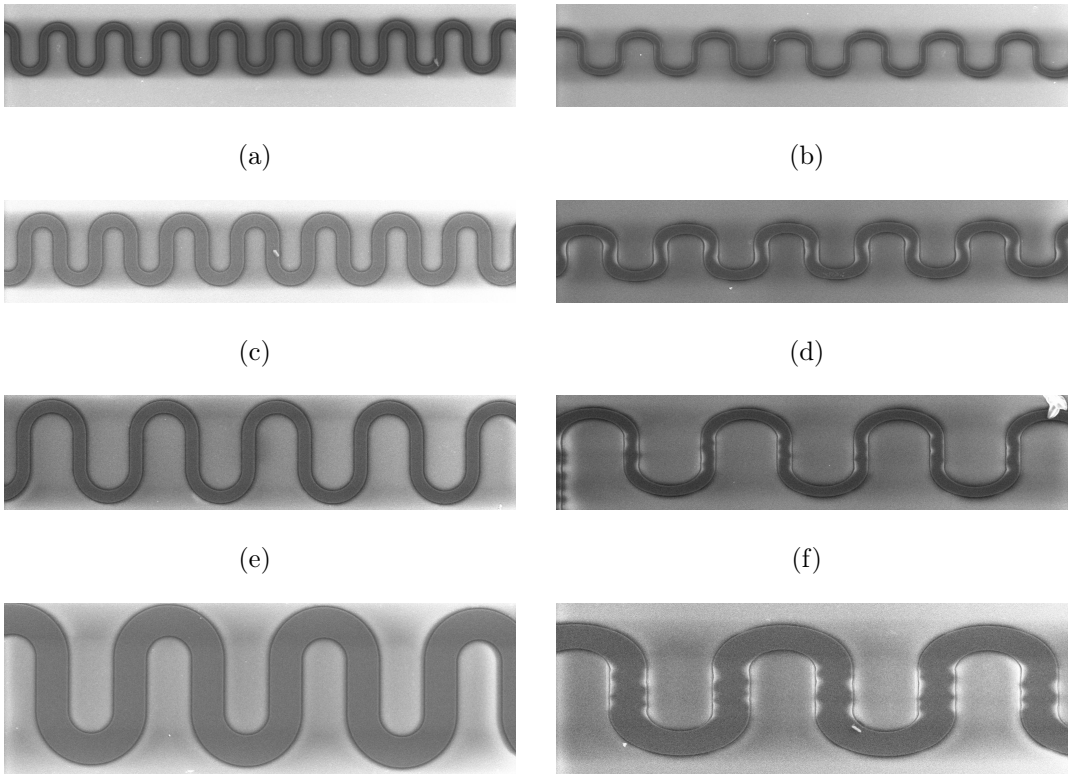

Figure 5.7: Environmental Scanning Electron Microscope (ESEM) images of serpentine specimens at 400X magnification; (a) W10R20A90 serpentine specimen before loading, (b) W10R20A90 serpentine specimen at the end of loading, (c) W20R20A120 serpentine specimen before loading, (d) W20R20A120 serpentine specimen at the end of loading, (e) W20R40A180 serpentine specimen before loading, (f) W20R40A180 serpentine specimen at the end of loading, (g) W50R40A270 serpentine specimen before loading, (h) W50R40A270 serpentine specimen at the end of loading

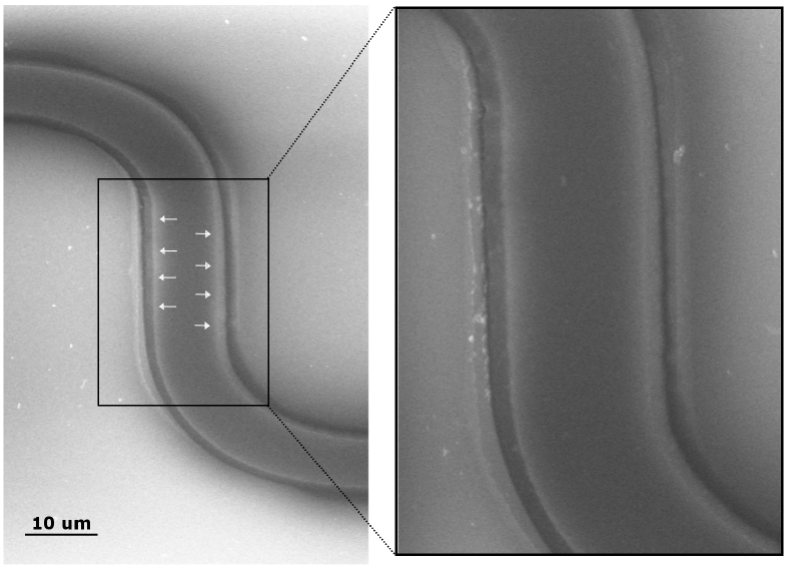

Figure 5.8: ESEM image of the W10R20A90 specimen with 400X and 2000X magnification at 35% stretch (for specimen geometrical information refer to Table 3.1)

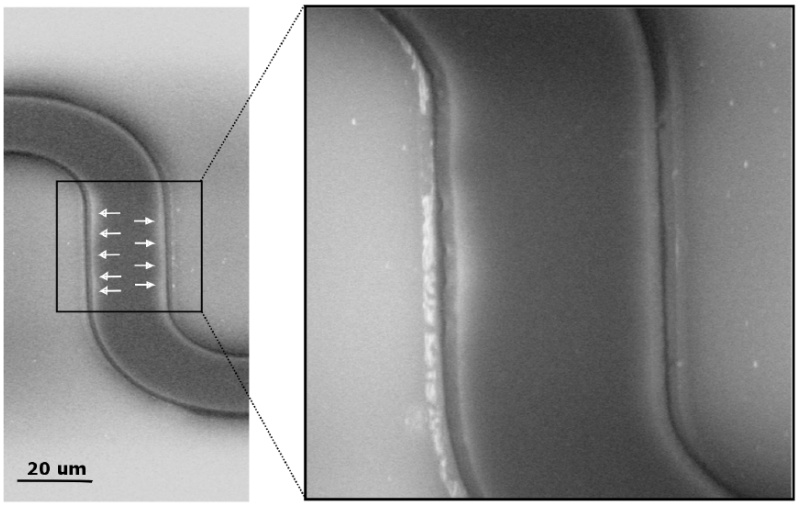

Figure 5.9: ESEM image of the W20R20A120 specimen with 400X and 2000X magnification at 35% stretch (for specimen geometrical information refer to Table 3.1)

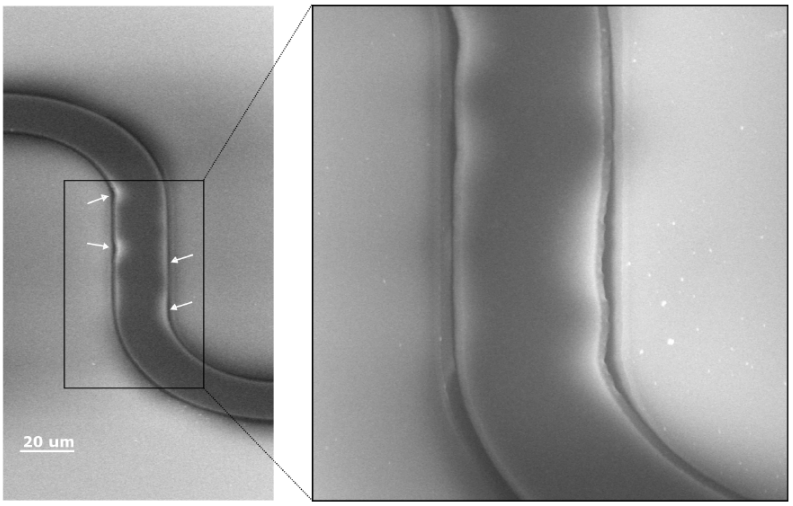

Figure 5.10: ESEM image of the W20R40A180 specimen with 400X and 2000X magnification at 35% stretch (for specimen geometrical information refer to Table 3.1)

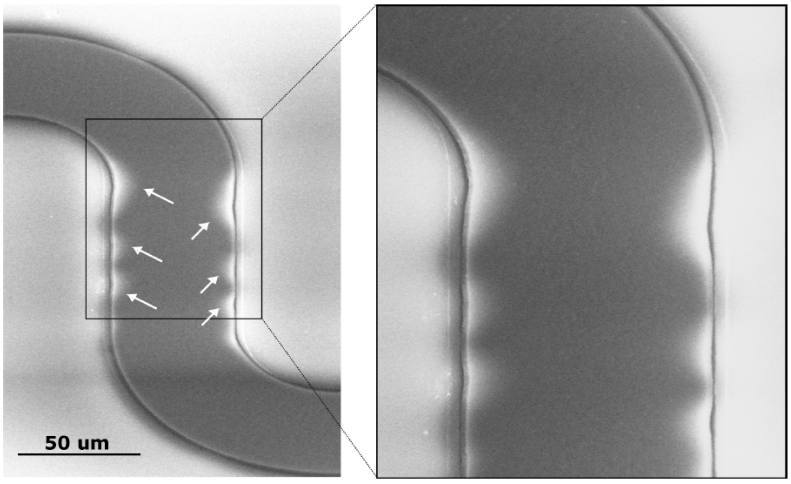

Figure 5.11: ESEM image of the W50R40A270 specimen with 400X and 2000X magnification at 35% stretch (for specimen geometrical information refer to Table 3.1)

5.2.3 Meander Buckling

The focus of the experimental tests performed to study the meander buckling was only on the local phenomena happening, so the stress strain curves obtained from the tests are skipped in reporting of the results and the images obtained by the optical microscope and ESEM will be reported only.

In Figure 5.12 images taken by the optical microscope during the experiments are seen. The images are captured before loading the specimens (Figures 5.12(a) and (c)) and after the complete unloading of the specimens to zero force (Figures 5.12(b) and (d)). The buckling observed in the transversal part (the part between two meanders in the case of W50R40A180 specimen which lacks the transversal part) suggests that the loading was done up to a point that can guarantee noticeable amount of plasticity inside the meanders. However enough plasticity was believed to be induced in the meanders, there was no buckling observed in the meanders in neither cases. A more clear image obtained from the ESEM can bee seen in Figure 5.13. This images shows a stretched and then unloaded W50R40A270 specimen with a 2000X magnification. No buckling was observed even with the precision of an ESEM image.

5.3 Analytical Models Results

In this section the results of the different analytical models introduced in chapter 4 will be discussed. As in chapter 4, the results will be presented as divided into different sections. The first two parts will be discussing the problem of transversal buckling, encompassing both the perfect bond analytical model and the imperfect bond one. In continue, the results obtained from the analytical model to study the meander buckling will be discussed again in two parts. Firstly, considering the substrate to be elastic and for two sets of material system; Secondly, with a elastic-plastic substrate based on the plasticity of PI as remarked in section 5.2.1.

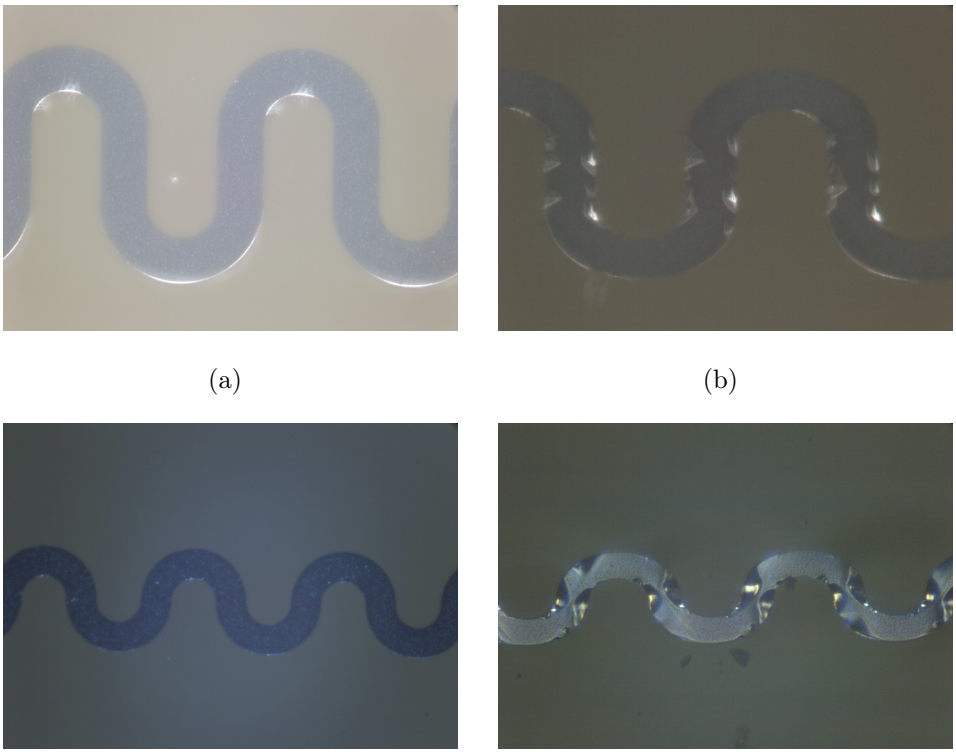

(a) (b)

(c) (d)

Figure 5.12: Optical microscope images of serpentine specimens used for the meander buckling tests; (a) W10R20A90 serpentine specimen before loading, (b) W10R20A90 serpentine specimen at the end of unloading, (c) W50R40A270 serpentine specimen before loading, (d) W50R40A270 serpentine specimen at the end of unloading

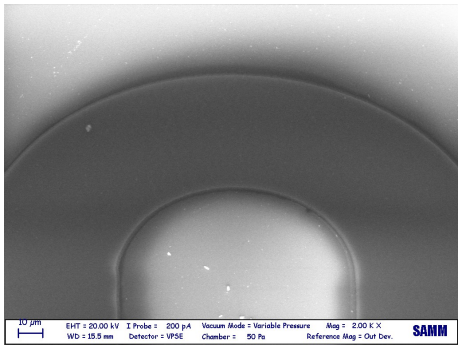

Figure 5.13: ESEM image of the W50R40A270 specimen with 2000X magnification after being stretched and then unloaded to load zero

5.3.1 Transversal Buckling - Perfect Bond Model

To study the transversal buckling the analogy with the problem by Song et al. (2008) was used. In order to make sure about the validity of the solution derived, the results were firstly found for the material system and geometry reported in the paper by Song et al. (2008) which are $E_f = 130GPa, \nu_f = 0.27, E_s = 1.8MPa, \nu_s = 0.48$ and $h = 0.1\mu m$ (silicon thin film and PDMS substrate). The results concerning this case are found in Figure 5.14. Good agreement between the results obtained from the present study and the reported results of Song et al. (2008) confirmed the reliability of the derivations done. In this figure both analytical and experimental results reported by Song et al. can be found.

In Figure 5.15 and 5.16 the results obtained from the application of the analogous problem of Song on the transversal buckling problem are reported. In Figures 5.15(a) and (b) the wavelength and amplitude of the buckling are plotted against the compressive transversal strain, respectively. Considering the Poisson's ratio effect, the same plots were found against the tensile axial strain. Considering the simplifications assumed in defining the model, this axial strain could be considered as the stretch applied to the entire stretchable interconnect. As a result, the wavelength and amplitude of the buckling against the axial tensile strain are plotted in Figure 5.16(a) and (b), respectively. The axial strain is more strictly related to the application since it roughly corresponds to the strain experienced by a hypothetical device featuring this kind of stretchable interconnects.

Specifically, in Figure 5.16(a) the onset of buckling is understood as the wave amplitude experiences an abrupt increase. This was expected for a mechanical phenomenon whose essential nature is that of an equilibrium instability. The buckling critical strain is shown on the plots for the wavelength as well, using a star indicator. The critical compressive strain resulting in buckling of the thin film was found to be equal to 0.08 and the corresponding axial tensile strain which initiates the buckling in the transversal parts was found to be equal to 0.2353. Finally, the wavelength cor-

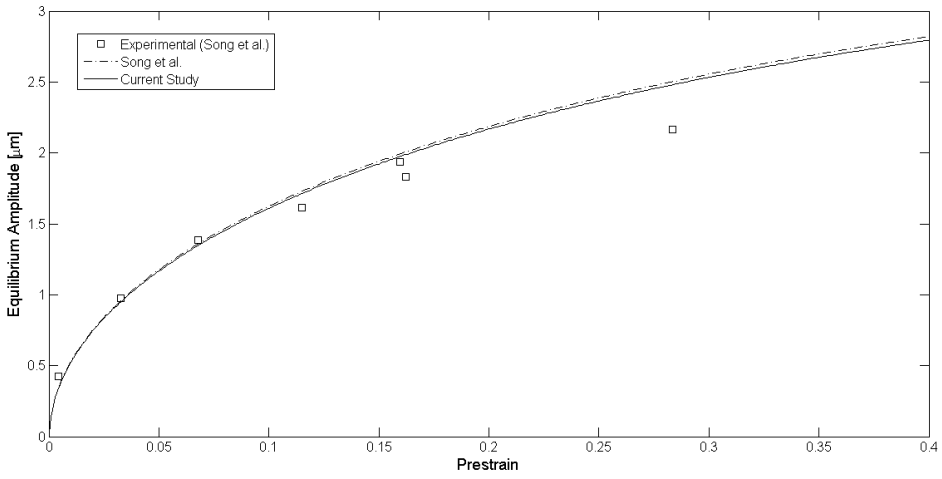

(a)

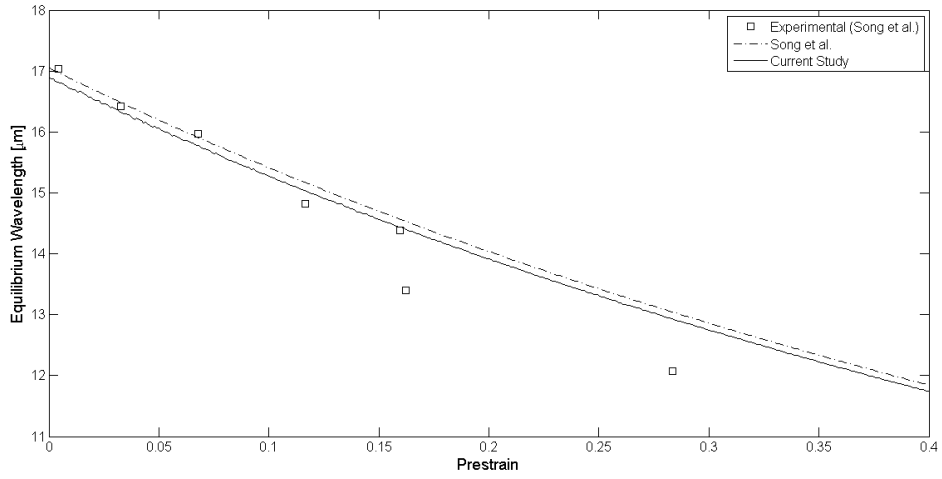

(b)

Figure 5.14: The results of the analogous problem used to solve the transversal buckling problem to be compared with the results by Song et al. (2008); (a) amplitude of buckling with against the prestrain, (b) wavelength of buckling with against the prestrain

responding to the onset of buckling was resulted to be $10.7\mu m$. Reliability of these results will be discussed in Chapter 6, as compared to experimental observations and validated computational results.

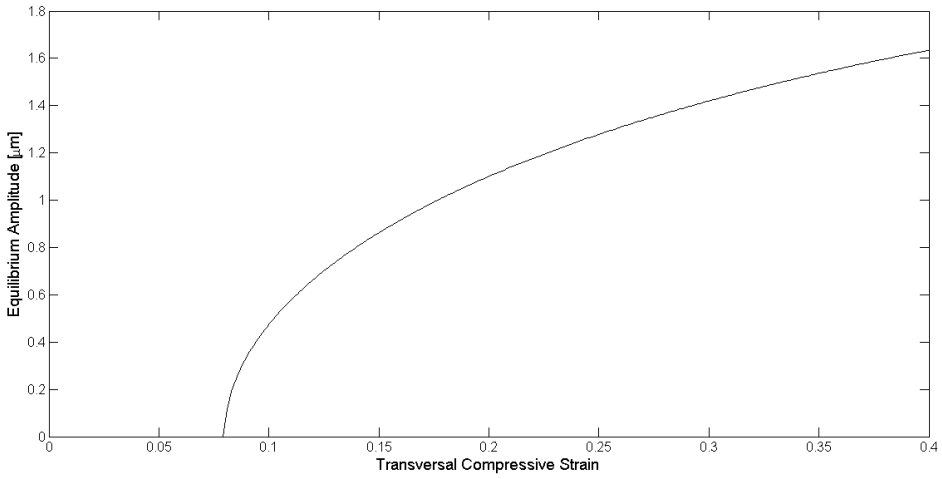

(a)

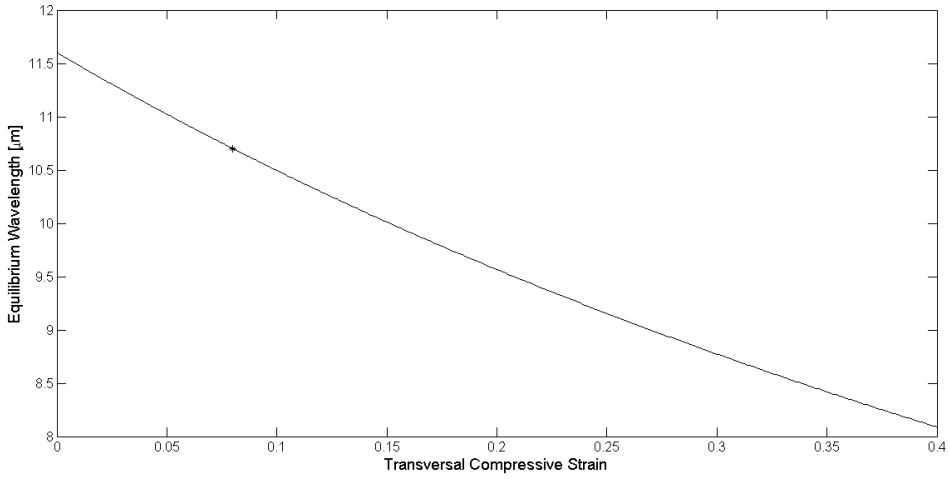

(b)

Figure 5.15: The results of the transversal buckling problem; (a) amplitude of buckling with against the transversal compressive strain, (b) wavelength of buckling with against the transversal compressive strain

5.3.2 Transversal Buckling - Imperfect Bond Model

While the perfect bonded interface model provided a suitable description of the post-buckling behavior, the imperfect bond model can only provide an estimate of

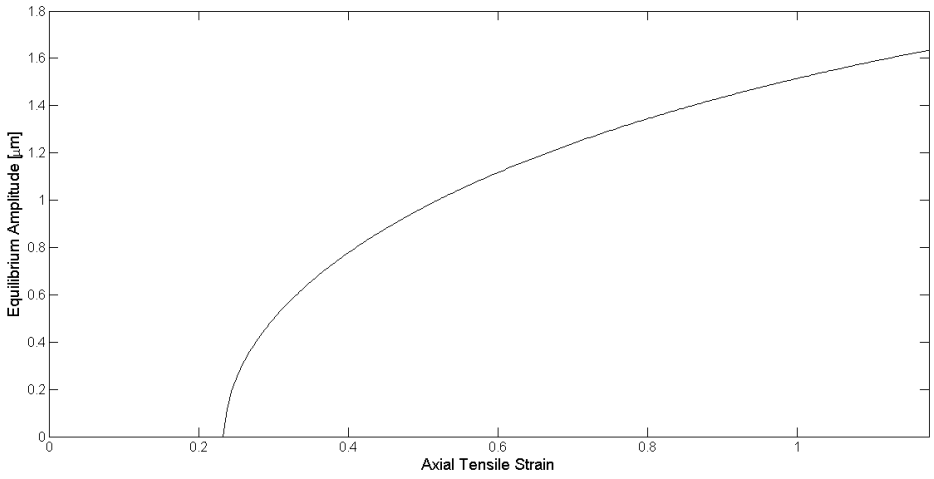

(a)

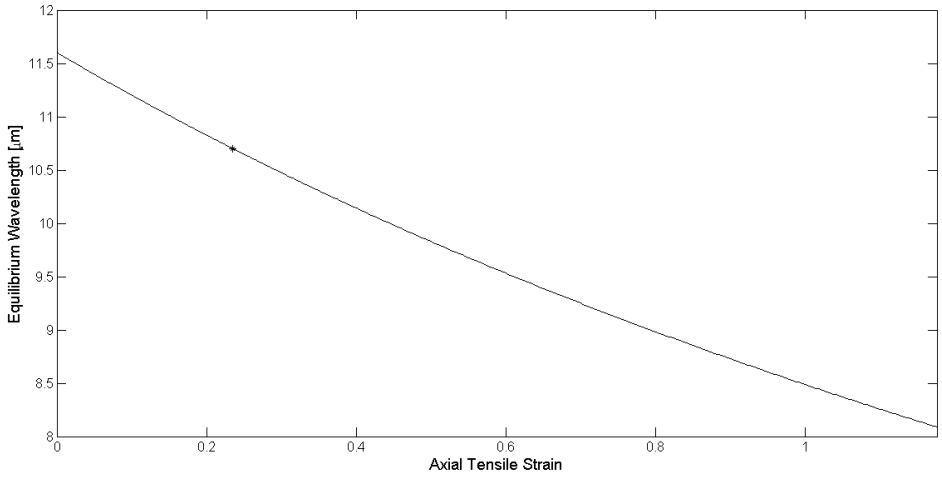

(b)

Figure 5.16: The results of the transversal buckling problem; (a) amplitude of buckling with against the axial tensile strain, (b) wavelength of buckling with against the axial tensile strain

the critical point. Nevertheless, this perfectly complies with the need to estimate the safe deformation range, in which buckling is not likely to occur. Provided this remark on such fundamental difference between the two analytical models presented for the buckling of transversal parts, the results of the imperfect bond model are

reported here as in Figure 5.17 plotting the critical transversal compressive strain versus λ, which is a dimensionless representative of the buckling wave length. As it was noted in section 4.2, the experimental value for the interface stiffness can be presented with two values (a pair of upper and lower bounds). In this figure, the relation between the critical strain and λ is plotted for these two values of interfacial stiffness. It should be noted that the minimum of the plot reveals the condition of buckling both in terms of the critical strain and the wavelength. The results state that the buckling should occur at the transversal strain between 0.37% and 0.59% and the wavelength of buckling should be in range of $33.4\mu m$ and $42\mu m$.

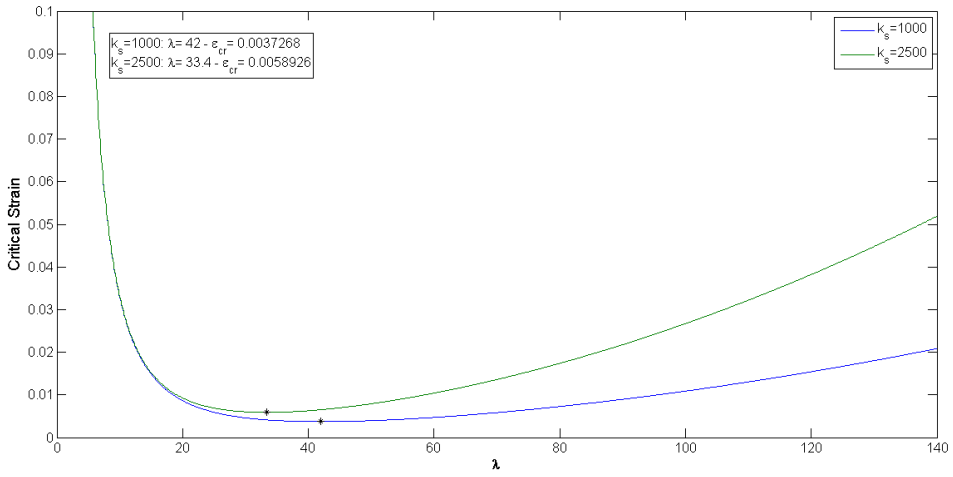

Figure 5.17: The results of the transversal buckling problem with the imperfect interface for the experimental value of the interfacial stiffness ($K_s = 1000 - 2500 MPa/mm$)

The same analysis was repeated by changing the values of interfacial stiffness. The values of 10 times bigger, 10 and 100 times smaller than the experimental value of K_s were explored and the results can be found in Figure 5.18. It was observed that the wavelength increases with decreasing of the interfacial stiffness and the buckling happens in lower strain.

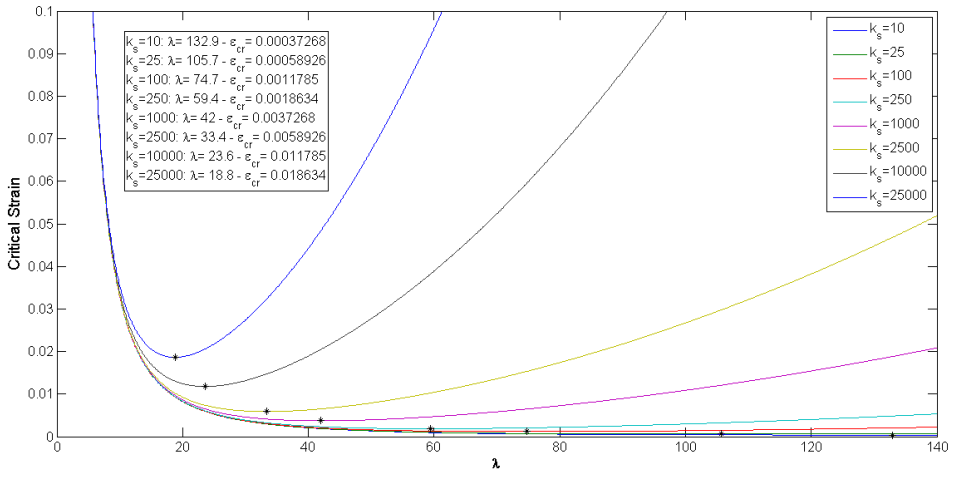

Figure 5.18: The results of the transversal buckling problem with the imperfect interface for different values of the interfacial stiffness

5.3.3 Meander Buckling on Elastic Substrate

The results of the meander buckling problem obtained form the model described in section 4.3 are represented here for the case of elastic substrate. The material properties and the geometry corresponding to the specimens used in the tests are studied firstly and then another case of material properties were applied to the model to study a different case as well.

The results of the material system of Aluminum thin film and PI substrate can be found in Figures 5.19(a) and (b), plotting the amplitude and wavelength of the buckling respectively. It is noteworthy to recall that the model of perfect bond for transversal parts and that of buckling of meanders during unloading essentially branch from the very same model by Song et al.: thus, it is not surprising that the critical strain and the corresponding wavelength coincide in the two cases, for the amounts of 8% strain and 10.7 μm, respectively. The only significant difference resides in how the so called prestrain is understood and thus how does it relate with the overall sample stretch, which is the very application parameter. While for the perfect bond model for transversal parts, the strain leading to buckling was

the compressive strain due to Poisson effect, in the model of meander buckling the plastic strain trapped in the meander stands for Song's prestrain: based on previous simulation results (Cattarinuzzi, 2012), by first approximation it could be argued that the first principal strain experienced by the meanders is equal to the overall sample strain in the stretch direction; thus the critical strain applied to the whole interconnect is the total strain corresponding to 8% of plastic strain due to Al hardening law.

Considering another material system of gold thin film on a Polydimethylsiloxane (PDMS) substrate, the results of the meander buckling were found and are plotted in Figures 5.20(a) and (b), representing the amplitude and wavelength of buckling respectively. It can be seen that the buckling happens in very lower value of plastic strain (almost zero) and the wavelengths are very longer with respect to the Al/PI system which is due to the lower stiffness of the substrate lowering the energy of the equilibrium state.

Experimental evidence was found in the literature in a similar case, i.e. meander buckling due to compressive strain in Au/PDMS material system (Gray et al., 2004).

5.3.4 Meander Buckling on Elastic-Plastic Substrate

Based on the irreversibility of the PI substrate, the results of the previous section on the meander buckling of Al/PI system cannot be trusted, since they do not account for the plasticity of the substrate. (see the arguments of section 4.3).The results of the meander buckling model, enriched by the plasticity of the substrate are reported in Figure 5.21 where in part (a) the amplitude of buckling for the two cases of elastic and plastic substrate are compared. The fact that the amplitude for the plastic substrate remain zero suggests that the buckling doesn't occur in this case or at least it doesn't show it self in up to 25% of thin film plastic strain which is plotted here. The reason, based on the argument depicted in Figures 4.10 and 4.11, can be found in Figure 5.21(b). This figure illustrates the plastic strain

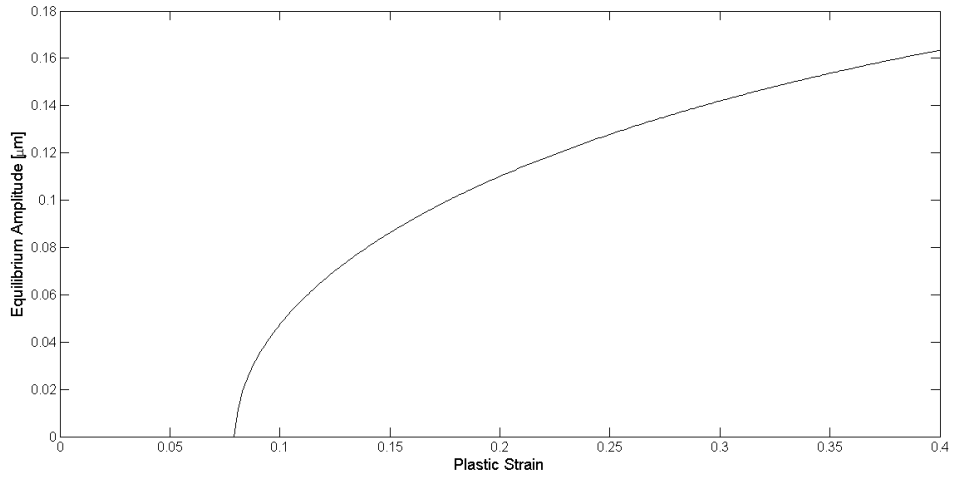

(a)

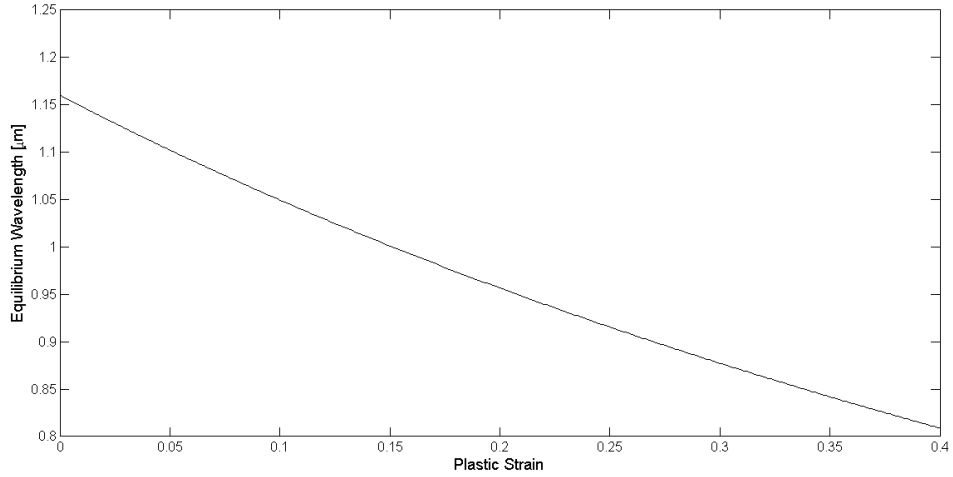

(b)

Figure 5.19: The results of the meander buckling problem for the Al/PI material system; (a) amplitude of buckling with against the plastic strain in the thin metal film, (b) wavelength of buckling with against the plastic strain in the thin metal film

offset (the parameter to be checked with the buckling criteria) for both elastic and plastic substrate. It can be noticed that in the elastic substrate case, the offset (being equal to the plastic strain of the thin film only) intersects with the buckling limit at the strain equal to 0.08, while in the case of plastic substrate the plastic

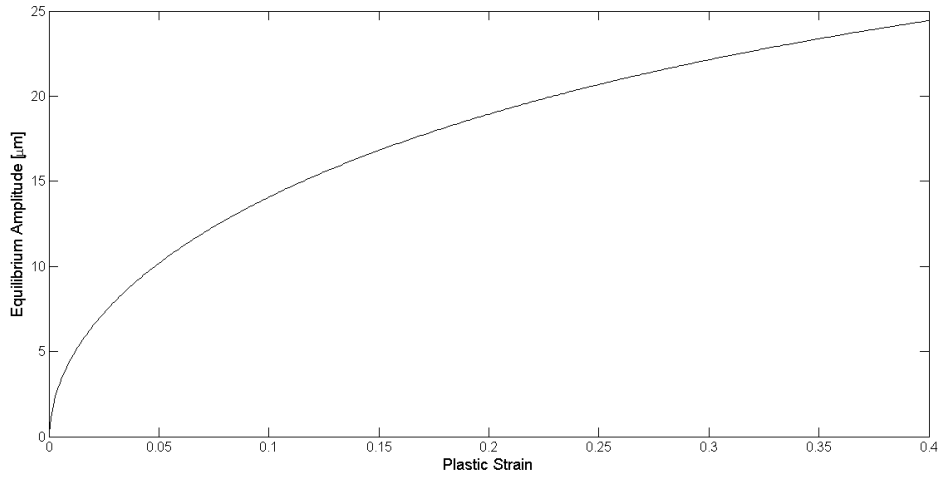

(a)

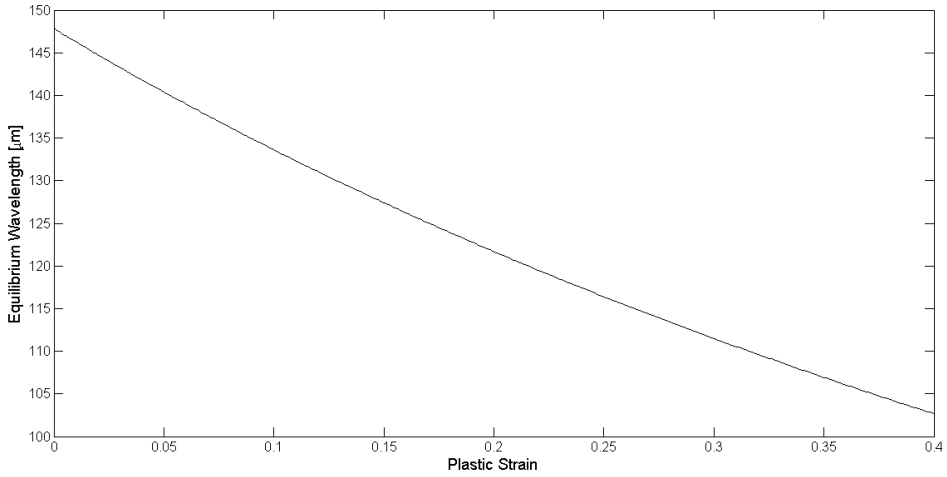

(b)

Figure 5.20: The results of the meander buckling problem for the Au/PDMS material system; (a) amplitude of buckling with against the plastic strain in the thin metal film, (b) wavelength of buckling with against the plastic strain in the thin metal film

strain offset doesn't reach the limit up to the 25% of metal thin film plastic strain seen in the plot. So it is reasonable no to observe buckling in Figure 5.21(a). If the trend of the curve representing the plastic substrate is considered constant out of the range shown, the buckling criterion will be satisfied only in a very high value of

strain before which the global failure of the interconnect happens, which based on the experimental results is in the range of 40% to 60% (refer to Figure 5.5).

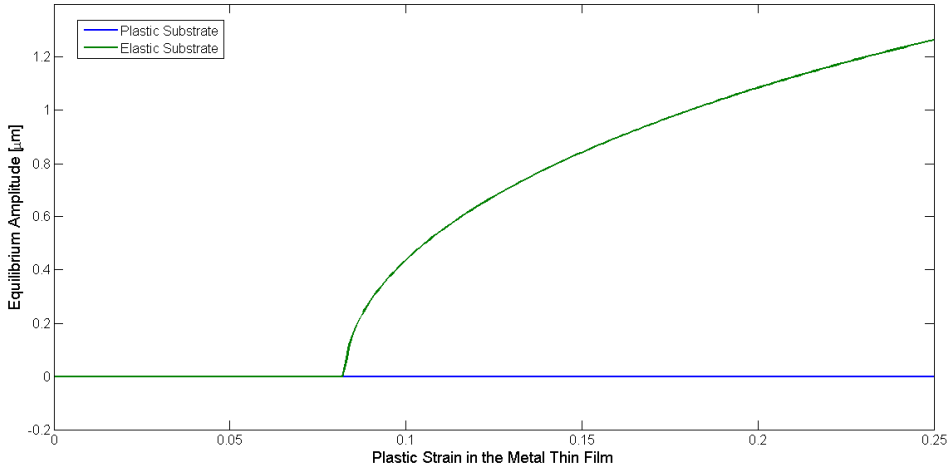

(a)

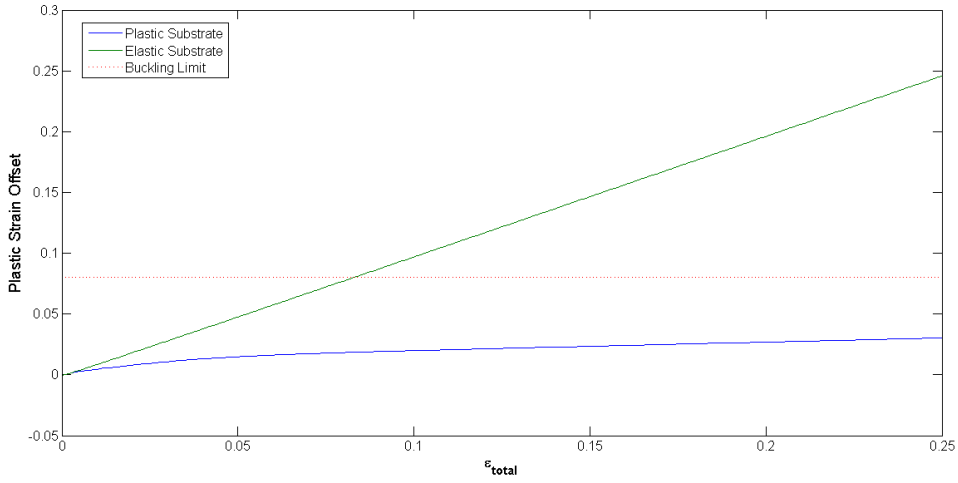

(b)

Figure 5.21: The results of the meander buckling problem for the Al/PI material system considering the substrate as an elastic plastic; (a) amplitude of buckling with against the plastic strain in the thin metal film, (b) wavelength of buckling with against the plastic strain in the thin metal film

5.4 Finite Element Model Results

In the finite element model of Abaqus, two parameters where changed to be studied. The transversal part length was a design parameter of major concern, since it was known for each sample and thus its effect on the buckling behavior could be directly compared with the corresponding experimental results. The interfacial stiffness was the second parameter in the view of further investigation of its influence on the buckling behavior to make possible also the comparison with the results of the analytical model. The interfacial stiffness was modeled by three other values in addition to the experimental value (refer to section 4.4). In figure 5.22 the contours illustrating the vertical displacement field in each case of interfacial stiffness can be found. All the cases are modeled with a $90\mu m$ length. It is seen that the higher the stiffness, the lower the wavelength and consequently the higher number of waves are fitted in the 90 micrometers of length, allowing the buckling and delamination. In Figure 5.23, the contours showing the axial stress in the model are found for each case of interfacial stiffness. The distribution of the axial stress in the thickness of the thin film shows the development of bending due to the deformation caused by buckling. It is interesting to notice that in the lower cases of the interfacial stiffness, this distribution is very close to a symmetric distribution, while with higher values of interfacial stiffness notable asymmetry is observed such that no tension at all is observed through the film-thickness for the highest value of interfacial stiffness. This can be only explained by the compressive stress inside the thin film due to the direct external loading. Considering this fact this reveals that the amount of compressive stress is higher in the stiffer interface models suggesting that the buckling happens in a higher amount of applied strain. This is will be confirmed quantitatively in continue, observing evolution of the vertical deformation by the applied strain in each model.

In figure 5.24 the vertical displacement of a single node in the model of $90\mu m$ length is plotted against the applied compressive strain. The critical strain was

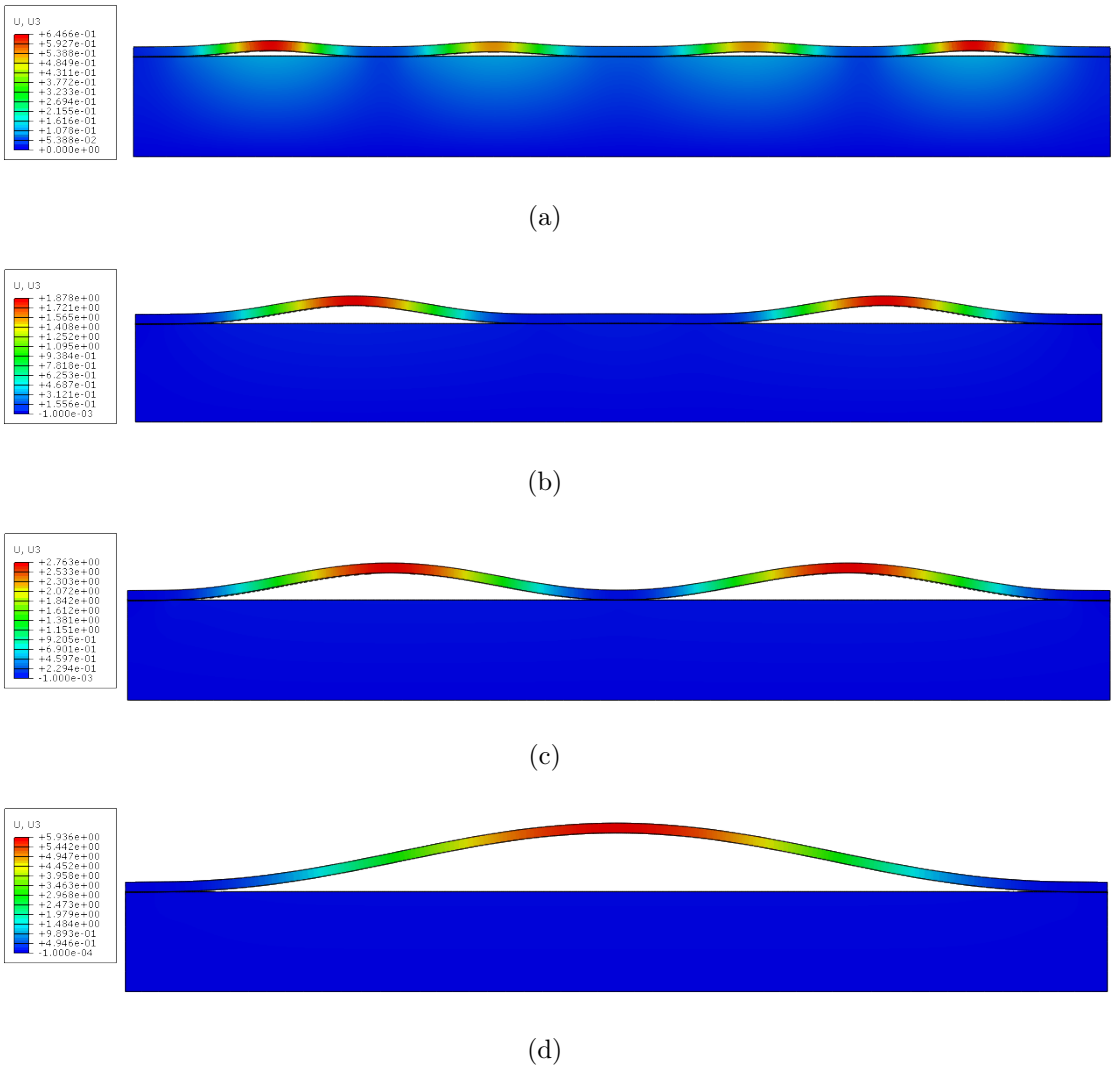

Figure 5.22: Contours of vertical displacement for the different cases of interfacial stiffness (a zoomed section of the model showing one wave length of buckling) ; (a) the highest value of interfacial stiffness ($K_s = 10000 - 25000 MPa/mm$), (b) the experimental value of the interfacial stiffness ($K_s = 1000 - 2500 MPa/mm$), (c) a lower value of interfacial stiffness ($K_s = 100 - 250 MPa/mm$), (d) the lowest value of interfacial stiffness ($K_s = 10 - 25 MPa/mm$)

trivially defined as the point in which an abrupt shift in the slop of the node displacement was observed. Automatic identification of the exact value for the critical strain was pursued by the development of a proper MATLAB (MathWorks, Inc.,

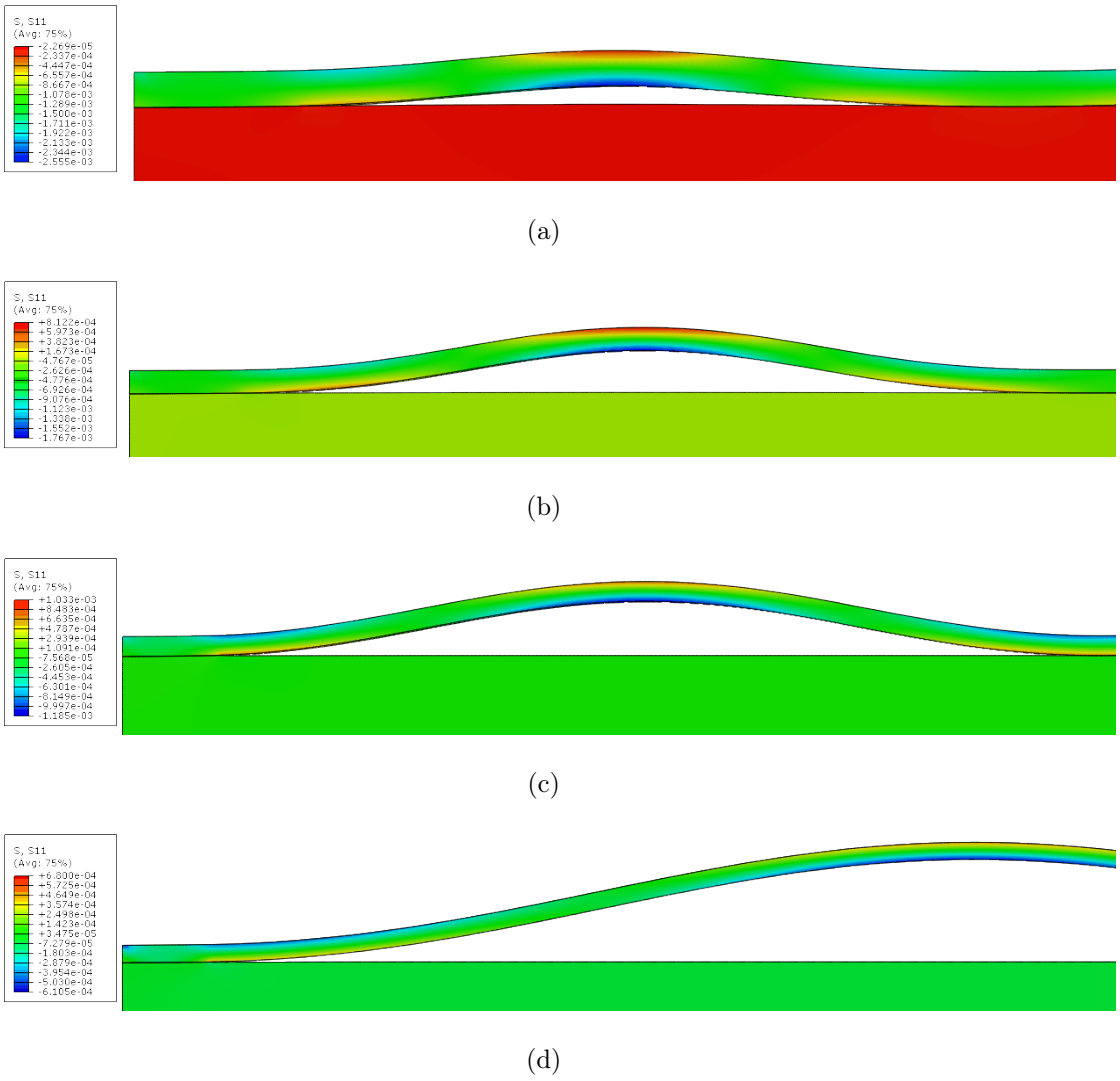

Figure 5.23: Contours of axial stress for the different cases of interfacial stiffness; (a) the highest value of interfacial stiffness (10 times bigger than the experimental value), (b) the experimental value of the interfacial stiffness, (c) a lower value of interfacial stiffness (10 times smaller than the experimental value), (d) the lowest value of interfacial stiffness (100 times smaller than the experimental value)

Massachusetts, USA) routine; this protocol was systematically applied to each modeling case study.

Figure 5.25 shows all the four cases of interfacial stiffness in the plot of vertical displacement against the length of the model. The simulation results are quantita-

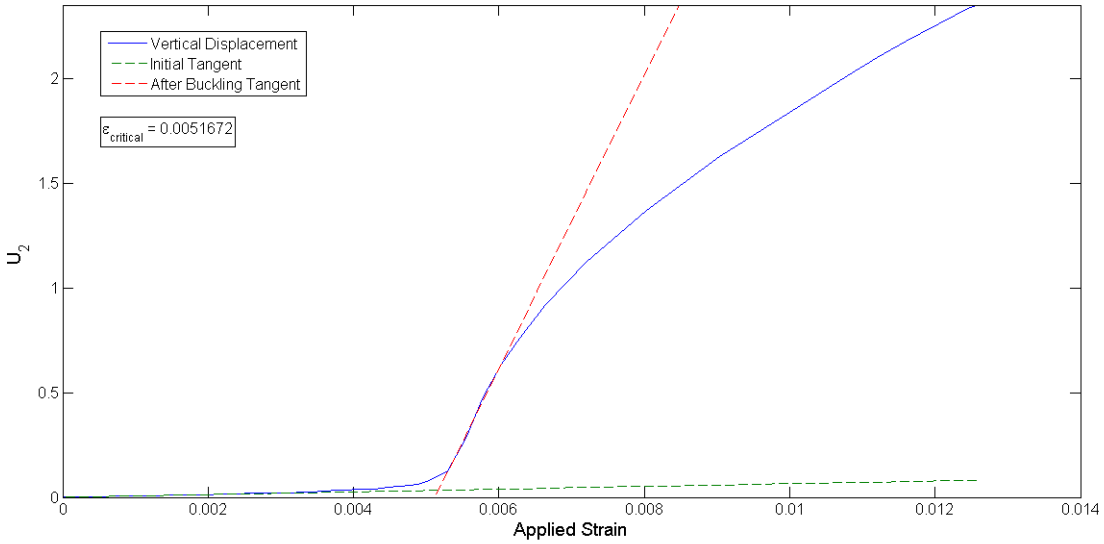

Figure 5.24: The vertical displacement of a single node of the thin film plotted against the applied compressive strain on the model of $90\mu m$ length and experimental interfacial stiffness showing the method used to find the critical strain

tively compared in terms of wavelength amplitude and critical strain. The change in the wavelength of the buckling is basically due to the change of the equilibrium energy state. The higher the interfacial interface, the higher the energy content of the system under compression which results in lower wavelengths and higher buckling critical strains.

In continue, using the interface stiffness as its experimental value, the simulation was done for different lengths, representing different cases of transversal lengths as in the S shaped interconnect specimens. In Figure 5.26 the vertical displacement contour for every five different lengths can be found.

Table 5.1: The wavelength and critical strain for different cases of transversal length in the finite element model

L=40 [μm]		L=60 [μm]		L=90 [μm]		L=100 [μm]	
Wavelength [μm]	ε_{cr}	Wavelength [μm]	ε_{cr}	Wavelength [μm]	ε_{cr}	Wavelength [μm]	ε_{cr}
38.3	0.00546	31.7	0.00567	36.7	0.00517	36.0	0.00525

Figure 5.27 better depicts the effect of transversal length on the buckling of

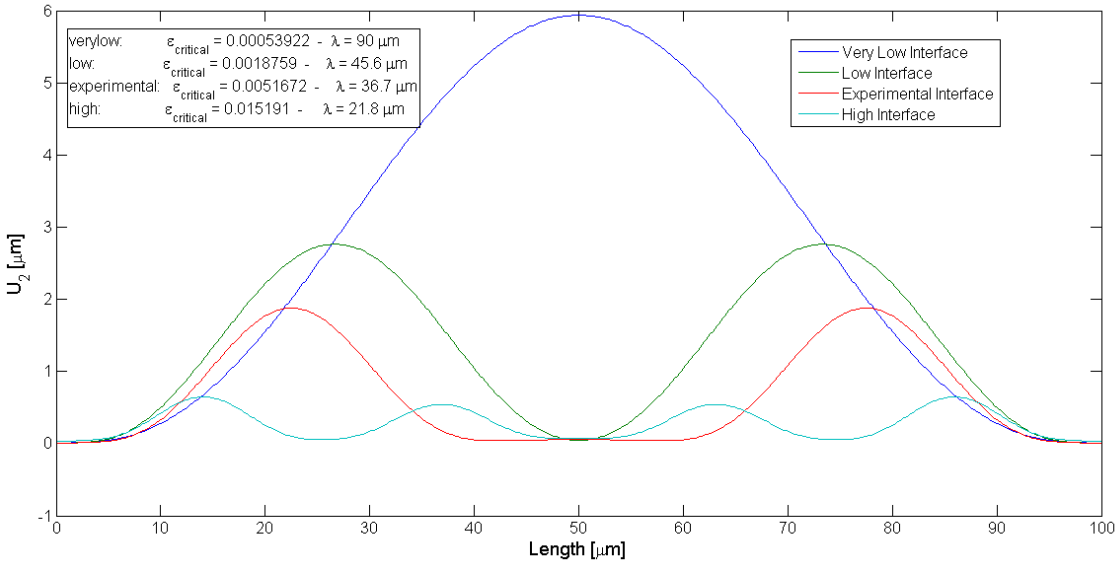

Figure 5.25: The vertical displacement of the thin metal film against the length of the model for different cases of interfacial stiffness

the thin film. It is seen that the model with only $30\mu m$ length doesn't allow the buckling, while the others do. The model of $40\mu m$ length allows only one wavelength of buckling while the models of $60\mu m$ an $90\mu m$ allow two of them and the longest case of $100\mu m$ fits almost three. This is accompanied with the fact that the wavelength remains in the range of $31.7\mu m$ and $38.3\mu m$ and the critical strain in the range of 0.52% and 0.57%. The wavelength and critical strain for different cases of transversal part length can be found in Table 5.1.

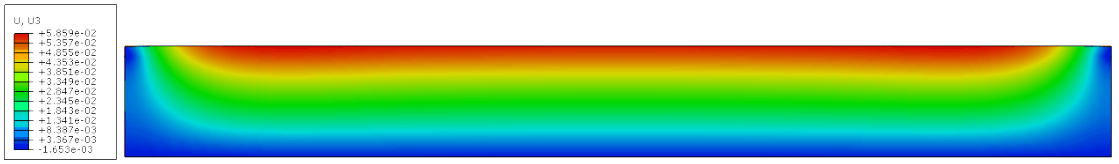

(a)

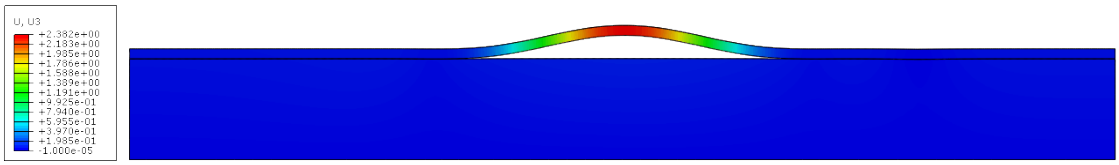

(b)

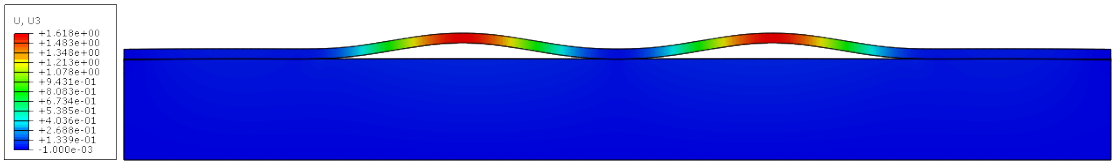

(c)

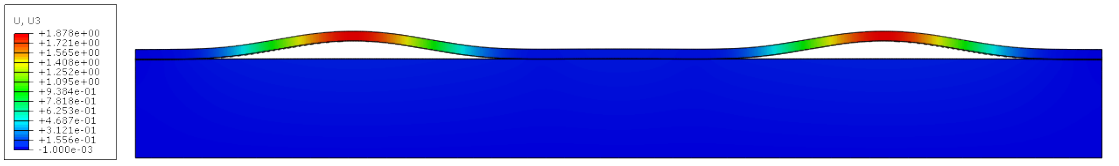

(d)

(e)

Figure 5.26: Contours of vertical displacement for the different cases of interfacial stiffness; (a) $30\mu m$ long transversal part, (b) $40\mu m$ long, (c) $60\mu m$ long, (d) $90\mu m$ long, (e) $100\mu m$ long

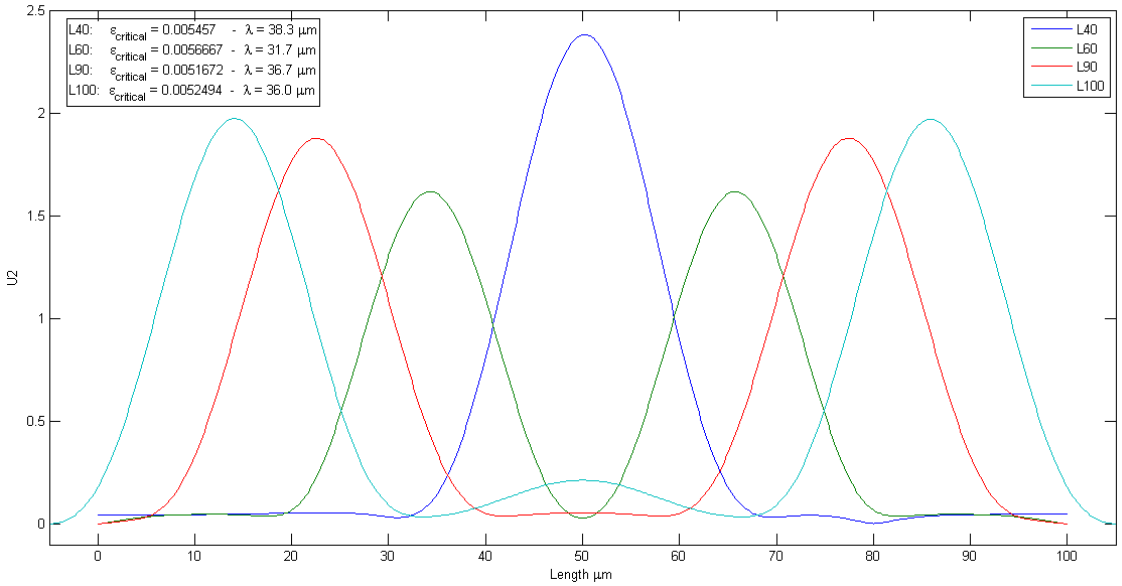

Figure 5.27: The vertical displacement of the thin metal film against the length of the model for different cases of transversal part length

Chapter 6

Conclusions

6.1 General Conclusions

A combination of experimental analytical and numerical tools enabled the investigation of the local behavior of stretchable interconnects consisting of Al thin film on PI substrates. New insights in the interplay between the buckling and delamination failure modes were presented in chapter 5. The in-house prepared test setup, allowed for reliable *in-situ* analysis, providing meaningful results for this study. Analytical models were developed, aiming to provide effective tools for the prediction of the buckling behavior (section 5.3). Validation of the latter by means of comparison with reliable computational models (section 5.4) suggests the current study to provide significant preliminary contribution in the view of mechanically reliable design of stretchable interconnects. In continue, relevant conclusions will be cast matching the information provided by all the investigation methods presented in this study. The experimental study of the mechanical properties of the S shaped interconnects used in stretchable electronics showed between 40% and 60% of stretchability in the material system of Al thin film and PI substrate, which places this type of interconnects as a suitable interconnect for disposable applications requiring limited stretchability. However this grade of stretchability was accompanied with some local

phenomena such as buckling of the thin metal film and its delamination from the substrate which can be accounted for as failure of the interconnect. In continue, analytical and computational approaches were used in order to study the buckling of the thin film in two main structural parts of the S shaped interconnects, namely meanders and transversal parts. In this way there was the possibility to compare the results of the models with the qualitative observations of the buckling and delamination obtained from the experiments.

The buckling of the transversal parts were studied through analytical model and a finite element simulation. Based on the fact that the buckling of the thin film, in the Al/PI samples was always observed being accompanied by the delamination it is important to account for the imperfection between the bonding of the thin metal film and the polymeric substrate. The analytical model considering the imperfection of the interface between the thin film and substrate however, reveals results that are in agreement with the observations of the experimental tests performed to study the buckling of the transversal parts of the interconnects. This analytical model suggests that the buckling in the transversal part occurs at the strain between 0.37 % and 0.59 % and the wavelength of buckling will be in range of $33.4\mu m$ and $42\mu m$. This wavelength range is suggesting a characteristic length which was observed in the experimental results as well while the perfect-bond model was unable to quantitatively match with experiments. The specimens with transversal parts smaller than this range ($L = 30\mu m$) did not show any buckling in their transversal parts while in all the other specimens ($L = 40, 60 and 90\mu m$) the buckling occurred. It was concluded that different buckling/delamination behaviors observed for varying serpentine geometries were related to the ratio between the transversal part length and the characteristic length of the typical buckling wavelength. Specifically, delamination accompanied by buckling could occur provided that at least one entire wavelength could be hosted by the transversal length; otherwise, only uniform shear dominated delamination could be observed. There was also a very good agreement between these results and the ones obtained from the finite element simulation of

the transversal buckling phenomenon. The wavelength and critical strain found by the FE model for different cases of transversal length, as in Table 5.1, are all in the same range as found by the analytical model. Also the study on the interfacial stiffness effect ended in exact agreement for both the finite element model and the analytical one as can be found in Table 6.1. Only the wavelengths found for the two lower values of interfacial stiffness are out of the corresponding ranges, however they are very close. Since in this case the model was featuring a $90\mu m$ long transversal part, it could not host one and two wavelengths inside for the '*very low*' and '*low*' cases of interfacial stiffness, respectively, and satisfy the range stated by the analytical model. As a consequence the wavelengths were shrunk to fit in the available length but remained close to the values predicted by the analytical model. Based on this agreement, both with the experiments and the FEM, the analytical model can be used as a simple and useful tool to describe the buckling of the thin film in the transversal part of the S shaped interconnects of the stretchable electronics.

Table 6.1: Comparison between the Analytical model of transversal buckling (imperfectly bonded interface) and the finite element model

Analytical Model			Finite ESlement Model		
$K_s[MPa/mm]$	Wavelength $[\mu m]$	ε_{cr}	Wavelength $[\mu m]$	ε_{cr}	Interfacial Stiffness Case
10	132.9	0.00037	90.0	0.00054	Very Low
25	105.7	0.00059			
100	74.7	0.00118	45.6	0.00188	Low
250	59.4	0.00186			
1000	42.0	0.00373	36.7	0.00517	Experimental
2500	33.4	0.00589			
10000	23.6	0.01179	21.8	0.0152	High
25000	18.8	0.01863			

The analytical study of the buckling of the thin film in the meanders of the S shaped interconnects was performed in two cases for Al/PI material system: (i) as a preliminary attempt, plasticity of the PI substrate was neglected in the first model; (ii) conversely, the second model is a more refined one, accounting for the effect of PI permanent strain during unloading. Considering the plasticity of the substrate, the

buckling was predicted not to occur in the meanders, which was in agreement with the results obtained form the experimental study on the meander buckling; in fact the later haven't shown buckling after complete unloading of different specimens. On the other hand, the first model presenting the case of elastic substrate can be a useful tool to predict the buckling in the meanders of interconnects as far as elastomeric substrates are concerned, e.g. for the case of gold thin film and PDMS substrate. In this case buckling of the menders was predicted to happen with even small amount of plastic strain trapped inside the thin film and experimental evidences from the literature confirm the aforementioned issue for metal conductors on elastomers. It can be concluded that using an elastic-plastic substrate like PI can be useful since it prevents the buckling of the meanders in unloading and is suitable for disposable applications requiring limited stretchability, while a substrate without any plasticity such as an elastomer like PDMS, can be useful for cyclic applications having in mind that the buckling of the meanders is due in this case.

6.2 Future Developments

The current study consisted of experimental, analytical and numerical investigation of the buckling and delamination phenomenon in the stretchable interconnects. The work done can be extended in some suggested directions as follows. In preparation of the μTensile Machine, preparation of a force control testing system can make possible a new series of tests that would give the possibility to study new aspects of the mechanical behavior of the stretchable electronic interconnects. Recalling that the mechanical reliability is due, indeed, to ensure electrical reliability as well, performing electro-mechanical tests could be a further step. So far in this thesis, the failure of the interconnects was considered as the global breakage or local out of plane phenomena such as delamination of the thin film, however the *in-situ* measurement of the electrical resistance of the interconnects during the mechanical tests can provide useful information and better insight of the phenomena happening

in the interconnects.

As concerned material selection, alternative to the Al/PI interconnects would be Au/PDMS (as applied in one of the analytical models of the current study). Studying the mechanical behavior of samples made of this combination of materials with specific experimental focus is suggested as a future development to this thesis. The Au/PDMS interconnects is expected to show different mechanical behavior, due to the elastomeric nature of the polymeric substrate, which would on one hand enable higher stretchability (beyond 100% strain), while on the other hand is more likely to trigger meander buckling when recovering extremely large deformations; an experimental study on the buckling of the meanders upon unloading can help validating the results obtained form the analytical model of the meander buckling. Furthermore, to assess the reliability of the estimates by the meander buckling model, the development of finite element plain strain models accounting for metal film plasticity would be a natural continuation of the present study, as already provided for the transversal buckling case.

Bibliography

F. Axisa, F. Bossuyt, J. Missine, R. Verplancke, T. Vervust, and J. Vanfleteren. Stretchable engineering technologies for the development of advanced stretchable polymeric systems. In *PORTABLE-POLYTRONIC 2008 - 2nd IEEE International Interdisciplinary Conference on Portable Information Devices and the 2008 7th IEEE Conference on Polymers and Adhesives in Microelectronics and Photon*, 2008.

N. Bowden, S. Brittain, A.G. Evans, J.W. Hutchinson, and G.M. Whitesides. Spontaneous formation of ordered structures in thin films of metals supported on an elastomeric polymer. *Nature*, 393(6681):146–149, 1998.

L. Cai, J. Li, P. Luan, H. Dong, D. Zhao, Q. Zhang, X. Zhang, M. Tu, Q. Zeng, W. Zhou, and S. Xie. Highly transparent and conductive stretchable conductors based on hierarchical reticulate single-walled carbon nanotube architecture. *Advanced Functional Materials*, 22(24):5238–5244, 2012.

E. Cattarinuzzi. Meccanica dei dispositivi di "stretchable electronics": Caratterizzazione dei materiali costituenti e comportamento meccanico delle interconnessioni. Master's thesis, School of Industrial Engineering, Bioengineering Department, Politecnico di Milano, 2012.

W.-Y. Chang, T.-H. Fang, and Y.-C. Lin. Physical characteristics of polyimide films for flexible sensors. *Applied Physics A: Materials Science and Processing*, 92(3): 693–701, 2008.

Z. Chen, W. Ren, L. Gao, B. Liu, S. Pei, and H.-M. Cheng. Three-dimensional flexible and conductive interconnected graphene networks grown by chemical vapour deposition. *Nature Materials*, 10(6):424–428, 2011.

W.M. Choi, J. Song, D.-Y. Khang, H. Jiang, Y.Y. Huang, and J.A. Rogers. Biaxially stretchable "wavy" silicon nanomembranes. *Nano Letters*, 7(6):1655–1663, 2007.

K. Efimenko, M. Rackaitis, E. Manias, A. Vaziri, L. Mahadevan, and J. Genzer. Nested self-similar wrinkling patterns in skins. *Nature Materials*, 4(4):293–297, 2005.

M. Gonzalez, F. Axisa, M.V. Bulcke, D. Brosteaux, B. Vandevelde, and J. Vanfleteren. Design of metal interconnects for stretchable electronic circuits using finite element analysis. In *EuroSime 2007: International Conference on Thermal, Mechanical and Multi-Physics Simulation Experiments in Microelectronics and Micro-Systems, 2007*, 2007.

M. Gonzalez, F. Axisa, M.V. Bulcke, D. Brosteaux, B. Vandevelde, and J. Vanfleteren. Design of metal interconnects for stretchable electronic circuits. *Microelectronics Reliability*, 48(6):825–832, 2008.

D.S. Gray, J. Tien, and C.S. Chen. High-conductivity elastomeric electronics. *Advanced Materials*, 16(5):393–397, 2004.

Yoshiaki Hattori, Leo Falgout, Woosik Lee, Sung-Young Jung, Emily Poon, Jung Woo Lee, Ilyoun Na, Amelia Geisler, Divya Sadhwani, Yihui Zhang, Yewang Su, Xiaoqi Wang, Zhuangjian Liu, Jing Xia, Huanyu Cheng, R. Chad Webb, Andrew P. Bonifas, Philip Won, Jae-Woong Jeong, Kyung-In Jang, Young Min Song, Beatrice Nardone, Michael Nodzenski, Jonathan A. Fan, Yonggang Huang, Dennis P. West, Amy S. Paller, Murad Alam, Woon-Hong Yeo, and John A. Rogers. Multifunctional skin-like electronics for quantitative, clinical monitoring of cutaneous wound healing. *Advanced Healthcare Materials*, pages n/a–n/a, 2014. ISSN 2192-2659.

J.P.M. Hoefnagels, J. Neggers, P.H.M. Timmermans, O. Van Der Sluis, and M.G.D. Geers. Copper-rubber interface delamination in stretchable electronics. *Scripta Materialia*, 63(8):875–878, 2010.

M. Hommel and O. Kraft. Deformation behavior of thin copper films on deformable substrates. *Acta Materialia*, 49(19):3935–3947, 2001.

Y.-Y. Hsu, M. Gonzalez, F. Bossuyt, F. Axisa, J. Vanfleteren, and I. De Wolf. In situ observations on deformation behavior and stretchinginduced failure of fine pitch stretchable interconnect. *Journal of Materials Research*, 24(12):3573–3582, 2009.

Y.-Y. Hsu, M. Gonzalez, F. Bossuyt, F. Axisa, J. Vanfleteren, and I. De Wolf. The effect of pitch on deformation behavior and the stretching-induced failure of a polymer-encapsulated stretchable circuit. *Journal of Micromechanics and Microengineering*, 20(7), 2010a.

Y.-Y. Hsu, M. Gonzalez, F. Bossuyt, F. Axisa, J. Vanfleteren, B. Vandevelde, and I. De Wolf. Design and analysis of a novel fine pitch and highly stretchable interconnect. *Microelectronics International*, 27(1):33–38, 2010b.

Y.-Y. Hsu, M. Gonzalez, F. Bossuyt, F. Axisa, J. Vanfleteren, and I. De Wolf. The effects of encapsulation on deformation behavior and failure mechanisms of stretchable interconnects. *Thin Solid Films*, 519(7):2225–2234, 2011a.

Y.-Y. Hsu, M. Gonzalez, F. Bossuyt, J. Vanfleteren, and I. De Wolf. Polyimide-enhanced stretchable interconnects: Design, fabrication, and characterization. *IEEE Transactions on Electron Devices*, 58(8):2680–2688, 2011b.

Z.Y. Huang, W. Hong, and Z. Suo. Nonlinear analyses of wrinkles in a film bonded to a compliant substrate. *Journal of the Mechanics and Physics of Solids*, 53(9): 2101–2118, 2005.

J. Jansons, A. Aniskevich, and L. Pazhe. Analysis of reversible and irreversible strains in the creep of a nonlinear viscoelastic polymer. *Mechanics of Composite Materials*, 48(2):209–216, 2012.

J. Jones, S.P. Lacour, S. Wagner, and Z. Suo. A method for making elastic metal interconnects. In *Materials Research Society Symposium - Proceedings*, volume 769, pages 189–194, 2003.

J. Jones, S.P. Lacour, S. Wagner, and Z. Suo. Stretchable wavy metal interconnects. *Journal of Vacuum Science and Technology A: Vacuum, Surfaces and Films*, 22 (4):1723–1725, 2004.

Y.J. Jung, S. Kar, S. Talapatra, C. Soldano, G. Viswanathan, X. Li, Z. Yao, F.S. Ou, A. Avadhanula, R. Vajtai, S. Curran, O. Nalamasu, and P.M. Ajayan. Aligned carbon nanotube-polymer hybrid architectures for diverse flexible electronic applications. *Nano Letters*, 6(3):413–418, 2006.

D.-Y. Khang, H. Jiang, Y. Huang, and J.A. Rogers. A stretchable form of single-crystal silicon for high-performance electronics on rubber subtrates. *Science*, 311 (5758):208–212, 2006.

D.-H. Kim, J. Song, M.C. Won, H.-S. Kim, R.-H. Kim, Z. Liu, Y.Y. Huang, K.-C. Hwang, Y.-W. Zhang, and J.A. Rogers. Materials and noncoplanar mesh designs for integrated circuits with linear elastic responses to extreme mechanical deformations. *Proceedings of the National Academy of Sciences of the United States of America*, 105(48):18675–18680, 2008.

D.-H. Kim, Z. Liu, Y.-S. Kim, J. Wu, J. Song, H.-S. Kim, Y. Huang, K.-C. Hwang, Y. Zhang, and J.A. Rogers. Optimized structural designs for stretchable silicon integrated circuits. *Small*, 5(24):2841–2847, 2009.

D.-H. Kim, N. Lu, R. Ghaffari, Y.-S. Kim, S.P. Lee, L. Xu, J. Wu, R.-H. Kim, J. Song, Z. Liu, J. Viventi, B. De Graff, B. Elolampi, M. Mansour, M.J. Slepian, S. Hwang, J.D. Moss, S.-M. Won, Y. Huang, B. Litt, and J.A. Rogers. Materials for multifunctional balloon catheters with capabilities in cardiac electrophysiological mapping and ablation therapy. *Nature Materials*, 10(4):316–323, 2011.

D.H. Kim, J. Viventi, J.J. Amsden, J. Xiao, L. Vigeland, Y.S. Kim, J.A. Blanco, B. Panilaitis, E.S. Frechette, D. Contreras, D.L. Kaplan, F.G. Omenetto, Y. Huang, K.C. Hwang, M.R. Zakin, B. Litt, and J.A. Rogers. Dissolvable films

of silk fibroin for ultrathin conformal bio-integrated electronics. *Nature materials*, 9(6):511–517, 2010.

K.-S. Kim, K.-H. Jung, and S.-B. Jung. Design and fabrication of screen-printed silver circuits for stretchable electronics. *Microelectronic Engineering*, 2013.

H.C. Ko, G. Shin, S. Wang, M.P. Stoykovich, J.W. Lee, D.-H. Kim, J.S. Ha, Y. Huang, K.-C. Hwang, and J.A. Rogers. Curvilinear electronics formed using silicon membrane circuits and elastomeric transfer elements. *Small*, 5(23): 2703–2709, 2009.

M. Kolluri, M.H.L. Thissen, J.P.M. Hoefnagels, J.A.W. van Dommelen, and M.G.D. Geers. In-situ characterization of interface delamination by a new miniature mixed mode bending setup. *International Journal of Fracture*, 158(2):183–195, 2009.

M. Kolluri, J.P.M. Hoefnagels, J.A.W. Van Dommelen, and M.G.D. Geers. An improved miniature mixed-mode delamination setup for in situ microscopic interface failure analyses. *Journal of Physics D: Applied Physics*, 44(3), 2011.

O. Kraft, M. Hommel, and E. Arzt. X-ray diffraction as a tool to study the mechanical behaviour of thin films. *Materials Science and Engineering A*, 288(2): 209–216, 2000.

C.-T. Kuo, M.-C. Yip, and K.-N. Chiang. Time and temperature dependent mechanical characterization of polymer-based materials in electronic packaging applications. *Journal of the Chinese Institute of Engineers, Transactions of the Chinese Institute of Engineers,Series A/Chung-kuo Kung Ch'eng Hsuch K'an*, 27 (7):949–954, 2004.

S.P. Lacour, S. Wagner, Z. Huang, and Z. Suo. Stretchable gold conductors on elastomeric substrates. *Applied Physics Letters*, 82(15):2404–2406, 2003.

S.P. Lacour, J. Jones, S. Wagner, T. Li, and Z. Suo. Stretchable interconnects for elastic electronic surfaces. *Proceedings of the IEEE*, 93(8):1459–1466, 2005.

T. Li and Z. Suo. Deformability of thin metal films on elastomer substrates. *International Journal of Solids and Structures*, 43(7-8):2351–2363, 2006.

T. Li, Z. Suo, S.P. Lacour, and S. Wagner. Compliant thin film patterns of stiff materials as platforms for stretchable electronics. *Journal of Materials Research*, 20(12):3274–3277, 2005.

K.L. Lin, J. Chae, and K. Jain. Design and fabrication of large-area, redundant, stretchable interconnect meshes using excimer laser photoablation and in situ masking. *IEEE Transactions on Advanced Packaging*, 33(3):592–601, 2010.

N. Lu, X. Wang, Z. Suo, and J. Vlassak. Failure by simultaneous grain growth, strain localization, and interface debonding in metal films on polymer substrates. *Journal of Materials Research*, 24(2):379–385, 2009.

R. Lucchini. *Mechanics of stretchable interconnects for stretchable electronics devices*. PhD thesis, Structural, Seismic and Geotechnical Engineering Department, Politecnico di Milano, 2014.

V.J. Lumelsky, M.S. Shur, and S. Wagner. Sensitive skin. *IEEE Sensors Journal*, 1 (1):41–51, 2001.

P. Matyba, H. Yamaguchi, G. Eda, M. Chhowalla, L. Edman, and N.D. Robinson. Graphene and mobile ions: The key to all-plastic, solution-processed light-emitting devices. *ACS Nano*, 4(2):637–642, 2010.

H. Mei, R. Huang, J.Y. Chung, C.M. Stafford, and H.-H. Yu. Buckling modes of elastic thin films on elastic substrates. *Applied Physics Letters*, 90(15), 2007.

J. Neggers, J. Hoefnagels, O. Van Der Sluis, O. Sedaghat, and M. Geers. Interface integrity in stretchable electronics. In *Conference Proceedings of the Society for Experimental Mechanics Series*, volume 6, pages 577–581, 2011.

P.J. Roache. Perspective: a method for uniform reporting of grid refinement studies. *Journal of Fluids Engineering, Transactions of the ASME*, 116(3):405–413, 1994.

J.A. Rogers. Electonics: Toward paperlike displays. *Science*, 291(5508):1502–1503, 2001.

T. Sekitani, Y. Noguchi, K. Hata, T. Fukushima, T. Aida, and T. Someya. A rubberlike stretchable active matrix using elastic conductors. *Science*, 321(5895): 1468–1472, 2008.

C. Shet and N. Chandra. Analysis of energy balance when using cohesive zone models to simulate fracture processes. *Journal of Engineering Materials and Technology, Transactions of the ASME*, 124(4):440–450, 2002.

T. Someya, T. Sekitani, S. Iba, Y. Kato, H. Kawaguchi, and T. Sakurai. A large-area, flexible pressure sensor matrix with organic field-effect transistors for artificial skin applications. *Proceedings of the National Academy of Sciences of the United States of America*, 101(27):9966–9970, 2004.

J. Song, H. Jiang, Z.J. Liu, D.Y. Khang, Y. Huang, J.A. Rogers, C. Lu, and C.G. Koh. Buckling of a stiff thin film on a compliant substrate in large deformation. *International Journal of Solids and Structures*, 45(10):3107–3121, 2008.

Y. Sun and J.A. Rogers. Structural forms of single crystal semiconductor nanoribbons for high-performance stretchable electronics. *Journal of Materials Chemistry*, 17(9):832–840, 2007.

J. Viventi, D.-H. Kim, L. Vigeland, E.S. Frechette, J.A. Blanco, Y.-S. Kim, A.E. Avrin, V.R. Tiruvadi, S.-W. Hwang, A.C. Vanleer, D.F. Wulsin, K. Davis, C.E. Gelber, L. Palmer, J. Van Der Spiegel, J. Wu, J. Xiao, Y. Huang, D. Contreras, J.A. Rogers, and B. Litt. Flexible, foldable, actively multiplexed, high-density electrode array for mapping brain activity in vivo. *Nature Neuroscience*, 14(12): 1599–1605, 2011.

A.L. Volynskii, S. Bazhenov, O.V. Lebedeva, and N.F. Bakeev. Mechanical buckling instability of thin coatings deposited on soft polymer substrates. *Journal of Materials Science*, 35(3):547–554, 2000.

S. Wagner, S.P. Lacour, J. Jones, P.-H.I. Hsu, J.C. Sturm, T. Li, and Z. Suo. Electronic skin: Architecture and components. *Physica E: Low-Dimensional Systems and Nanostructures*, 25(2-3 SPEC.ISS.):326–334, 2004.

J. Wu, M. Agrawal, H.A. Becerril, Z. Bao, Z. Liu, Y. Chen, and P. Peumans. Organic light-emitting diodes on solution-processed graphene transparent electrodes. *ACS Nano*, 4(1):43–48, 2010.

C. Yu and H. Jiang. Forming wrinkled stiff films on polymeric substrates at room temperature for stretchable interconnects applications. *Thin Solid Films*, 519(2): 818–822, 2010.